Computational Spectral Microscopy and Compressive Millimeter-wave Holography

by

Christy Ann Fernandez

Department of Electrical and Computer Engineering

Date: _____

Approved:

_____
David J. Brady, Supervisor

_____
Joseph N. Mait

_____
Bobby Guenther

_____
Adrienne Stiff-Roberts

_____
Jungsang Kim

Dissertation submitted in partial fulfillment of the
requirements for the degree of Doctor of Philosophy
in the Department of Electrical and Computer Engineering
in the Graduate School of
Duke University

2010

ABSTRACT

Computational Spectral Microscopy and Compressive Millimeter-wave Holography

by

Christy Ann Fernandez

Department of Electrical and Computer Engineering
Duke University

Date: _____

Approved:

_____
David J. Brady, Supervisor

_____
Joseph N. Mait

_____
Bobby Guenther

_____
Adrienne Stiff-Roberts

_____
Jungsang Kim

An abstract of a dissertation submitted in partial fulfillment of the requirements for the degree of Doctor of Philosophy in the Department of Electrical and Computer Engineering in the Graduate School of Duke University

2010

Copyright © 2010 by Christy Ann Fernandez
All rights reserved

Abstract

This dissertation describes three computational sensors. The first sensor is a scanning multi-spectral aperture-coded microscope containing a coded aperture spectrometer that is vertically scanned through a microscope intermediate image plane. The spectrometer aperture-code spatially encodes the object spectral data and nonnegative least squares inversion combined with a series of reconfigured two-dimensional (2D spatial-spectral) scanned measurements enables three-dimensional (3D) (x, y, λ) object estimation. The second sensor is a coded aperture snapshot spectral imager that employs a compressive optical architecture to record a spectrally filtered projection of a 3D object data cube onto a 2D detector array. Two nonlinear and adapted TV-minimization schemes are presented for 3D (x, y, λ) object estimation from a 2D compressed snapshot. Both sensors are interfaced to laboratory-grade microscopes and applied to fluorescence microscopy. The third sensor is a millimeter-wave holographic imaging system that is used to study the impact of 2D compressive measurement on 3D (x, y, z) data estimation. Holography is a natural compressive encoder since a 3D parabolic slice of the object band volume is recorded onto a 2D planar surface. An adapted nonlinear TV-minimization algorithm is used for 3D tomographic estimation from a 2D and a sparse 2D hologram composite. This strategy aims to reduce scan time costs associated with millimeter-wave image acquisition using a single pixel receiver.

Contents

Abstract **iv**

List of Tables **viii**

List of Figures **ix**

Acknowledgements **xviii**

1 Introduction **1**

1.1 Organization 10

1.2 Contributions 11

2 Scanning multi-spectral aperture-coded microscope **13**

2.1 Introduction 14

2.2 Mathematical system model 19

2.2.1 Calibration and reconstruction 26

2.3 System design 29

2.3.1 Coded aperture spectrometer (CAS) design 29

2.3.2 Spectrometer and microscope interface 34

2.3.3 SmacM spatial resolution metrics 38

2.4 Simulation results 40

2.5 Experimental results 47

2.5.1 Calibration and sample illumination 48

2.5.2 Narrow-source illuminated calibration targets 51

2.5.3 Fluorescence microscopy with SmacM 55

2.6 Summary 63

3 Snapshot spectral imaging **65**

3.1 Introduction 66

3.2 System model 69

3.3 Reconstruction procedure and simulation results 77

3.3.1 3D data cube estimation algorithm 77

3.3.2 Direct spectral feature identification algorithm 79

3.3.3 Simulation Results 86

3.4 System design 96

3.5 Experimental results 98

3.5.1 Image quality analysis with (DD)CASSI 98

3.5.2 Calibration procedure and algorithm implementation 102

3.5.3 Fluorescence microscopy with CASSI 105

3.5.4 Verification testbed 110

3.6 Dynamic imaging with CASSI 113

3.7 Compact CASSI-II design 114

3.8 Summary 119

4 Millimeter-wave compressive holography **122**

4.1 Introduction 123

4.2 Theory 126

4.2.1 Hologram recording geometry 131

4.2.2 Hologram plane sampling and resolution metrics 134

4.3 Reconstruction methods and Simulations 137

4.3.1 Simulation Results 145

4.4 Experimental setup 156

4.5 Experiment results 159

4.6 Summary and Conclusion 168

5 Conclusions and discussion **170**

A Appendix **173**

A.1 Derivation of angular, linear dispersion, and spectral resolution 173

A.2 Hadamard and S-matrices 175

A.3 Pseudo-inverse TV-minimization for 3D data cube estimation 176

A.4 Full-field CASSI illumination fiber coupled setup 181

A.5 Millimeter-wave compressive holography forward and adjoint model matrices 184

A.6 Millimeter-wave holography InP Gunn source characteristics 188

A.7 Millimeter-wave holography: superheterodyne receiver sensitivity calculation 190

Bibliography **192**

Biography **200**

List of Tables

3.1 Zemax and experimental spot sizes 100

3.2 Fluorescent Microspheres 106

4.1 Synthetic 3D Slit (ST) and 3D Gun and Dagger (GD) Sparsity 155

List of Figures

1.1 Image compressibility in the discrete cosine transform (DCT) basis. (a) MATLAB baseline phantom image. Coefficient removal by (b) 31.51%, (c) 61.72%, and (d) 73.60%. (e) MATLAB baseline cameraman image. Coefficient removal by (f) 17.82%, (g) 61.48%, and (h) 78.90%. 4

2.1 (a) Optical architecture for the CAS consisting of an input aperture (OP), grating (G), and a 2D focal plane (FP). (b) Power spectral density profile propagated through the system architecture. The effect of the aperture-code on the power spectral density is shown. 19

2.2 Object data point mapping onto a 2D detector plane. Location of the object data point along the y-axis remains constant, while the point along the x-axis is dependent upon λ at x. This dependence is due to the grating linear dispersion occurring along the x-axis. This diagram is a pictorial representation of the shift-invariant impulse response h for the CAS. 20

2.3 CAS pushbroom data collection and inversion flow diagram 25

2.4 Optical design of the f/7 spectrometer showing the object plane (OP), collimating optics (L1 and L2), grating (G), imaging optics ($L1$ and $L2$), and a focal plane (FP). 30

2.5 Spot diagrams for various field positions at (a) $\lambda = 550$ nm, (b) $\lambda = 600$ nm, (c) and $\lambda = 665$ nm. 32

2.6 Spectrometer MTF plot at all field positions and at three wavelengths (550 nm, 600 nm, and 665 nm) within the prescribed spectral range of the system. 33

2.7 *SolidWorks* 3D rendered image of the spectrometer mounted to a CCD. 34

2.8 (a) Optical schematic for SmacM. (b) Hardware layout for the system. (c) At the intermediate image plane of the microscope, a 0.35× *Nikon* coupler demagnifies the relayed image and maps object data onto the coded aperture spectrometer. (d) CAD rendered image of the sample holder for the microscope. 36

2.9 Optical resolution limits of different numerical aperture (NA) microscope objectives as a function of wavelength. 39

2.10 Simulated SmacM measurements and reconstructions. (a) A Matlab 'Shepp-Logan phantom' test image with a spatially varying intensity, as seen in the colorbar. (b) Shuffled, order 64 S-matrix. (c) Multi-spectral 'Shepp-Logan phantom' reconstruction from simulated detector scanned measurements. (d) A subset of scanned measurements across the object data, a sum is taken over the spectral axis. Two 'Shepp-Logan phantom' images with varying intensity represents dispersion from the grating and the intensity variation represents the variation in spectrum intensity. (e) Aperture-code modulation of a single row from the object data over a series of 64 scanned measurements. Two copies appear due to the spectral content of the object row along the x-axis. (f) Reconstructed spectral plot overlayed with the baseline data at a single pixel location in the reconstructed object data cube. 41

2.11 SmacM simulations from a spectrally extended input object. (a) Spectral plot at a single spatial location within the estimated object data cube. The NNLS spectral estimate and baseline spectral plot are shown. (b) Reconstructed image estimate of the 'Shepp-Logan phantom' object cube. (c) CAS snapshot showing the object mask-modulated and dispersed image. (e) Aperture-code modulation of a single row from the object data over a series of 64 scanned measurements. Two copies appear due to the spectral content of the object that is dispersed along the x-axis. 43

2.12 SmacM image reconstructions from simulated measurements corrupted by AWGN. Synthetic baseline images include (a) a 2D 'Shepp-Logan phantom', (b) circles and slits, and (c) circles. (d-f) Reconstruction PSNR versus Measurement SNR corrupted by AWGN for spectrally different input object emissions. Note that a decrease in PSNR after a maximum is seen due to the measurement S-matrix central column that is completely opaque. 45

2.13 NNLS data inversion. (a) Cropped image of a CAS response to a Krypton lamp source. (b) Spectral estimates calculated using NNLS. (c) Aligned spectral estimates. (d) Summation of the spectral estimates provided a spectral profile. (e) Calibrated spectral profile generated using the 'polyfit' function in MATLAB to interpolate known spectral peaks for the Krypton lamp with locations from the reconstructed spectrum for the source (peak location 170 in (d) becomes 587.1 nm and peak location 220 becomes 557 nm. 50

2.14 (a) "On" and (b)"off" amplitude values from two spatial locations in the reconstructed object data cube as a function of wavelength. (c) SPOT Baseline image of a chrome-on-quartz fractal pattern observed with a 20× objective and 0.35× demagnifier. (d) Downsampled baseline image created to match the resolution of the aperture-coded spectrometer. (e) Reconstruction estimate for a single transverse image at a single spectral channel. 52

2.15 Object data cube for a chrome-on-quartz 'DISP' mask illuminated by a green HeNe and HeNe diffuse laser combination. Rotated image at spectral channel (a) $k = 248$ (evidence of green HeNe source), (b) $k = 150$, (c) $k = 97$ (evidence of the HeNe source), and (d) $k = 15$. (e) Baseline downsampled 2D image obtained with the SPOT camera at a slightly different field of view compared to the CAS field of view. (f) Spectral plot at a single voxel in the data cube where a green HeNe laser peak and a HeNe laser peak are shown. 54

2.16 Object data cube reconstruction of 0.2 μm fluorescent microspheres excited by 532 nm laser light. Transverse images at spectral channels (a) $k = 268$, (b) $k = 222$, (c) $k = 205$, (d) $k = 128$, and (e) $k = 10$ are shown. (f) Downsampled baseline image from the SPOT camera. (g) Spectral plot for the spatial location row 29, column 57 on the bead overlayed with an OO baseline spectrum. (h) Spectral plot of a background pixel located at spatial position row 29, column 80. . . . 58

2.17 Excitation and emission spectra from (a) the green-fluorescent BODIPY FL goat anti-mouse IgG label and (b) the red-fluorescent Texas Red-X phalloidin label contained in the bovine pulmonary artery endothelial cell, *Invitrogen* FluoCell Slide #2. 61

2.18 Object data cube reconstruction of the *Invitrogen* FluoCell Slide #2 containing bovine pulmonary artery endothelial cells 5 - 20 μm in size. Object data cube reconstruction of spatial slices at spectral channels (a) $k = 313$, (b) $k = 284$, (c) $k = 250$, (d) $k = 200$, and (e) $k = 10$ are shown. (f) Downsampled baseline image from the SPOT camera. (g) RGB rendered image with the SPOT camera. (h) Spectral plot at spatial location row = 10 and column = 8 on the cell and (i) at spatial location row = 13 and column = 80 located in the background of the object data cube. 62

3.1 (a) Optical architecture for a DD CASSI consisting of two Amici prisms (AP1 & AP2), an aperture code (M) and a focal plane (FP). (b) Power spectral density profile propagated through the system optical architecture. The effect of the aperture code on the power spectral density is illustrated. 70

3.2 (a) Object data cube (f) transformation into a sparse data cube (α) using spectral priors (W). A spectrum recorded at a single pixel location in f corresponds to a single pixel value and bead identity in α. (b) Matrix representation of the spectral data base, W. W can be thought of as a spectrum look-up table.† 80

3.3 (a) Simulated 64 x 64 pixel aperture code. (b) Downsampled fluorescence spectra of a 0.3 intensity-valued yellow green (YG/n=1), 0.5 intensity-valued orange (O/n=2), 1.0 intensity-valued red (R/n=3) and 0.7 intensity-valued crimson (C/n=4) beads. (c) Simulated 10×10 pixel fluorescent squares in a 64×64 pixel image with the corresponding (d) simulated detector image. (e) Input image for 15×15 pixel spectrally different fluorescent squares in a 64×64 pixel image with the corresponding (f) simulated detector image. Note that the colors in (c,e) represent the different intensity values of the simulated fluorescent squares.† 87

3.4 Simulated f and f^* data cubes where each sub-image represents a transverse image as a function of spectral slice, k. (a) "true" $f(i, j, k)$ data cube as a function of k for 10×10 pixel squares, (b) estimated $f^*(i, j, k)$ data cube as a function of k for 10×10 pixel squares, (c) "true" $f(i, j, k)$ data cube as a function of k for 15×15 pixel squares, and (d) estimated $f^*(i, j, k)$ data cube as a function of k for 15×15 pixel squares. 90

3.5 Simulated α and reconstructed α^* data cube where each n-channel relates to a single spectral vector in W. (YG, n=1; O; n=2; R, n=3; C,n = 4)(a) "true" $\alpha(m_1, m_2)$ as a function of n for 10×10 pixel squares (b) estimated $\alpha^*(m_1, m_2)$ as a function of n for 10×10 pixel squares. The dotted line in the $n = 4$ slice represents a residual artifact from the $n = 3$ slice. (c)"true" $\alpha(m_1, m_2)$ as a function of n for 15×15 pixel squares (d) estimated $\alpha^*(m_1, m_2)$ as a function of n for 15×15 pixel squares.† 91

3.6 Plot of reconstruction MSE from CASSI measurements corrupted by Poisson noise. Reconstruction efficacy is compared between (a) direct f^* data cube estimation and (b) f^*_α data cube estimation (see Section 3.3C for the definition of f^*_α).† 94

3.7 (a) Optical architecture for a CASSI interface to an inverted microscope. (b) Realization of Fig. 3.1(a) is in this ray-traced drawing for the first-half of CASSI where (f) is the object (L1) and (L2) are imaging and collimating lenses, (AP) is a direct-view double Amici prism and (MP) is the mask plane where the aperture code resides. (c) Layout of a Zeiss AxioObserver microscope with CASSI coupled to an exit port. (d) Back-end of CASSI.† 96

3.8 (a) Bandpass filtered halogen (500 - 510 nm) illuminated double slit (12 μm) (DD) CASSI image without the aperture-code in the intermediate image plane. (b) Edge spread function (ESF) recorded along (the orange line) a single column and all rows in (a). (c) Line spread function (LSF) generated for regions $L1$, $L2$, $R1$, and $R2$ in (b) with a gaussian curve fit applied to each LSF. (d) *Zemax* modulation transfer (MTF) plot of the custom designed (DD) CASSI system. Experimentally estimated MTFs at (e) 450 nm, (f) 500 nm, (g) 650 nm, and (h) 700 nm. 101

3.9 f* data cube reconstruction using TV-minimization. Amplitude spectral plots at a single spatial location on the (a) $BG1$ bead, (b) $G1$ bead, (c)$YG1$ bead, (d) $Y1$ bead, (e) $O1$ bead, (f) $RO1$ bead, (g) $R1$ bead, (h) $CA1$ bead, (i) $C1$ bead, and (j) $S1$ bead labeled accordingly in (k). Baseline OO spectra for each bead type are overlayed with CASSI-based reconstructed spectra. (k) Pseudo-colored ten bead CASSI reconstructed image. White circles are additionally added to the image to outline the bead locations.† 108

3.10 (a) Baseline CASSI 2D intensity-valued measurement of a ten bead type fluorescent scene acquired with a 50×, 0.4 NA microscope objective. White circles are added to the images to outline the locations of the beads. (b) CASSI reconstructed 2D spectral feature map, γ_1^*. (c) CASSI 2D spectral feature map, γ_2^*. (d) Nikon A1 series baseline image with ten bead type discrimination where the beads are additionally outlined in white. (e) Spectral vectors used in the database, W, for CASSI reconstructions.† 111

3.11 *Zemax* 3D optical architecture of CASSI-II where f_0 represents the source spectral density and *FP* represents the monochromatic detector plane.. 115

3.12 *Zemax* CASSI-II spot diagrams at the mask plane for wavelengths (a) 470 nm, (b) 600 nm, (c) and 770 nm. Image plane CASSI-II spot diagrams at wavelengths (d) 470 nm, (e) 600 nm, and (f) 770 nm. . . 117

4.1 Fourier-transform domain sampling of the object band volume in a transmission geometry. (a) 2D slice of a 3D sphere where the dotted-line represents the measurement from single plane wave illumination. (b) Rectilinear pattern represents wave vectors sampled by the hologram due to a finite detector plane sampling. (c) Wave normal sphere cross-section for spatial and axial resolution analysis.† 130

4.2 (a) Spectrum for an off-axis hologram recording depicting an inherent increase in bandwidth for adequate object separation from undiffracted terms. (b) Spectrum for a Gabor hologram recording depicting the overlay of undiffracted, object, and conjugate terms. (c) Transverse slices from linear inverse propagation results at various z-planes.† . . 132

4.3 Transverse slices from TV-minimization reconstructions at different z-planes. A dominant squared-field term is confined to the z=0 plane.† 143

4.4 Sampling windows for sparse measurement where (a) 3.9%, (b) 9.77%, (c) 23.83%, (d) 44.56%, and (e) 54.68% measurements are removed.† . 145

4.5 Synthetic 3D slit object results with an applied transmittance function and corrupted by AWGN at a 30 dB measurement SNR using (a) backpropagation and (b) TV-minimization for 3D tomographic object estimation. Various values for τ (0.2 – 1.0) are used for sparsely sampled (0.0 – 54.68%) TV reconstructions† (see Table 4.1) 149

4.6 Synthetic 3D dagger and gun object results with an applied transmittance function and corrupted by AWGN at a 30 dB measurement SNR using (a) backpropagation and (b) TV-minimization for 3D tomographic object estimation. A τ value of 0.2 is used for TV-minimization reconstructions from sparsely sampled detector measurements corrupted by AWGN (see Table 4.1).† 150

4.7 Experiment with a polymer model gun and dagger placed at two different distances along the axial plane.(a) Photograph of the experiment. Transverse slices in four different z-planes of the (b) backpropagated and (c) TV-minimization reconstructions. Amplitude pixel (x,y) as a function of z, in 10 mm increments, where TV-minimization and backpropagation for a central point on the (d) barrel of the gun and (e) on the blade edge of the dagger are plotted.† 152

4.8 Plot of reconstruction PSNR (in dB) versus measurement SNR (in dB) from millimeter-wave holography detector measurements corrupted by AWGN. TV-minimization reconstruction results with 0.0 - 54.7% measurement reduction are shown for the (a) synthetic slit target and (b) synthetic gun and dagger target. Backpropagation reconstruction results with 0.0 - 54.7% measurement reduction are shown for the (c) synthetic slit target and (d) synthetic gun and dagger target.† 154

4.9 Optical schematic for millimeter-wave Gabor holography containing a waveguide (WG), object extent (L_x), detector plane sampling with number of pixels (N) and pixel pitch (dx), waveguide to object distance (z_1), and object to receiver distance (z_3).† 157

4.10 Superheterodyne receiver (a) circuit diagram and (b) experimental layout where incident energy (RF in) is mixed with a local oscillator (LO), down converted to an intermediate frequency (IF), amplified by both an LNA and a second amplifier, filtered with a band pass filter (BPF), and detected with a Schottky diode.† 158

4.11 Object scale of a semi-transparent polymer (a) wrench, (b) dagger, and (c) gun.† 161

4.12 Experiment with a polymer model wrench, gun, and dagger placed at three different distances along the axial plane.(a) Photograph of the experiment. Transverse slices in four different z-planes of the (b) backpropagated and (c) TV-minimization reconstructions. Amplitude pixel (x,y) as a function of z, in 5 mm increments, where TV-minimization reconstructions and backpropagation estimates for a center point on the (d) wrench, (e) gun, and (f) dagger are plotted.† 164

4.13 Experimental holographic recording of (a) a model dagger and a model gun and (c) a model dagger, a model gun, and a model wrench located in different z-planes.† 165

4.14 Sparse measurement reconstruction of experimental data using (a) linear backpropagation and (b) TV-minimization for 3D object estimation. Amplitude of a central pixel (x,y) on the blade edge of the dagger as a function of z, plotted in 10 nm increments, from (c) 3.9% holographic measurement removal and (d) 54.68% holographic measurement removal.† 167

A.1 (a) Hadamard (H_A) and S-matrices (S_A) of different orders. (b) Singular value spectrum. 175

A.2 CASSI system model where the transformation matrix (H) is represented by a summation matrix (V) and a calibration cube matrix (C) from a CASSI system measuring four spectral channels 177

A.3 (a) Singular values plot for the transformation matrix, H.(b) Singular values plot for H^+.(c) Singular values plot for the H^+H matrix . . . 178

A.4 (a) Simulated 40×40 pixel aperture-code. (b) Simulated 15×15 pixel fluorescent squares in a 40×40 detector image. Baseline and pseudo-inverse adapted TV-minimization spectral estimates at a single spatial locations from each 15×15 pixel square for the (c) yellow-green and (d) orange spectral signature. (e) Baseline f data cube of 15×15 pixel squares. (f) Pseudo-inverse TV-minimization f^* data cube estimate. . 180

A.5 (a) *Zemax* system prescription data for the optical setup used for CASSI calibration data acquisition. (b) (distance units in mm) *Zemax* 3D optical layout for object space NA matching and full-field illumination of CASSI. 182

A.6 (a) *Epsilon Lambda* spectral linewidth plot of a tunable W-band InP Gunn diode at a 94 GHz central frequency. (b) Data sheet for the InP Gunn diode oscillator with a maximum output power at 20 dBm (100 mW). Power output as a function of micrometer reading. (c) Spectrum analyzer reading from the superheterodyne receiver circuit at a single frequency (94 GHz before heterodyne detection) of 7.55 GHz. Power reading measures .10 mW at the detector and greater than 25 mW at the output to the waveguide after 6 dB attenuation. 189

A.7 Receiver output voltage versus input power at 94 GHz. 191

Acknowledgements

As a child, one begins the quest of learning through curiosity. Parents provide inspiration through answered questions, encouragement, patience, and love.

Throughout my academic career, I have been encouraged by my mother and father to persevere even when goals may seem unattainable and challenges complicated. My uncle, Mike Rosa, once said, "If not you, then who? If not now, then when?" Graduate school was the epitomy of perseverance. Without the love, assistance, and encouragement from my mother, father, and husband; I could not complete graduate school or this document.

Mentors are meant to mold and challenge a student. I thank Dr. Larry Medsker for guiding me through my undergraduate career at American University, for encouraging me to obtain a Ph.D., and for his neverending friendship. Attending graduate school at Duke University was made possible by Dr. David Brady. I thank him immensely for his faith in my potential as a researcher, for his abundant encouragement, and for his commitment to guide and intellectually challenge me. He is a brilliant advisor and I am grateful for the opportunity to have worked in his group. Dr. Joseph Mait and David Wikner both inspired and mentored me in the field of millimeter-wave imaging. I thank Dr. Joseph Mait and David Wikner for taking the time to work with me, treating me as an equal and a friend, and for their patience. Finally, I would like to thank my defense committee: Dr. Stiff-Roberts for her advice through the graduate school process, Dr. Jungsang Kim for his challenging questions and support since my qualifying exam, and Dr. Bob Guenther for his guidance.

Also, I thank my DISP colleagues at Duke University who have inspired research discussions and provided comfort through research and coursework challenges: Dr. Kerkil Choi, Dr. Michael Gehm, Evan Cull, Andrew Portnoy, Ashwin Wa-

gadarikar, Sehoon Lim, David Kittle, Nan Zheng, Scott McCain, and Mohan Shankar. Finally, a special thanks to Ryoichi Horisaki of Osaka University in Japan for extremely helpful discussions about diffraction tomography. A special thanks is extended to the administrative staff for their assistance through the years – Jennifer Dubow, Leah Goldsmith, Samantha Morton, and Ellen Currin.

I also acknowledge the support of a National Defense Science and Engineering Graduate Fellowship (NDSEG) sponsored by the AFOSR.

Graduate school has brought many answered prayers. I can't help but thank God for his neverending love and guidance. Most of all, while providing a means for a continued education, he has blessed me with a best friend, colleague, and the man of my dreams, Evan Cull. Words can not describe how his support, love, and patience have impacted my journey through graduate school. Thank you Evan for all of your help, friendship, and love.

Henry David Thoreau said, "All endeavor calls for the ability to tramp the last mile, shape the last plan, endure the last hours toil. The fight to the finish spirit is the one ... characteristic we must posses if we are to face the future as finishers." Again, thank you mom and dad for your selfless love and encouragement. I will rise to future challenges, with the help of God, and be a finisher with you (mom and dad) as my inspiration. ¿

Chapter 1

Introduction

Discoveries in image formation have been motivated by the need to reproduce a scene of interest. For example, the pinhole camera (*camera obscura* [1]) was used to observe solar eclipses using the human eye as a detector. Painters used the same camera to project a scene onto a canvas for static scene reproduction. Until the 1827 Daguerrotype [2], scenes were not captured on film. This progression from analog detection with the eye to static scene production onto a canvas eventually led to the automation of the imaging process. The invention of the charge-coupled device in 1969 marked the beginning of the digital age in imaging and revolutionized image capture. With the digital camera, images could be stored and manipulated after acquisition using computer processing.

Digital imaging revolutionized image formation by replacing the chemical and mechanical process of film with electronic recording of light. Advances in imaging sensors and microprocessors have made static and dynamic scene capture easier. In particular, digital imaging enabled data storage where images could be stored and analyzed later. More importantly, images could be manipulated for image quality

enhancement. Post-processing methods of digital images also facilitated image compression for more efficient data storage.

Computational imaging extends beyond the advantages of digital imaging to optimize optical sensor performance. Two-dimensional (2D) detector arrays are used at the back-end of spectrometers or imagers for digital image capture. These digital images are electronic snapshots of analog signals represented by pixels with a fixed dynamic range. Computational imaging utilizes electronic detection to convert analog signals to discrete ones, while relying on microprocessor technology and post-processing capacity for data interpretation. One question that arises is: can one improve digital optical sensor performance? Computational imaging aims to provide an answer to this question.

Computational imaging sensor design involves identifying the target application, engineering the sensor design (e.g. optics, resolution, and data sampling and encoding strategy), and creating a tailored post-detection process. At the core of computational imaging a parallel design strategy exists between data sampling and encoding in the sensor hardware and for algorithm design. Sampling and encoding are vital for the development of novel computational sensors.

Data sampling and encoding can be incorporated into the spatial (e.g. image plane or pupil plane) [3] or time domain [4]. This dissertation exploits spatial domain

sampling and coding to maximize data extraction from 2D measurements using post-detection inversion. Spatial domain sampling and encoding is driven by the following questions:

- Can data be sampled and encoded in a unique way such that post-detection measurement inversion enables perfect or near perfect signal reproduction?
- How is sampling related to perfect or near perfect signal recovery?
- Do more efficient sampling strategies other than Nyquist exist?

Conventional measurements utilize traditional Shannon sampling theory [2,5]. For the imaging case, Shannon measurements correspond to uniformly sampled bandlimited 2D signals at or above the Nyquist rate ($2B$). Nyquist sampling enables perfect signal reconstruction. This sampling strategy imposes a need for a large number of measurements and high sensor resolution to maximize optical sensor performance. Optical systems limited by a data acquisition cost (e.g. pixel size, number of scans, sensor size) are challenged by complete signal estimation.

One recent tour de force is a compressive sensing (CS) paradigm that employs a sub-Nyquist sampling strategy for highly accurate signal estimation [6, 7]. Instead of utilizing Dirac delta functions or harmonic functions as the sampling basis, an alternate basis is used for perfect or nearly perfect signal reconstruction [8]. Recon-

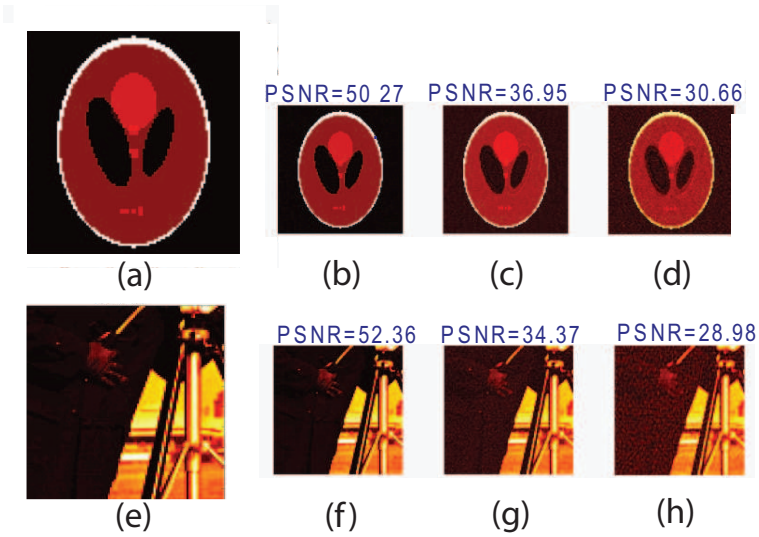

Figure 1.1: Image compressibility in the discrete cosine transform (DCT) basis. (a) MATLAB baseline phantom image. Coefficient removal by (b) 31.51%, (c) 61.72%, and (d) 73.60%. (e) MATLAB baseline cameraman image. Coefficient removal by (f) 17.82%, (g) 61.48%, and (h) 78.90%.

struction accuracy in CS depends on the sparsity or the compressibility of a signal in an alternate basis. Sparsity is commonly imposed through transform coding techniques (e.g. discrete cosine transform (DCT) or wavelet transform) [9]. A transform coding approach is a signal decomposition expressed as

$$f(x) = \sum_{i}^{N} x_i \Psi_i(x), \tag{1.1}$$

where x_i represents the coefficients of f and Ψ_i represents column vectors from the orthonormal basis (e.g. DCT). An example of image compressibility is shown in Fig. 1.1, where up to 70% of the lowest-valued DCT domain coefficients are thresholded from two MATLAB baseline images (i.e. 'Shepp-Logan phantom' and 'camera-

man') in the DCT domain and signal estimation with a high peak signal-to-noise ratio is still possible. Simulations in Fig. 1.1 show the redundance in the image data when decomposed in the DCT basis since a high percentage of coefficients can be removed without a huge sacrifice in image reconstruction.

Once the signal f is transformed into a compressible signal or a K-sparse signal using Eq. (1.1), the signal is stated to be sparse in the Ψ-domain. Then, a measurement matrix, ϕ, is used to sample a small number of projections compared to the N-dimensional signal f since ϕ is an $M \times N$ matrix. The system model is defined as

$$\begin{aligned} g &= \phi f \\ &= \phi \Psi x, \end{aligned} \tag{1.2}$$

where g is an M-dimensional vector, $\phi\Psi$ represents an $\Re^N \rightarrow \Re^M$ mapping given the $M \times N$ matrix result, and f is transformed using Ψx and is an N-dimensional vector. Note that $M \ll N$. This measurement model creates an underdetermined and often ill-posed problem since multiple solutions for f exist. In CS, it is known that incoherent projections between the sensing matrix (ϕ) and transform matrix (Ψ) improve image reconstruction [6,10,11]. A measure of the mutual coherence between the measurement basis and transform basis (ϕ, Ψ) is used as a measure for signal

recoverability. The mutual coherence metric is defined as

$$\mu(\phi, \Psi) = \sqrt{N} \max_{i,j} |< \phi_i, \Psi_j >| \, . \tag{1.3}$$

The mutual coherence is a measure of maximum correlation between the rows and columns of ϕ and Ψ. Low coherence suggests that fewer samples are required for the projective recording of the signal coefficients for perfect data recovery [10]. After exploiting signal sparsity and incoherence, a CS inversion algorithm is used for signal estimation. If M measurements are recorded at random in the ϕ-domain and the measurement basis sparsity or transform basis are incoherent, then a convex optimization program is used to solve for x where

$$\min \| \, x \, \|_{l1} \;\; \text{such that } g = \phi \Psi x. \tag{1.4}$$

Perfect recovery is achieved when

$$M \geq C \mu^2(\phi, \Psi) K \log(N). \tag{1.5}$$

The CS reduction in the total number of measurements required for accurate signal estimation enables a reduction in computational sensing resources otherwise necessitated in conventional sensing.

Computational imaging sensor design couples the aforementioned sampling strategies with spatial encoding mechanisms at the optical hardware level (i.e. before data acquisition) to extract useful information in the post-processing stage. For example, Hadamard encoding at the input to a spectrometer multiplexes object spectral information onto a detector plane [12], while well-known image compression encoding can be translated into the optical hardware design for near perfect data estimation from sub-Nyquist measurements [13]. The end goal for computational imaging at the post-detection stage is data recovery. As a result, a tailored algorithm is used to recover data from the coded measurements.

Computational imaging is particularly applicable to spectral imaging (e.g. absorption, reflectance, or emission) [14]. Spectral imaging is ubiquitous since portable digital cameras are simple spectral analyzers – providing three spectrally broad filter responses (e.g. red, green, and blue) per spatial location. Computational imaging with spectral imaging devices aims to recover a 3D (x, y, λ) object spectral density from a single or a series of intensity-valued 2D detector measurements. Since recording intensity measurements with a CCD destroys all spectral information, the use of spatial-spectral encoding strategies coupled with decoding algorithms enables the recovery of object data otherwise lost in the detection process.

Two examples of computational spectral imagers are discussed in this disserta-

tion. First, a pushbroom spectral imager employs a multiplex encoding strategy for high throughput analysis. The spectral imager projects independent and spectrally encoded measurements of the object onto a 2D detector array and uses a nonnegative least squares algorithm to decode the measurements. This spectral imager uses a coded aperture spectrometer (CAS), which replaces the slit of a conventional spectrometer with a shifted and scaled Hadamard matrix. The CAS is placed at an output port to a microscope for pushbroom operation. The pushbroom imager records multiplexed object spectral data and provides 32× higher throughput than a conventional slit spectrometer. Second, this dissertation describes a snapshot spectral imager that leverages the compressibility of signals in an alternate basis for CS data inversion. Essentially, the snapshot spectral imager incorporates compression into the optical architecture to record a 2D spectrally filtered projection of a 3D spectral data cube. With this system, a post-detection CS inversion algorithm is used to reconstruct the 3D (x, y, λ) object data cube.

Holography [15] is another application that benefits from computational imaging. Using a 2D detector array for holography enables digital holography and digital object reconstruction from intensity-valued interference measurements, thereby removing the photographic development process. However, recording intensity measurements also destroys object field information (e.g. phase). Linear algorithms are generally

used to recover the object data encoded in the diffraction pattern recorded at the 2D detector array. Within the diffraction tomography and holography literature, limitations and benefits of image acquisition and data inversion are explored. Generally, 3D tomographic object estimation is only possible when multi-angle object illumination or object rotation is employed to capture multiple digital holograms [16, 17]. Computational holography aims to deliberately subsample a 3D object band volume in a unique way so that nonlinear methods can be used to recover the object density from a single holographic recording. Computational holography does this by exploiting object sparsity and by utilizing CS numerical techniques to enable improved object reconstruction.

This dissertation provides an example of a computational holographic imager that aims to recover 3D (x, y, z) tomographic data from a single 2D holographic image composite recorded with a square-law detector [18]. Since a hologram is a natural compressive spatial encoder, capturing a 3D object band volume onto a 2D detector array, a TV-minimization algorithm is used to enable the recovery of object data otherwise challenging to decode from a single 2D hologram recording. A convex optimization method is used to reconstruct a source at a rate that violates the conventional Nyquist limit.

1.1 Organization

This dissertation presents three major projects. Chapter 2 describes the system model, opto-mechanical design, and experimental results with a second generation scanning multi-spectral aperture-coded microscope (SMACM). A series of 2D (spatial-spectral) frames are recorded with a coded aperture spectrometer (CAS). The push-broom scans are reconfigured and NNLS inverted to construct a 3D (x, y, λ) object data cube. The high throughput and efficient spatial-spectral encoding mask in the CAS makes it ideally suited for fluorescence microscopy applications. However, limits associated with scan times make SMACM non-ideal for dynamic scene analysis.

Motivated by shorter data acquisition times and dynamic scene analysis, Chapter 3 focuses on the system model and system design of a dually-dispersive (DD) coded aperture snapshot spectral imager (CASSI). Also, Chapter 3 describes two algorithms for 3D (x, y, λ) data cube estimation from a single 2D detector measurement. The chapter concludes with a discussion on dynamic scene analysis of fluorescent microspheres with CASSI and describes the *Zemax* design for an off-the-shelf and a more compact (DD) CASSI system.

Chapter 4 includes the system model, system design, and experimental results for millimeter-wave compressive holography. Two methods for 3D tomographic object

estimation are evaluated: 3D estimation from 2D holographic measurements and 3D estimation from 2D sparsely sampled holographic measurements. Each employ TV-minimization for 3D object estimation.

Finally, Chapter 5 provides a summary and thoughts on potential directions for the research efforts in the dissertation.

1.2 Contributions

The author was the principle investigator for the projects described in this dissertation. Dr. David Brady provided project direction for all research efforts in this document. Dr. Joseph Mait and David Wikner supervised the project detailed in Chapter 4.

Chapter 2 was the continuation of a previous generation system by M. Gehm and D. Brady [19].

Chapter 3 extended work by M. Gehm, R. John, D. Brady, R. Willet and T. Schultz [20] for fluorescence microscopy. Also, Dr. Kerkil Choi assisted in the algorithm development. The chapter details are reproduced from an *Applied Optics* article with permission from the journal.

Chapter 4 was motivated by compressive holography by D. Brady, K. Choi, D. Marks, R. Horisaki, and S. Lim [21]. Discussions with Ryoichi Horisaki provided

guidance for system model implementation. Michael Mattheiss automated data acquisition for experiments in Chapter 4. This chapter is reproduced from an *Applied Optics* article with permission from the journal. Dr. Joseph Mait and David Wikner assisted in the experimental realization of the millimeter-wave holography platform and Dr. Joseph Mait inspired sparse sampling.

Chapter 2

Scanning multi-spectral aperture-coded microscope

This chapter describes a second generation scanning multi-spectral aperture-coded microscope (SMACM). SMACM is a pushbroom hyperspectral imager that consists of a coded aperture spectrometer (CAS) interfaced to an exit port of a laboratory-grade microscope. In the CAS, a binary-valued order 64 S-matrix replaces the slit input aperture in a conventional pushbroom imaging system – providing 32 times greater throughput. The S-matrix is a shifted and scaled Hadamard matrix. The CAS has a spectral range of 550 - 665 nm with 1 nm spectral resolution. Pushbroom operation involves mechanically scanning the CAS perpendicular to the spectrometer dispersion direction. A series of scanned two-dimensional (2D) (spatial-spectral) measurements are recorded with the CAS – with an object spectrum dispersed along the columns and a spatial field oriented along the rows. These 2D measurements are reconfigured and a nonnegative least squares (NNLS) algorithm is used for spectral data estimation. The first generation system interfaced the CAS to a rapid-prototyped, custom-built microscope with optical quality and the effective spatial resolution constrained by

a single available objective [19]. The microscope and subsystems were individually mounted to the optical table and during each scan vibration and misalignments were noticed. To address these issues, SmacM was built to provide improved mechanical stability since the CAS was directly connected to the microscope frame. This robust structure helped to reduce mechanical vibrations and further limited the mechanical instabilities to table vibrations. Also, interfacing the CAS to a laboratory-grade microscope enabled an improved effected spatial resolution since the system was not constrained to a single objective. In this chapter, transmissive mask analysis is repeated with SmacM. Also, extended source emissions from fluorescent microspheres and fluorescent cells are explored. SmacM has a sample plane spatial resolution of 15.4 - 1.54 μm, depending on the user-selected objective.

2.1 Introduction

Spectral imaging (SI) spans a wide variety of applications aimed at reconstructing a spectrum at every pixel location in an image for object or feature identification. SI began in the 1960s with remote sensing of natural resources and agriculture monitoring [22–24]. Some military applications include real-time surveillance and reconnaissance [25, 26], while biomedical applications include cancer detection [27, 28], DNA microarray image analysis [29], flow cytometry [30, 31], and pathogenesis of diabetic

retinopathy [32].

Many types of spectral imagers exist for 3D (2D spatial, 1D spectral) data cube generation [33]. Spectral imaging can be separated into three different spectral discrimination categories: filtered, dispersive, and interferometric. Filtered approaches include rotating filter wheels, Fabry-Perot spectrometers, and electronically tunable filters such as acousto-optic tunable filters (AOTFs) or liquid crystal tunable filters (LCTFs). Dispersive instruments employ a prism, grating, or computer generated hologram (CGH) for spectral data mapping across a 2D detector array. Interferometric systems include Fourier-transform spectrometers (FTS) where two beams are interfered. The inverse Fourier-transform of the FTS signal as a function of path delay translates into points on a spectrum. Also, spectral discrimination categories are further partitioned into spatial scanning methods employed for 3D (x,y,λ) data cube acquisition: whiskbroom (point scan), pushbroom (line-scan), and staring (e.g. windowing or framing). More recently snapshot systems have been used in spectral imaging.

There exist advantages and disadvantages for each of the previously mentioned categories – filtered, dispersive, and interferometric. The focus of this section includes filtered and dispersive methods for both scanning and snapshot data acquisition. Filtered scanning systems include LCTFs and AOTFs which suffer from wavelength

switching times and light throughput issues. However, much improvement has been made to AOTFs and LCTFs for spectral imaging applications (e.g. microscopy and remote sensing applications). State-of-the-art AOTF switching times are less than 100 μs with spectral resolution between 1.5 - 3 nm in the spectral range of 450 - 800 nm [34]. LCTF switching times range between 50 - 150 ms with a spectral resolution of .25 - 20 nm depending on the spectral range [35]. Light throughput remains a fundamental issue with any filtered scanning systems, thereby reducing the overall system signal-to-noise ratio.

To overcome the drawbacks associated with filtered scanning systems, dispersive systems are considered. Although dispersive systems provide high-throughput, they are limited by instrument efficiency. Dispersive scanning systems provide high spatial and spectral resolution with a cost in scan time. Dispersive, snapshot and scanning spectral imagers employ a spatial-spectral encoding scheme for object data cube estimation. For example, CASSI [20, 36–38], detailed in Chapter 3, is a prism-based dispersive system that records a 2D spectrally filtered projection of a 3D (x, y, λ) object data cube in a snapshot. The computerized tomographic imaging system (CTIS) [20, 36–38] is another snapshot spectral imager which maps signal from each voxel in an object cube to distinct diffraction patterns onto a CCD detector array using a CGH. Finally, a compact image slicing spectrometer (ISS) [39] is a snapshot

spectral imaging system that uses a custom optic to separate an image into 2D slices and disperses the image, thereby projecting 3D object data onto a 2D detector array. Each of these snapshot spectral imagers contains a spatial-spectral resolution tradeoff compared to scanning systems. Therefore, dispersive scanning systems sacrifice speed for high spatial and spectral resolution, while snapshot spectral imagers sacrifice spatial and spectral resolution for speed. The target application determines which variety is preferred.

This chapter focuses on dispersive pushbroom imaging for complete 3D data cube (x, y, λ) acquisition. Dispersive pushbroom imagers record a series of 2D images (1D spatial, 1D spectral) during scanning. After post-processing and reconfiguring, an object data cube is reconstructed such that a spectrum is provided at each pixel location. More specifically, a pushbroom CAS for hyperspectral imaging is discussed in this chapter [19, 40]. Benefits associated with CAS include photon collection efficiency of diffuse sources and a multiplex advantage [2, 12]. These systems have been used for high throughput analysis of weak and incoherent signals for tissue chemometrics [41], remote sensing of chemicals [42], and longwave infrared spectroscopy [43]. High throughput with the CAS makes it ideal for fluorescence scene analysis.

Previous work in CAS hyperspectral microscopy involved an interface to a rapid-prototyped, custom-built microscope [19,40]. The first generation prototype acquired

and reconstructed data from monochromatically-illuminated chrome patterns on a quartz substrate with a high signal-to-noise (SNR) ratio. While extended source measurements from a nanoparticle aggregate were successfully recorded and a data cube estimate was generated, this chapter describes a mechanically stable second generation system better suited for fluorescence microscopy applications. In this chapter, a scanning multi-spectral aperture-coded microscope (SmacM) contains a CAS robustly interfaced to a laboratory-grade microscope for transmission mask and fluorescence microscopy studies.

This chapter is organized as follows: Section 2.2 reformulates the CAS and push-broom imaging system model. The calibration and post-detection procedure for SmacM are also explored in this section. Further, Section 2.3 describes the system design for the CAS, as well as the interface to a laboratory-grade microscope. Also, spatial resolution limitations of the SmacM system are investigated. Simulated SmacM measurements and reconstruction results are evaluated in Section 2.4. Section 2.5 presents SmacM experimental data from narrowband source illuminated targets and broadband emission from fluorescence targets. Finally, Section 2.6 summarizes the project presented in this chapter.

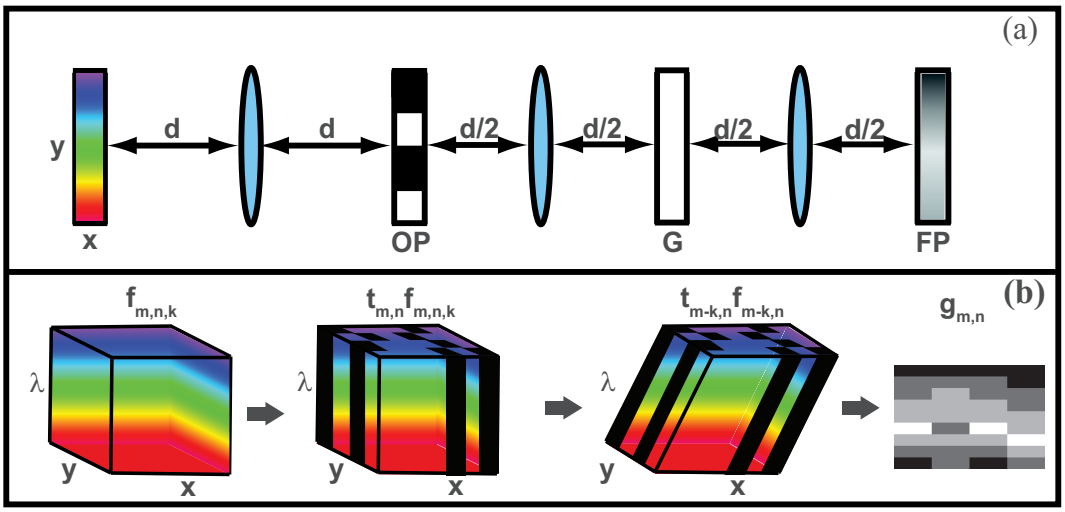

Figure 2.1: (a) Optical architecture for the CAS consisting of an input aperture (OP), grating (G), and a 2D focal plane (FP). (b) Power spectral density profile propagated through the system architecture. The effect of the aperture-code on the power spectral density is shown.

2.2 Mathematical system model

The mathematical system model for coded aperture systems has already been explored [2, 12]. This chapter summarizes the mathematical model for the CAS and describes the system model for CAS pushbroom operation, data inversion, and data cube generation. For CAS, intensity-valued measurements at the detector array are expressed as a convolution between the input source spectrum and the input aperture-code. In SmacM, the CAS contains an aperture-code that is a binary-valued order 64 S-matrix. The S-matrix is a shifted and scaled Hadamard matrix containing mutually orthogonal rows. The aperture-code spatially maps the input source spectral density onto the two-dimensional (2D) detector array. Each row of measurements

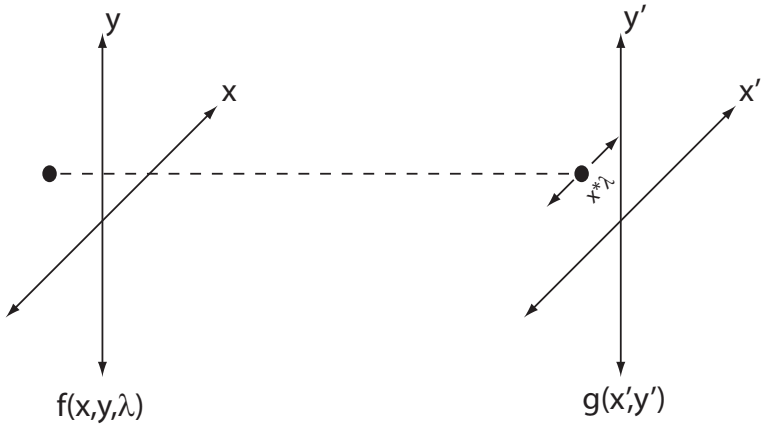

Figure 2.2: Object data point mapping onto a 2D detector plane. Location of the object data point along the y-axis remains constant, while the point along the x-axis is dependent upon λ at x. This dependence is due to the grating linear dispersion occurring along the x-axis. This diagram is a pictorial representation of the shift-invariant impulse response h for the CAS.

recorded at the detector array represents independent projections of spectral channels as a function of spatial location. Intensity-valued measurements recorded with the CAS (see Fig. 2.1) are modeled as:

$$g(x', y') = \iiint dx\ dy\ d\lambda\ t(x, y)\ f(x, y; \lambda)\ h(x, x', y, y'; \lambda) p_{m,n}(x', y'), \qquad (2.1)$$

where $h(x, x', y, y'; \lambda)$ is a linear shift invariant impulse response representing propagation through unity magnification optics, $t(x, y)$ describes the aperture-code transmittance function, $f(x, y; \lambda)$ is the input source spectral density, and $p_{m,n}(x', y')$ represents the detector sampling function. In the system model describing the CAS shown in Fig. 2.1, the transformation along the y-axis is held constant and the mapping along the x-axis is defined by the propagation kernel. The propagation kernel,

$h(x, x', y, y'; \lambda)$, for the CAS is defined as:

$$h(x, x', y, y'; \lambda) = \delta(y - y')\delta(x - (x' - \xi(\lambda - \lambda_c))), \tag{2.2}$$

where ξ represents the grating linear dispersion. The system response to a spectrally distinct point object is shown in Fig.2.2. Linear dispersion (ξ) is derived from the grating equation (see Appendix A.1 for derivation)

$$\sin(\theta_I) + \sin(\theta_R) = \frac{\kappa\lambda}{\Lambda}, \tag{2.3}$$

and is defined as

$$\xi = \frac{\delta x}{\delta \lambda} = \frac{\kappa F}{\Lambda \cos(\theta_R)}, \tag{2.4}$$

where the incident angle $\theta_I = 0$, λ is the operating wavelength, κ represents the grating diffraction order, F represents the output focal length of the imaging lens before the detector, Λ is the grating period, and θ_R is the reflected angle from the grating given the spectrometer center wavelength (λ_c). The transmittance function for the aperture-code, $t(x, y)$, is modeled as:

$$t(x, y) = \sum_i \sum_j t_{i,j} rect\left(\frac{x - i\Delta_m}{\Delta_m}, \frac{y - j\Delta_m}{\Delta_m}\right), \tag{2.5}$$

where Δ_m is the aperture-code pitch and $t_{i,j}$ represents an amplitude-value at the $(i,j)^{\text{th}}$ position in the aperture-code. The transmittance aperture-code amplitude, $t_{i,j}$, is based on the $(i,j)^{th}$ values in the S-matrix independent column code and is defined as:

$$t_{i,j}(:,j) = \frac{1}{2}\left(1 - H_A(:,j)\right), \tag{2.6}$$

where H_A describes a Hadamard matrix of order A and j represents the columns of the aperture-code. The normalized Hadamard matrix is generated using the 'hadamard' command in MATLAB. A shifted and scaled Hadamard matrix generates an S-matrix as denoted in Eq. (2.6) (see Appendix A.2 for S-matrix implementation).

Since a detector array records an intensity-valued image onto a 2D rectangular grid, the detector sampling function is modeled as

$$p_{m,n}(x',y') = rect\left(\frac{x' - m\Delta_D}{\Delta_D}, \frac{y' - n\Delta_D}{\Delta_D}\right), \tag{2.7}$$

where Δ_D describes the detector pixel pitch. Incorporating expressions for $t(x,y)$, $h(x,x',y,y';\lambda)$, and $p_{m,n}(x',y')$ into Eq. (2.1) yields:

$$\begin{aligned} g_{m,n} &= \sum_{i,j} t_{i,j} \iint dx'\, dy' \text{rect}\left(\frac{x' - \xi(\lambda - \lambda_C)}{\Delta_m}, \frac{y' - j\Delta_m}{\Delta_m}\right) f(x' - \xi(\lambda - \lambda_C), y') \\ &\quad \times p_{m,n}(x',y'), \end{aligned} \tag{2.8}$$

where $g_{m,n}$ represents a 2D discrete detector measurement. The variable k is substituted, $k = \xi(\lambda - \lambda_C)/\Delta_m$, into Eq. (3.1). If mask to detector misalignments and system blur are ignored, the transmittance rectangular function and the detector sampling function in Eq. (3.1) overlap when $i = m - k$ and $\Delta_m = \Delta_D$. Thus, the detector measurements are expressed as:

$$g_{m,n} = \sum_{i,j} t_{i,j}\delta_{i,m-k}\delta_{j,n} \iint dx'dy' f(x' - \xi(\lambda - \lambda_C), y'). \tag{2.9}$$

To further simplify the measurement model, a discrete representation for the source spectral density, $f(x', y', \lambda)$, is adapted. The discrete source spectral density is represented as:

$$f(x' - \xi(\lambda - \lambda_C), y') = \sum_{i,j} f_{i,j}\text{rect}\left(\frac{x' - \xi(\lambda - \lambda_C) - m\Delta}{\Delta}, \frac{y' - n\Delta}{\Delta}\right). \tag{2.10}$$

Again, it is assumed that the rectangular sampling function of the source spectral density overlaps with the aperture-code transmittance function ($\Delta = \Delta_m$). After substituting Eq. (2.10) into Eq. (2.9) the discrete detector measurement simplifies to:

$$g_{m,n} = \sum_{i,j,k} \delta_{i,m-k}\ \delta_{j,n}\ t_{i,j}\ f_{i,j} \tag{2.11}$$

The Kronecker deltas are used to simplify the aperture code (t) and the input source

spectral density (f) in Eq. (2.11) so that the final discrete model is expressed as

$$g_{m,n} = \sum_{k} t_{m-k,n} \; f_{m-k,n}. \tag{2.12}$$

The resultant algebraic model for the detector measurement is

$$g = Hf, \tag{2.13}$$

where g represents the vectorized detector measurement, H represents the spectrally shifted transmittance function (t) in Eq. (2.12), and f represents a vectorized source spectrum. Note that the continuous-to-discrete model has ignored blur and mask misalignments. In practice, system blur and misalignments impact reconstruction efficacy.

Pushbroom operation of CAS is shown in Fig. 2.3 [19]. A pushbroom imager collects a set of 2D images (1D spatial, 1D spectral) across a field-of-view (FOV) to estimate spectra and construct a data cube. For pushbroom operation, the CAS is translated along the y-axis (perpendicular to the dispersion direction) in Δ-increments. A y-axis linear scan provides measurement diversity. Each scanned 2D image represents row modulation of the object data with a different row of the aperture-code as shown in Fig. 2.3. A series of scanned measurements form an image composite where every

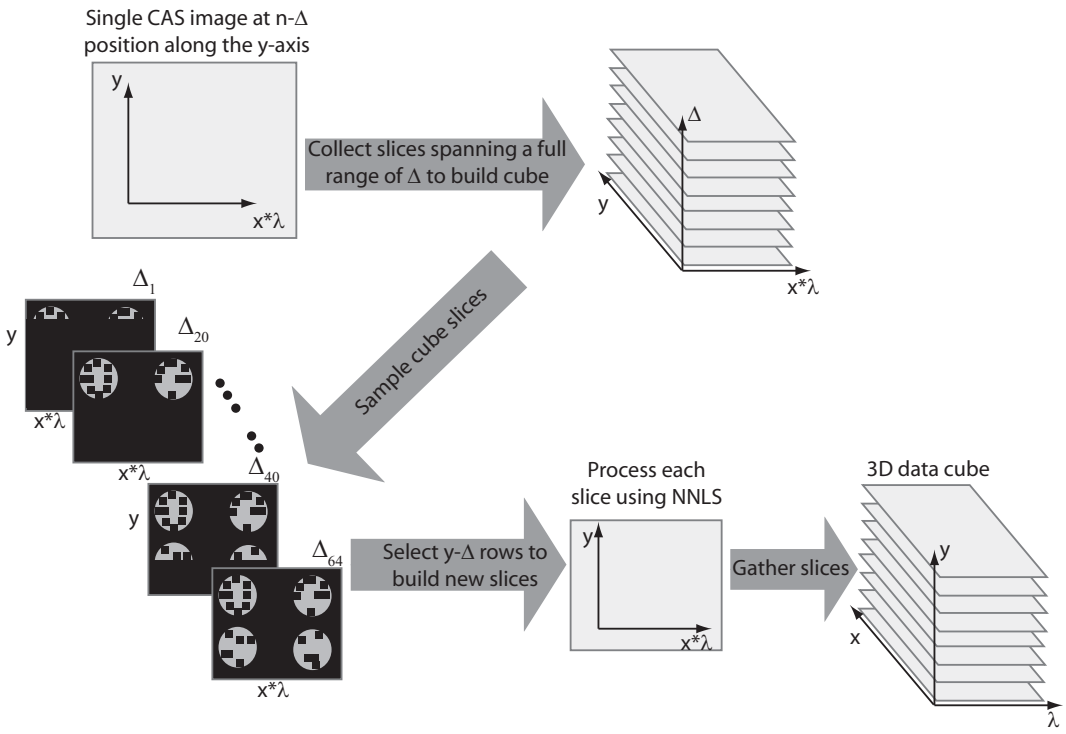

Figure 2.3: CAS pushbroom data collection and inversion flow diagram

row of the object data is modulated by every row in the aperture-code. A set of scans measures independent projections at each row of the aperture-code with respect to the object data. The discrete detector measurement shown in Eq. (2.12) is modified to account for translation along the y-axis and is denoted by

$$g_{m,n-\Delta} = \sum_{k} t_{m-k,n-\Delta} \; f_{m-k,n-\Delta}. \tag{2.14}$$

The scanned detector measurements can not be processed directly. The next section will discuss the method used to reconfigure the recorded images for spectral data inversion and data cube construction.

2.2.1 Calibration and reconstruction

This section describes the calibration procedure, the inversion scheme, and the data cube assembly procedure. Note that the convolution integral in Eq. (2.1) shows that the input source is convolved with the CAS input aperture-code. Therefore, sources with spectrally narrow peaks provide aperture-code features that are well registered to the detector plane. Spectrally broad sources, however, result in dispersed/smeared aperture-code features across the detector plane. This smeared data presents a challenge for mask feature registration. As a result, a procedure was adopted for data collection, calibration, spectral estimation, and data cube generation.

First, pushbroom imaging involves recording a series of 2D (spatial-spectral) detector measurements. Note that the set of scanned images along the y-axis represent a set of 2D multiplexed measurements of the mask-modulated object spectrum as shown in Fig. 2.3. During data acquisition, the CAS was scanned along the y-axis in Δ-increments. Snapshots collected with the CAS can not be directly inverted. Data manipulation of the recorded set of images is detailed in the post-detection procedure.

Second, a CAS 2D image of a spectrally narrow calibration source is used to vertically and horizontally register aperture-code features to the detector plane. The 2D snapshot was taken when the CAS was aligned with the central position of the

intermediate image plane at the microscope exit port. Note that the calibration source should uniformly illuminate the CAS. Spatial uniformity along both axes (x and y) eliminates any need for scanning. The spectrally narrow source was used to calibrate the wavelength axis and to remove 'smile' curvature. Note that 'smile' relates to image curvature of the aperture-code at the detector plane from spatial distortions caused by the dispersive element in the CAS or optical aberrations from the imaging optics [44].

Third, a post-detection procedure was followed for spectral data inversion and data cube synthesis. Post-detection steps include:

- record the indices of the aperture-code active (completely transmissive) and dead (completely opaque) rows registered at the detector plane using the calibration source image

- reorganize the set of scanned measurements such that a single 2D slice within the 3D data cube (x,y,Δ) represents a 2D (x,y) image of a single row (Δ) of object data modulated by every row in the aperture-code (other slices represent subsequent rows of the object data modulation)

- use active and dead row indices to vertically bin the set of scanned 2D detector images to the number of rows (e.g. 64) in the S-matrix

- apply smile curvature correction to each slice in the data
- apply a nonnegative least squares NNLS algorithm to the binned and smile corrected data

Recall that the new 3D data cube (2D spatial, 1D object row index) is configured so that the 2D image at a single object row index represents a mask-modulated object row dispersed along the horizontal axis. Data along the horizontal axis represents the spectrum contained within the object row data as shown in Fig. 2.3. For the CAS, 2D detector images require an inversion scheme for spectral estimation. The spectral data inversion method is a nonnegative least squares (NNLS) algorithm. NNLS is expressed as

$$Minimize \parallel \mathbb{H}f_{(i,:)} - g_{(i,:)} \parallel_2^2, f_{(i,:)} \geq 0, \tag{2.15}$$

where $\mathbb{H}$ represents the 64×64 S-matrix aperture-code, $f_{(i,:)}$ represents the vectorized spectral estimate for the i^{th} row and all columns of the dispersed object data, and $g_{(i,:)}$ represents the vectorized result from the i^{th} row and all columns of the object data modulated by every row in the aperture-code. This algorithm is a linear least squares optimization technique with a nonnegativity constraint. The algorithm inverts the data column-by-column and provides spectral estimates of the source row-by-row. The spectral estimates are aligned and a sum is taken along the rows of the final image

to obtain the spectral estimate from the image, as shown in Section 2.5, Fig. 2.13(c-e). After spectral inversion of all object data rows from all slices, the synthesized 3D data cube provides a spectrum at every spatial location within the scanned 2D scene. System simulations demonstrating the post-detection procedure and data cube reconstruction are detailed in Section 2.4.

2.3 System design

2.3.1 Coded aperture spectrometer (CAS) design

An f/7 CAS was designed for SmacM. The CAS optical design was optimized for a spectral range of 550 - 665 nm using the optical design software, *Zemax*. The CAS, shown in Fig. 2.4, has unity magnification from the input aperture (OP) to the focal plane (FP). The aperture-code at the input (OP) to the spectrometer, as shown in Fig. 2.4, is based on an order 64 S-matrix consisting of opaque and transmissive openings. A shuffled version of the S-matrix is used to remove any spatial correlations along the rows and columns of the mask structure [12]. The S-matrix is implemented as a chrome pattern on a quartz substrate with anti-reflective coating to maximize throughput. The smallest mask feature measures 54 μm or six pixels at the detector plane. Dead (completely opaque) rows are included in the aperture-code to account for vertical misalignments. Considering the mask feature size and the number of

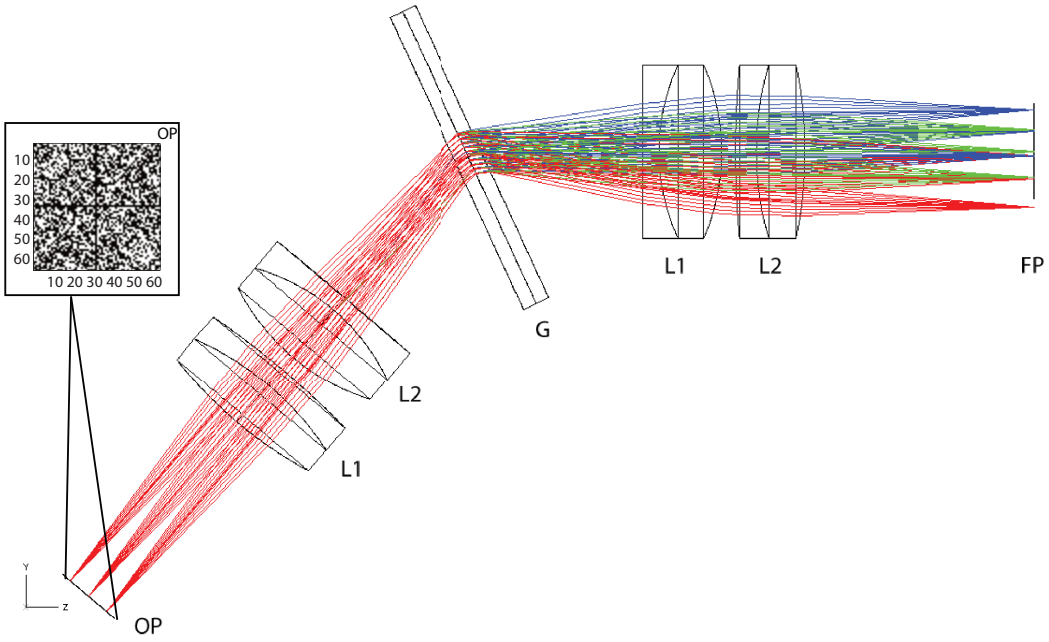

Figure 2.4: Optical design of the f/7 spectrometer showing the object plane (*OP*), collimating optics (L1 and L2), grating (*G*), imaging optics (*L1* and *L2*), and a focal plane (FP).

dead rows, the spatial extent of the mask can be calculated. The mask spatial extent is important for mask design and optical system design. The horizontal (M_H) and vertical (M_V) spatial extent of the mask for the CAS 4f-imaging system is defined by

$$M_V = p[AR + (A-1)D] \tag{2.16}$$

$$M_H = ApR,$$

where p is the detector pixel pitch, A represents mask order, R is the number of active pixels per mask feature, and D is the number of dead rows used in the mask

design. The vertical (M_V) and horizontal (M_H) spatial extent of the mask measures 3.438 mm and 2.304 mm. Light from the mask is directed toward lenses L1 and L2 and collimated onto a holographic transmission grating (G) in Fig. 2.4. The grating provides 0.059 mm/nm linear dispersion which yields 1 nm spectral resolution (see derivation in Appendix A). Note that the number of spectral channels measured by the CAS is determined by the spectral range ($\Delta\lambda$) divided by the spectral resolution. CAS measures 115 spectral channels.

The optical system for the spectrometer was optimized in *Zemax*. Minimizing spot size at the focal plane is of great importance in spectrometer design. Fig. 2.5 shows spot diagrams at five different field positions for three different wavelengths. Field positions are chosen to correspond to edge field points on the aperture-code. Spot size is spatially and spectrally variant. At the center field position, the spot size at 550 nm, 600 nm, and 665 nm is 38%, 7.21%, and 30.02% greater than the diffraction limited spot size (2.44λf/#). Spatial structure (see Fig. 2.5) in each spot diagram corresponds to optical aberrations affecting system performance. Dominant third order (Seidel) optical aberrations include spherical and field curvature.

Another metric for resolution in optical design involves measuring the spatial frequency response of the optical system. A measure of image contrast versus spatial frequency is known as the modulation transfer function (MTF) and is shown in

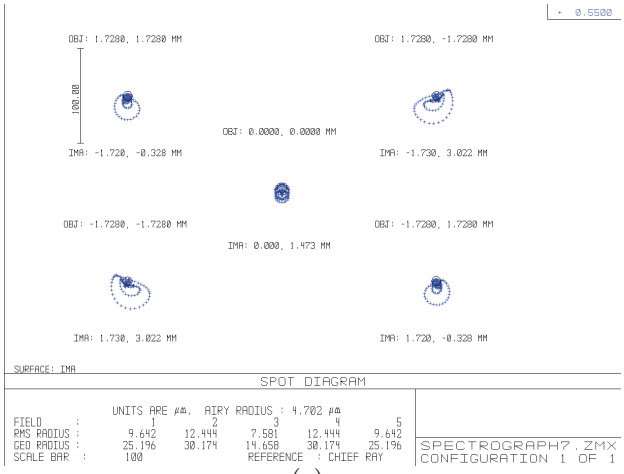

(a)

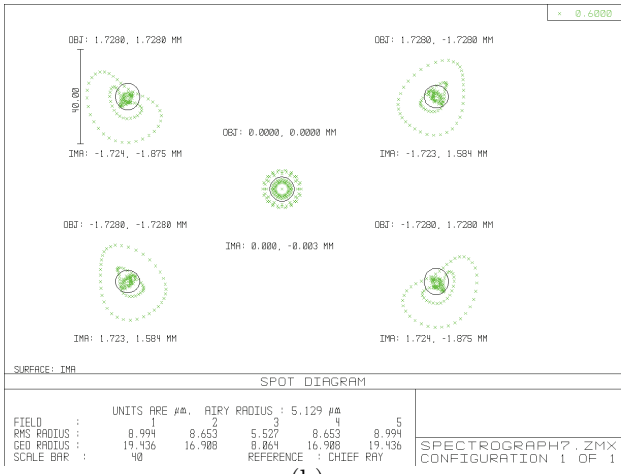

(b)

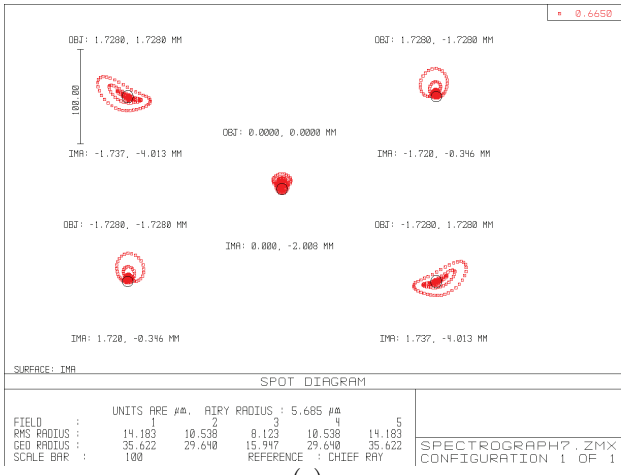

(c)

Figure 2.5: Spot diagrams for various field positions at (a) $\lambda = 550$ nm, (b) $\lambda = 600$ nm, (c) and $\lambda = 665$ nm.

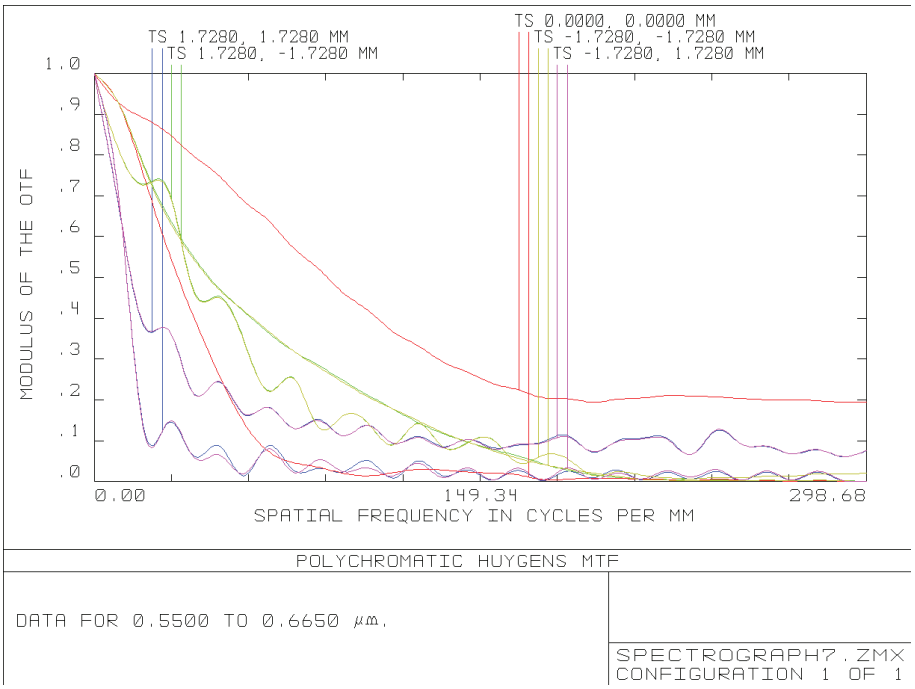

Figure 2.6: Spectrometer MTF plot at all field positions and at three wavelengths (550 nm, 600 nm, and 665 nm) within the prescribed spectral range of the system.

Fig. 2.6 for the CAS. Given a mask feature size of 54 μm, the MTF plot depicts CAS's ability to resolve this feature with high contrast. A CAS mask feature size of 54 μm yields a spatial frequency of 18.52 mm^{-1}. The spatial frequency is obtained by evaluating the reciprocal of the mask feature size. The MTF plot of tangential and sagittal fans at various field positions shows that image contrast at lower spatial frequencies is superior to the performance at higher spatial frequencies. A contrast of 0.8 - 1.0 is obtained at object spatial frequencies as high as 20 cycles/mm. Therefore, the CAS input mask feature size is optimal.

Prescription data from *Zemax* was used to develop a 3D model of the spectrometer

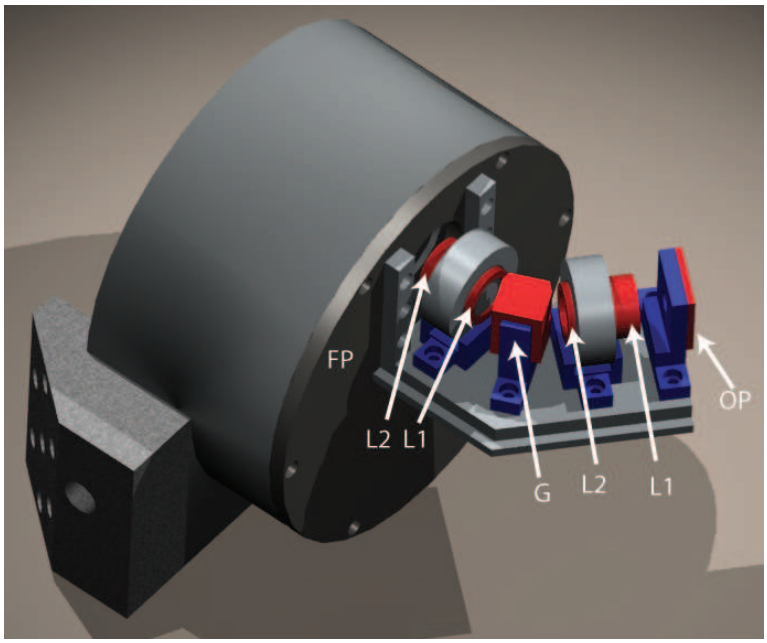

Figure 2.7: *SolidWorks* 3D rendered image of the spectrometer mounted to a CCD.

using a computer automated design (CAD) program, *SolidWorks*. The CAS housing shown in the CAD model was physically constructed using an *Eden 333* prototyping machine. The machine prints a 3D object one layer at a time with an ultraviolet cured photopolymer. A 3D *SolidWorks* rendering of the spectrometer attached to the detector is shown in Fig. 2.7.

2.3.2 Spectrometer and microscope interface

SmacM was robustly constructed by interfacing the custom-built CAS to a laboratory-grade, Zeiss Axioplan 2 microscope as shown in Fig. 2.8(b-c). The optical quality and mechanical structure of a laboratory-grade microscope far exceeds that of the custom-built microscope used in a previous iteration of this experiment [19]. While

the first prototype hyperspectral imager [19, 40] was limited to a single available microscope objective with the custom-built microscope, SmacM contains a CAS that is directly interfaced to a laboratory-grade microscope containing multiple objectives of various magnifications and NA(s). As a result, the optical quality and effective spatial resolution of SmacM was not constrained by a single available objective. A more optimized spatial resolution was realized. Also, good mechanical stability is achieved since the CAS is mounted to a raised baseplate directly supported by the optical table. Mechanical vibrations are thus reduced and largely limited to table vibrations. The CAS was translated at the back-end of the microscope, perpendicular to the grating dispersion direction, via computer-controlled translation. A *Newport* three axis stage and ESP300 motion controller enable adequate alignment of the CAS in both horizontal and vertical dimensions. CAS motion control with the ESP300 was automated over the RS-232 interface using the Matlab *Instrument Control Toolbox*. The maximum velocity was 25 mm/s, however, the velocity was set to 1 mm/s. Translation by a step size equivalent to a mask feature size (e.g. 54 μm) would take 54 ms. CAS scan times were limited by detector integration time rather than the translation speed. Generally, the scan time for the experiments described in this chapter took 10 - 20 minutes.

The Axioplan 2 microscope is also mounted directly to the optical table and

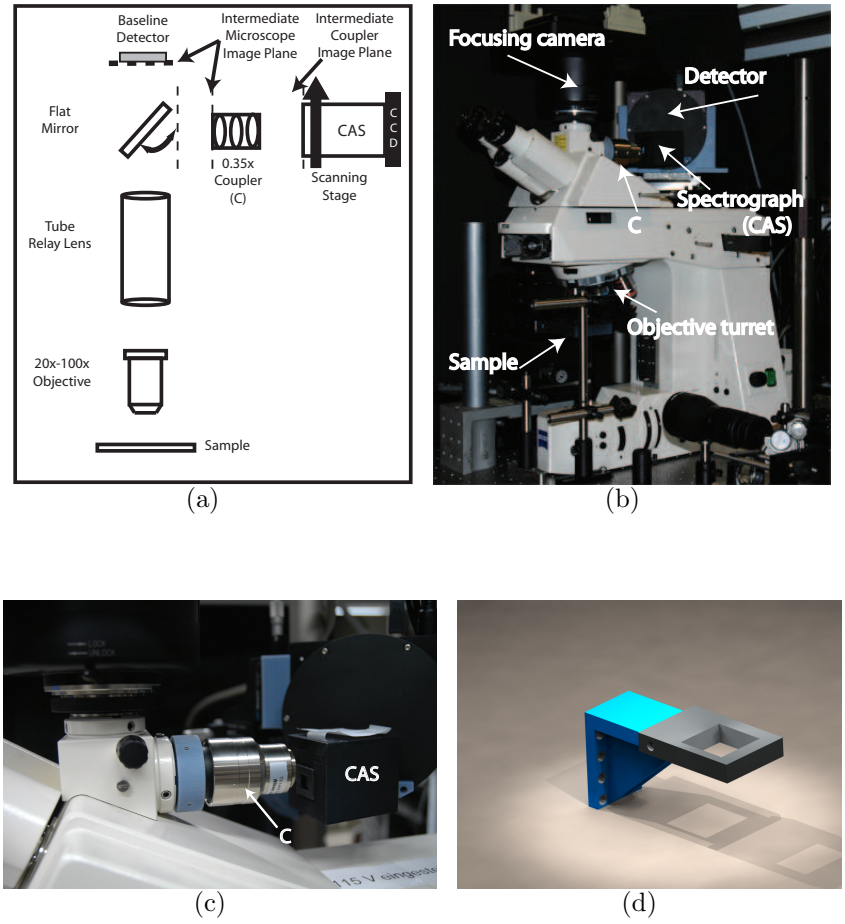

Figure 2.8: (a) Optical schematic for SmacM. (b) Hardware layout for the system. (c) At the intermediate image plane of the microscope, a 0.35× *Nikon* coupler demagnifies the relayed image and maps object data onto the coded aperture spectrometer. (d) CAD rendered image of the sample holder for the microscope.

modified to accommodate laser excitation at the sample plane. The condenser and sample holder were removed from the upright microscope to accommodate a custom sample holder shown in Fig. 2.8. The custom sample holder, fabricated with the *Eden 333* rapid prototyping machine, was attached to a motion-controlled, multi-axis stage for z-axis focus adjustment and transverse sample motion. Sample motion control was again automated over the RS-232 interface. Also, optical field size mismatch between the microscope output port and CAS necessitated coupling optics. A 0.35× Nikon CCTV C-mount coupler demagnifies a 23 mm relayed image to an 8 mm image. Since the coupling optic does not provide a 1:1 correspondence between the field size and aperture-code spatial extent, edges of the relayed object image are not visible to the CAS.

Two detector arrays were interfaced with SmacM. The CAS uses a *Santa Barbara Instruments* (SBIG) cooled scientific-grade Kodak ST-7XME CCD array with a quantum efficiency range of 70 - 75% between 550 - 665 nm. The detector array has a resolution of 510×765 with 16-bit dynamic range and a 9 μm square pitch. Recall that the CAS spectral range ($\Delta\lambda$) is 550 - 665 nm. The largest CCD pixel extent (765 pixels) defines the dispersion axis. For the CAS, the detector pixels along the dispersion direction are binned to 381. Since the CAS measures 115 spectral channels along the dispersion direction, every three spectral channels projected onto the

detector plane measures 1 nm. Automated data acquisition was realized using SBIG drivers accessed from MATLAB. Also, a baseline detector was coupled to a second exit port on the Axioplan 2 microscope. The baseline detector is a SPOT camera with a resolution of 1315×1033 pixels of 6.8 μm square pitch, yielding either a 12-bit grayscale image or a 36-bit color image. The detector has a quantum efficiency range of 20 - 40% between 500 - 600 nm. The SPOT camera uses a liquid crystal tunable filter to generate an RGB image. RGB images with the SPOT camera were not used to compare object data cube reconstructions in this chapter.

2.3.3 SMACM spatial resolution metrics

System spatial resolution factors into system design. Design metrics impacting CAS spatial resolution include: aperture-code feature size (Δf), pixel size (Δp), and spot size (Δr). Spatial resolution, Ω, is determined by the root-mean-square calculation denoted by

$$\Omega = [\Delta f^2 + \Delta p^2 + \Delta r^2]^{1/2}. \tag{2.17}$$

This calculation shows the dominant factor limiting Ω. The aperture-code feature size is determined by the mask feature to pixel ratio - a CAS mask feature maps to six detector pixels (54 μm). The spectrometer spot size is compared to the microscope objective Rayleigh criterion calculation. The microscope objective spot size, Δr,

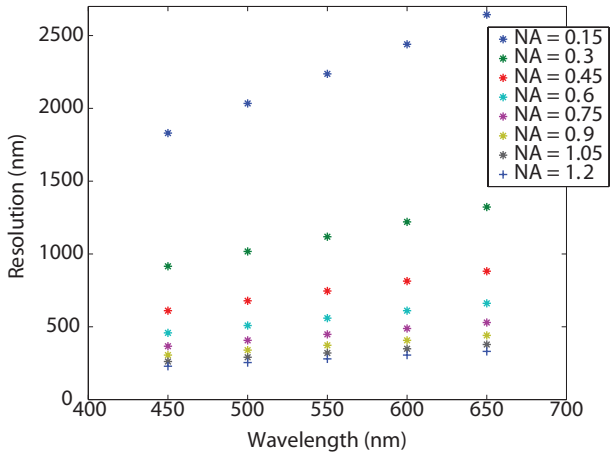

Figure 2.9: Optical resolution limits of different numerical aperture (NA) microscope objectives as a function of wavelength.

lower limit is defined by

$$\Delta r = \frac{0.61\lambda}{(\mathrm{NA})}, \tag{2.18}$$

where λ represents wavelength and NA describes the numerical aperture of the microscope objective. Figure 2.9 shows optical spatial resolution as a function of NA for different wavelengths. We can compare the spectrometer central field spot size (16.25 μm) to the microscope objective Rayleigh calculation with a 0.75 NA objective and a 532 nm illumination wavelength (200 nm). By doing this, we see that the optical resolution of SmacM is limited by the aperture-code feature size ($\Omega = \Delta f$).

The spatial resolution at the microscope sample plane based on the SmacM architecture is found using the aforementioned optical resolution limit. The microscope

object plane spatial resolution (Δs) is calculated by

$$\Delta s = \frac{\Delta f}{MC}, \tag{2.19}$$

where M represents microscope objective magnification and C defines the coupling optic magnification. The available microscope objectives for the Axioplan 2 microscope (10× - 100×) and the coupling optic (0.35×) provide a spatial resolution range of 15.4 μm - 1.54 μm.

2.4 Simulation results

This section presents simulations of SmacM measurements and the post-detection procedure detailed in Section 2.2.1. Spectrally narrow and broad object emissions were evaluated and spectral-spatial reconstruction accuracy compared when measurements are uncorrupted and corrupted by noise.

First, a snapshot detector measurement from a narrow band object spectral density was simulated. A Matlab 64×64 pixel 'Shepp-Logan phantom' image (see Fig. 2.10(a)) with a spatially varying intensity was used as a test object. A CAS detector measurement is simulated by convolving the object spectral signature shown in Fig. 2.10(f) with the object modulated aperture-code shown in Fig. 2.10(d). The object spectral emission, modeled by two Lorentzian functions, contained two peaks

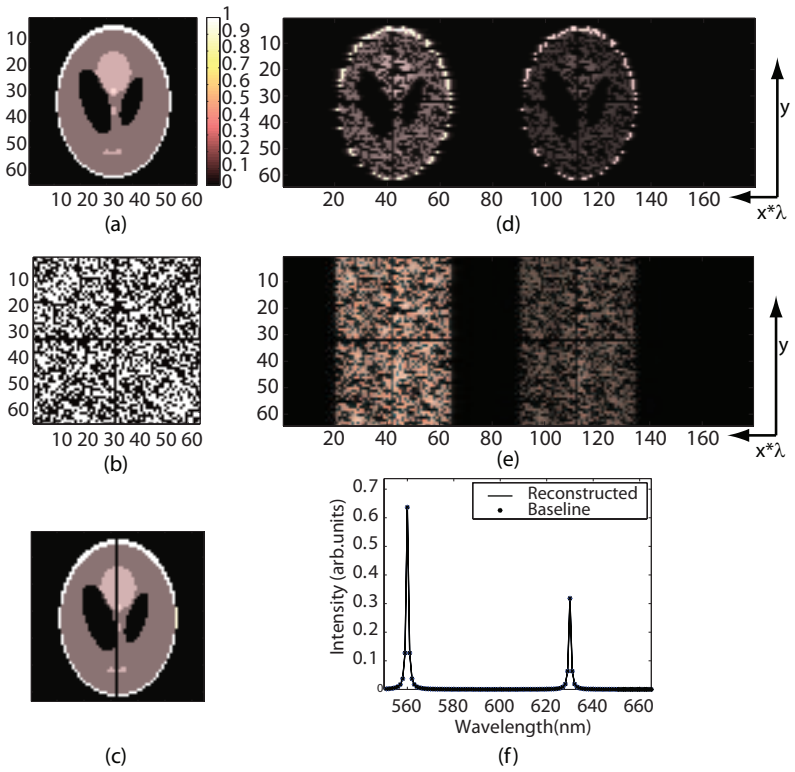

Figure 2.10: Simulated SMACM measurements and reconstructions. (a) A MATLAB 'Shepp-Logan phantom' test image with a spatially varying intensity, as seen in the colorbar. (b) Shuffled, order 64 S-matrix. (c) Multi-spectral 'Shepp-Logan phantom' reconstruction from simulated detector scanned measurements. (d) A subset of scanned measurements across the object data, a sum is taken over the spectral axis. Two 'Shepp-Logan phantom' images with varying intensity represents dispersion from the grating and the intensity variation represents the variation in spectrum intensity. (e) Aperture-code modulation of a single row from the object data over a series of 64 scanned measurements. Two copies appear due to the spectral content of the object row along the x-axis. (f) Reconstructed spectral plot overlayed with the baseline data at a single pixel location in the reconstructed object data cube.

located at 560 nm and 630 nm. Both peaks have different peak intensities and measure a full-width half maximum ($FWHM$) of 1 nm. The baseline spectrum at each pixel location in the 'Shepp-Logan phantom' image is shown in Fig. 2.10(f). Since the object data was not spatially uniform across the vertical axis, pushbroom measurements were simulated for spectral estimation and data cube construction.

The post-detection scheme mentioned in Section 2.2.1 is simulated in this section. For pushbroom measurement simulation, a single row from the object in Fig. 2.10(a) is modulated by the aperture-code and then convolved with the object spectrum. A set of pushbroom measurements is shown in Fig. 2.10(e). Recall that a set of pushbroom measurements represents independent projections of the object spectral data mapped to the detector plane. Several pushbroom measurements, shown in Fig. 2.10(e), were inverted for spectral estimation. Further, the synthetic object was compared with the spectrally summed object data cube estimate shown in Fig. 2.10(c). Reconstruction efficacy is measured using the peak signal-to-noise ratio (PSNR) metric. PSNR is defined as

$$\text{PSNR} \stackrel{\text{def}}{=} 20 \log_{10} \left\{ \frac{\text{MAX}_A}{\frac{1}{n_x n_y} \sum_{i=1}^{n_x} \sum_{j=1}^{n_y} [A_{i,j} - B_{i,j}]^2} \right\}, \tag{2.20}$$

where A represents the synthetic object, B represents the object estimate, n_x and n_y represent the number of detector pixels along each spatial dimension. A PSNR of 20.32 is calculated for the 'Shepp-Logan phantom' image. Much of the error in

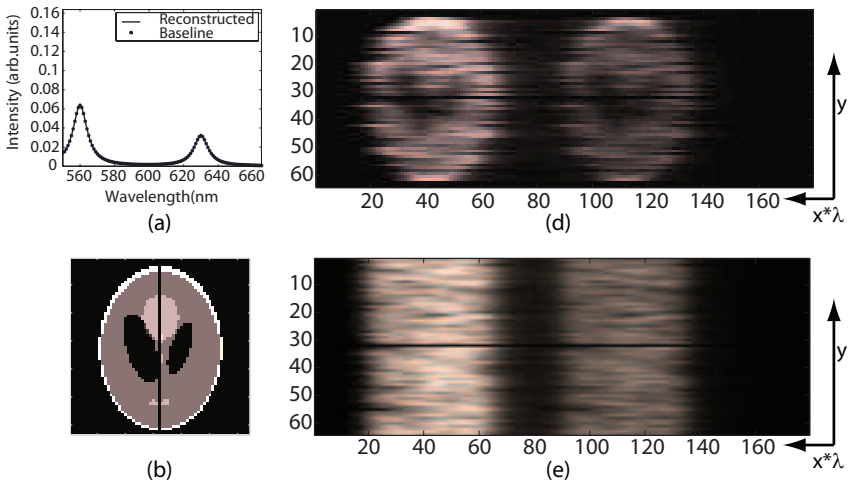

Figure 2.11: SMACM simulations from a spectrally extended input object. (a) Spectral plot at a single spatial location within the estimated object data cube. The NNLS spectral estimate and baseline spectral plot are shown. (b) Reconstructed image estimate of the 'Shepp-Logan phantom' object cube. (c) CAS snapshot showing the object mask-modulated and dispersed image. (e) Aperture-code modulation of a single row from the object data over a series of 64 scanned measurements. Two copies appear due to the spectral content of the object that is dispersed along the x-axis.

the estimate is attributed to the vertical line across the center of the reconstructed image. This vertical line is embedded in the measurement S-matrix and reproduced in each of the pushbroom/vertically scanned images. For this reason, the vertical line appears in the image estimate. The use of a different encoding matrix with no opaque columns would help increase PSNR. Also, spectral reconstruction from NNLS inversion was compared to the baseline spectrum. A single spatial location in the data cube was chosen for the comparison. The similarity between the baseline spectrum and spectral estimate is shown in Fig. 2.10(f). The spectral estimate is an exact reproduction of the baseline spectrum.

Also, pushbroom measurements from spectrally broad object emissions were sim-

ulated. The analysis of spectrally extended objects serves to mimic targets typically analyzed in fluorescence microscopy. Similar to pushbroom measurements from narrowband source simulations, a snapshot CAS detector measurement of a spectrally extended 'Shepp-Logan phantom' test object was generated. The mask-modulated object was convolved with a spectrum to produce the image shown in Fig. 2.11(d). The simulated object spectrum has a Lorentzian lineshape containing two peaks located at 560 nm and 630 nm and a *FWHM* of 10 nm. Figure 2.11(e) shows single row object data dispersed and modulated by every row in the aperture-code, thereby simulating pushbroom operation. Broad spectral emissions generated smeared and dispersed mask-modulated object data since the number of superimposed mask-modulated objects is defined by the spectral linewidth. NNLS inversion was used for spectral estimation of the image in Fig. 2.11(e). In the configured data cube, every spatial location contains a NNLS inverted spectral estimate. The baseline spectrum was compared to the reconstructed spectral estimate in Fig. 2.11(a). Further, PSNR was used to evaluate image reconstruction. A PSNR of 23.69 is calculated for the image estimate. Note that an increase in PSNR was observed for the spectrally broad object emission compared to the spectrally narrow object emission in the case under test. This occurs since the average energy detected with a spectrally extended object is higher than energy from a spectrally narrow linewidth source.

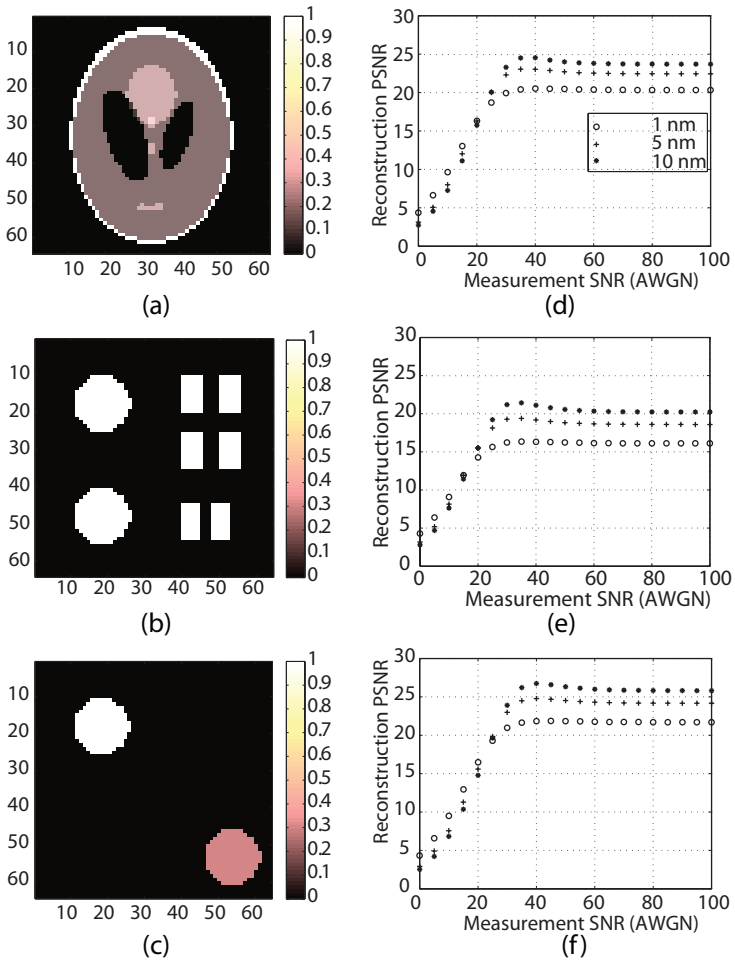

Figure 2.12: SmacM image reconstructions from simulated measurements corrupted by AWGN. Synthetic baseline images include (a) a 2D 'Shepp-Logan phantom', (b) circles and slits, and (c) circles. (d-f) Reconstruction PSNR versus Measurement SNR corrupted by AWGN for spectrally different input object emissions. Note that a decrease in PSNR after a maximum is seen due to the measurement S-matrix central column that is completely opaque.

The impact of additive white gaussian noise (AWGN) on pushbroom CAS measurements was also analyzed. AWGN was used to analyze a photon-limited case typically found in fluorescence microscopy. Recall that the use of an aperture-code in place of a conventional slit in the CAS enables a 32× increase in throughput, thereby presenting an advantage for coded aperture imaging of weakly fluorescent samples. Three different test targets were used to quantify image reconstruction accuracy for spectrally different object emissions. AWGN is generated using the 'awgn' MATLAB command where measurement signal-to-noise ratio (SNR) is an input parameter. The measurement SNR and PSNR are measured in decibels (dB). Figure 2.12 summarizes the results from CAS measurements with AWGN for three different test objects.

Three different test objects (e.g. 'Shepp-Logan phantom', circles/slits, and circle targets) in Fig. 2.12(a-c) were detected with the CAS after pushbroom operation and were corrupted with AWGN in simulation. The object estimates converge at a measurement SNR of about 60 dB for a spectral linewidth of 5 nm and 10 nm. However, all object test targets with 1 nm spectral linewidths converge at a 40 dB measurement SNR. The reconstruction PSNR versus measurement SNR plots for 5 nm and 10 nm spectral linewidths show a decrease in measurement SNR at an SNR range of 20 - 40 dB as shown in see Fig. 2.12(d-f). This decrease occurs after

a maximum value has been achieved. Simulations prove that this phenomenon is caused by the central vertical column in the measurement matrix (S-matrix) that is completely opaque. Simulations without the central opaque vertical column showed that the aforementioned phenomenon disappears.

Simulations in this section enabled the analysis of narrowband and wideband source emission. The behavior of CAS pushbroom measurements to narrowband and broad sources was quantified. Also, NNLS spectral reconstruction accuracy was measured for the case when detector measurements were corrupted and uncorrupted by noise. Simulations base on other sample conditions would improve the analysis of the CAS pushbroom imager.

2.5 Experimental results

Simulations from the previous section motivate experiments for narrowband and broadband spectral analysis. Also, the simulations helped to shed some light on algorithm performance for data cube estimation of spatially and spectrally extended objects. For fluorescent targets, smeared detector measurements are expected and a baseline measurement from a spectrally narrow source is necessary. This section describes calibration data collection, sample illumination geometries, and experimental results with SmacM.

2.5.1 Calibration and sample illumination

CAS calibration data frames were acquired with a krypton discharge lamp. The lamp was placed below the sample holder and directed towards the microscope objective. At the exit port of the microscope, a one inch field uniformly illuminated the input aperture of the CAS and a single detector measurement was recorded. Figure 2.13(a) shows the superposition of two mask patterns recorded at the detector plane – a convolution between the source and input aperture. Spatial uniformity of the source removed the need for vertical scanning. Note the smile curvature (parabolic curvature) at the right side of the image. Also, grating vertical misalignments are evident in Fig. 2.13(a) from the incomplete overlap of the superimposed and shifted mask images.

In the post-detection scheme, the CAS krypton discharge lamp data was vertically binned to match the number of rows in the order 64, S-matrix for spectral estimation. After NNLS inversion was applied to the data, spectral estimates along each row were calculated from each column of the image data as shown in Fig. 2.13(b). After aligning the spectral estimates (see Fig. 2.13(c)), a sum was taken along the rows of the estimated data as shown in Fig. 2.13(d-e). Summation along the rows provided a spectral estimate of the calibration source. Since a calibration source was used, the reconstructed peaks are mapped to wavelength locations using the 'polyfit' (a polyno-

mial fit) command in MATLAB. This command creates a polynomial fit between the peak locations obtained from NNLS spectral estimates and krypton lamp emission peak wavelengths as shown in Fig. 2.13(e). The peak krypton lamp wavelengths were obtained from the NIST spectral database. The calibration spectrum polynomial fit showed that higher spectral channels (e.g. 220) in the data corresponded to blue-shifted wavelengths and lower spectral channels (e.g. 170) correspond to red-shifted wavelengths. Note that two spatially overlapping monochromatic laser sources can be used for wavelength calibration if a discharge lamp is unavailable.

Once a calibration image was obtained, a sample illumination geometry was configured. For sample analysis, test targets and fluorescence microscopy slides were placed on a custom-built sample holder (see Fig. 2.8(d)) and were illuminated in two different ways. Chrome-on-quartz calibration targets were illuminated with a HeNe laser or HeNe/green HeNe laser combination. The laser beam(s) were directed towards the sample plane of the microscope for transmission illumination. Fluorescence samples were excited via darkfield illumination. This method employed a 5 W frequency-doubled solid state Nd:YVO_4 (neodymium yttrium vanadate) laser. The laser obliquely illuminated a small FOV within the sample. High power laser illumination enabled maximum excitation efficiency of the fluorescent markers.

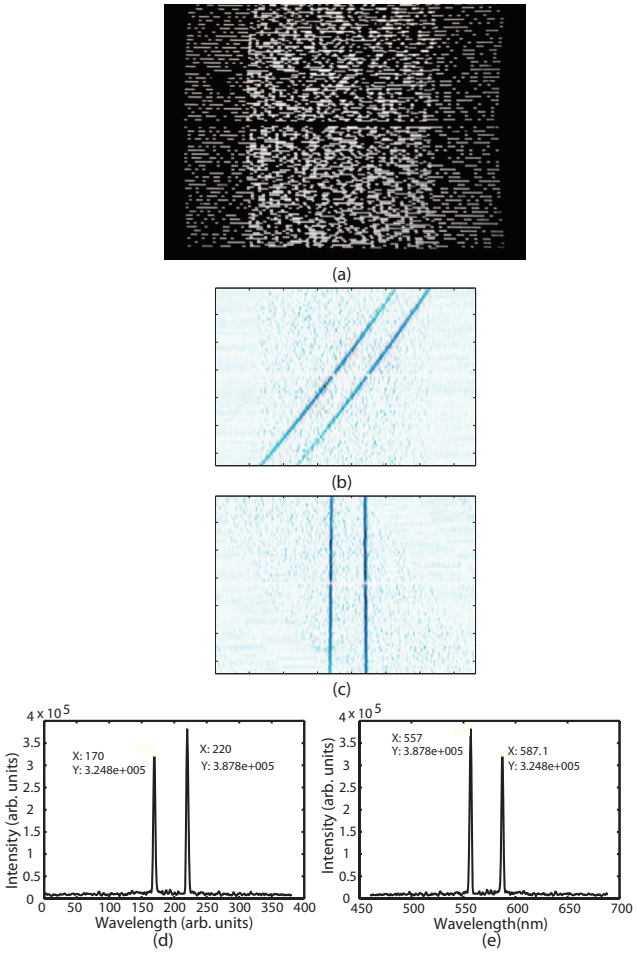

Figure 2.13: NNLS data inversion. (a) Cropped image of a CAS response to a Krypton lamp source. (b) Spectral estimates calculated using NNLS. (c) Aligned spectral estimates. (d) Summation of the spectral estimates provided a spectral profile. (e) Calibrated spectral profile generated using the 'polyfit' function in MATLAB to interpolate known spectral peaks for the Krypton lamp with locations from the reconstructed spectrum for the source (peak location 170 in (d) becomes 587.1 nm and peak location 220 becomes 557 nm.

2.5.2 Narrow-source illuminated calibration targets

Two chrome-on-quartz transmission masks were illuminated with laser light. Each 64×64 pixel mask (spatial extent of 57.6 μm) was imaged with a 20× microscope objective. For SmacM pushbroom operation, the CAS at the exit port of the microscope was scanned a total of 223 steps (a 12 mm vertical spatial extent) along the y-axis.

As a first test, a fractal mask pattern was illuminated by a 10× beam expanded HeNe laser. Using the post-detection procedure detailed in Section 2.2.1 and simulated in Section 2.4, a reconstructed HeNe spectrum is shown in Fig. 2.14(a). The spectral plots correspond to single spatial locations within the estimated object data cube. The amplitude spectral plot in Fig. 2.14(a) shows an "on" spatial location within the fractal pattern object data cube where HeNe light is transmitted. The peak in the figure is attributed to the HeNe wavelength (632 nm). Figure 2.14(b) shows an amplitude spectral plot corresponding to the background signal. Note that noise artifacts appear in both spectral plots adjacent to the maximum-valued peaks. This noise is attributed to algorithmic noise produced by system misalignments (e.g. grating misalignments, calibration source misalignments, or CAS scanning misalignments), CAS system blur, or CAS detector noise. Also, laser illumination of the transmission mask creates speckle, as shown in Fig. 2.14(c).

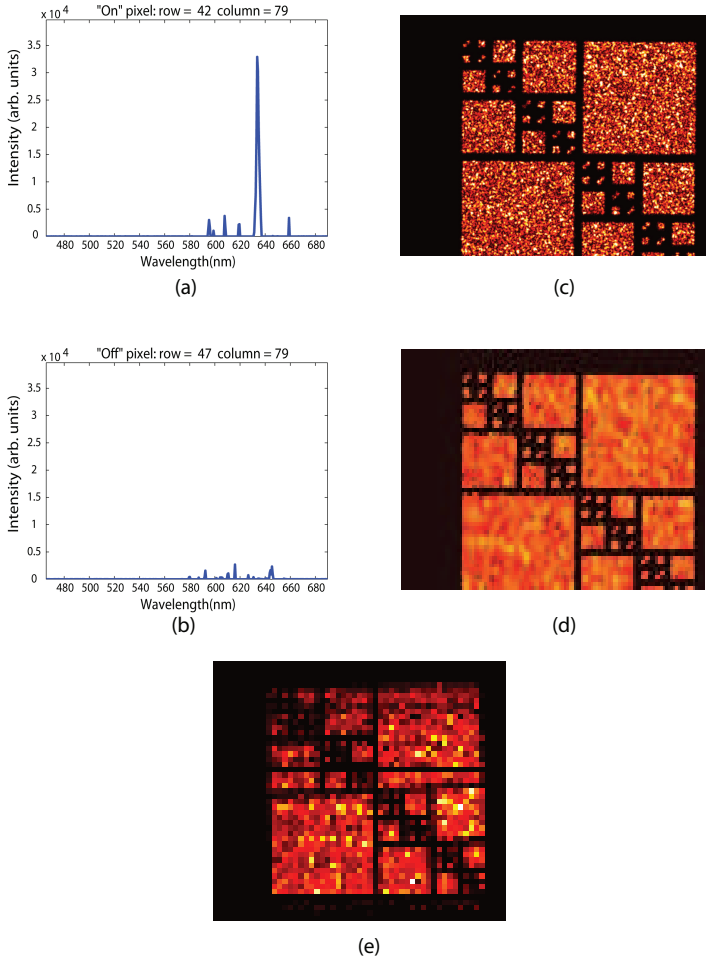

Figure 2.14: (a) "On" and (b)"off" amplitude values from two spatial locations in the reconstructed object data cube as a function of wavelength. (c) SPOT Baseline image of a chrome-on-quartz fractal pattern observed with a 20× objective and 0.35× demagnifier. (d) Downsampled baseline image created to match the resolution of the aperture-coded spectrometer. (e) Reconstruction estimate for a single transverse image at a single spectral channel.

A baseline image from the SPOT detector is shown in Fig. 2.14(c). The baseline image was downsampled to match the CAS image resolution as shown in Fig. 2.14(d). Figure 2.14(e) represents the maximum-valued image estimate along the spectral domain of the object data cube. A comparison was made between the SPOT baseline detector image in Fig. 2.14(d) and the maximum object estimate in Fig. 2.14(e) to evaluate image reconstruction quality. The reconstructed image and the baseline measurement are similar. Laser speckle impacts image quality with the maximum-value image estimate. The cross-hair features in the fractal pattern are distinguished in the maximum-valued image estimate.

A second transmittance mask containing the letters 'DISP' was illuminated with a 10× beam expanded diffuse HeNe and green HeNe laser combination. A CAS snapshot of a mask-modulated and dispersed input source is shown in Fig. 2.15(f). The dispersed 'DISP' mask represents the spectral content contained within the input object source. Using the procedure detailed in Section 2.2.1, spectral estimates were generated and a 3D data cube was created. Figure 2.15(a-d) displays 2D transverse slices along the spectral axis of the data cube. These image estimates were rotated to match the recorded SPOT baseline image in Fig. 2.15(e) and the image slices were scaled by the maximum value of the 3D data cube. Note that Fig. 2.16(a) does not display all 'DISP' letters since the spatial extent of the dispersed green spectral

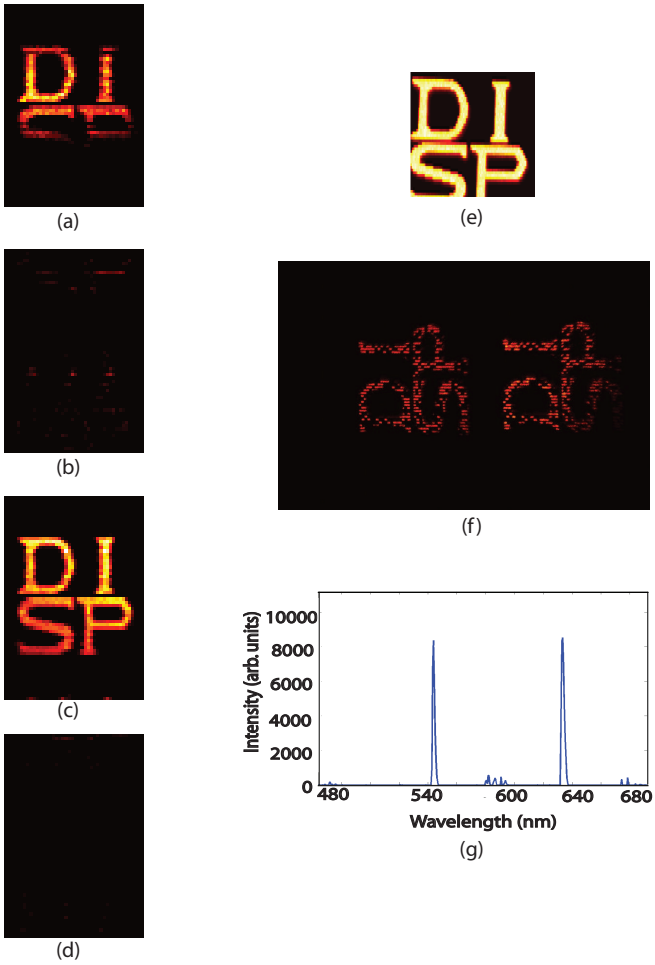

Figure 2.15: Object data cube for a chrome-on-quartz 'DISP' mask illuminated by a green HeNe and HeNe diffuse laser combination. Rotated image at spectral channel (a) $k = 248$ (evidence of green HeNe source), (b) $k = 150$, (c) $k = 97$ (evidence of the HeNe source), and (d) $k = 15$. (e) Baseline downsampled 2D image obtained with the SPOT camera at a slightly different field of view compared to the CAS field of view. (f) Spectral plot at a single voxel in the data cube where a green HeNe laser peak and a HeNe laser peak are shown.

channel of the CAS only partially maps to the edge of the CAS image plane. A downsampled baseline image from the SPOT camera was used to compare transverse slices along the spectral axis shown in Fig. 2.15(a-d). Note that the baseline SPOT image was not ideally matched to the FOV observed by the CAS. The spectral slices, in Fig. 2.15(a-d), spatially reveal the serifs from each letter on the mask. Residual noise artifacts are found in adjacent spectral channels as seen in Fig. 2.15(b,d). These artifacts are attributed to calibration misalignments with respect to scanned measurements and aforementioned system misalignments.

Further, an amplitude spectral plot at a single spatial (x,y) location on the 'DISP' letters is shown in Fig. 2.15(g). Noise artifacts appear in the spectral plot beside each of the maximum-valued spectral peaks. The spectral peaks shown in Fig. 2.15(g) correspond to the green HeNe (543 nm) and HeNe (632 nm) wavelengths. Improved calibration and alignment would minimize the noise contributions found in the spectral plot.

2.5.3 Fluorescence microscopy with SmacM

Fluorescence microscopy of microspheres and cells was realized with SmacM. A frequency-doubled laser at 532 nm was used for darkfield sample illumination. Laser fluence was monitored via a user controlled digital indicator. Laser power at the

sample plane varied between 100 mW to 250 mW. High laser power enabled efficient excitation of fluorescent targets with spectrally varying quantum efficiencies. Fluorescence emission was collected with an LD Epiplan-Neofluar 100×, 0.75 NA or an LD Epiplan 50×, 0.5 NA microscope objective. Objectives were chosen for infinity color correction and long working distances. Long working distances enabled oblique sample illumination. The microscope included a 532 nm laser line notch filter to eliminate unwanted scattered and reflected laser light collected at the microscope sample plane. After filtering, the light was directed toward two microscope exit ports where the CAS and baseline camera were located.

During pushbroom operation, the CAS was scanned a total of 223 steps (a 12 mm spatial extent). Note that translation began above the intermediate image plane of the microscope coupling optic and ended below the intermediate image plane of the coupling optic. CAS detector integration times for each set of scans varied between 1 and 30 s depending on fluorescence signal emission from the sample. Also, a krypton lamp calibration image was taken before each acquired dataset.

An *Invitrogen* solution containing 0.2 μm carboxylate-modified fluorescent microspheres (*fluospheres*) and a fluorescent cell were tested. The fluorescent microspheres were prepared in a 10:1 solution with deionized water. The *fluosphere* solution was UV-excited and a baseline spectrum was recorded with a conventional, *Ocean Optics*

(OO), slit spectrometer; see Fig. 2.16(g). Next, a droplet of poly-l-lysine was placed on the microscope slide for *fluosphere* adhesion. A droplet of the *fluosphere* solution was subsequently added to the microscope slide. Finally, deionized water was used to wash the droplet off of the microscope slide. *Fluosphere* samples analyzed at the microscope sample plane contained dried microspheres. Fluorescent labeled cells required no additional sample preparation.

A microscope slide containing 0.2 μm *fluospheres* was tested with SmacM. Optimal excitation of these *fluospheres* occurs at 540 nm. However, the *fluospheres* were sufficiently excited by 532 nm light due to their broad excitation profile. Post-processed 2D transverse slices along the spectral axis are shown in Fig. 2.16(a-e). A downsampled baseline SPOT detector image (see Fig. 2.16(f)) was compared to the reconstructed 2D images shown in Fig. 2.16(a-e). Recall that from Section 2.3.3, the calculated spatial resolution at the microscope sample plane was 1.54 μm. Therefore, the 0.2 μm fluospheres are diffraction limited test targets for SmacM. To evaluate SmacM spatial resolution performance, the baseline image recorded with the SPOT detector was first analyzed. The only optical element affecting the SPOT detector measurement was the microscope objective. The theoretical spatial extent of the fluosphere after the 100$\times$ microscope objective should measure 20 μm. The 0.2 μm fluosphere at the SPOT detector measured about 24 pixels (spatial extent

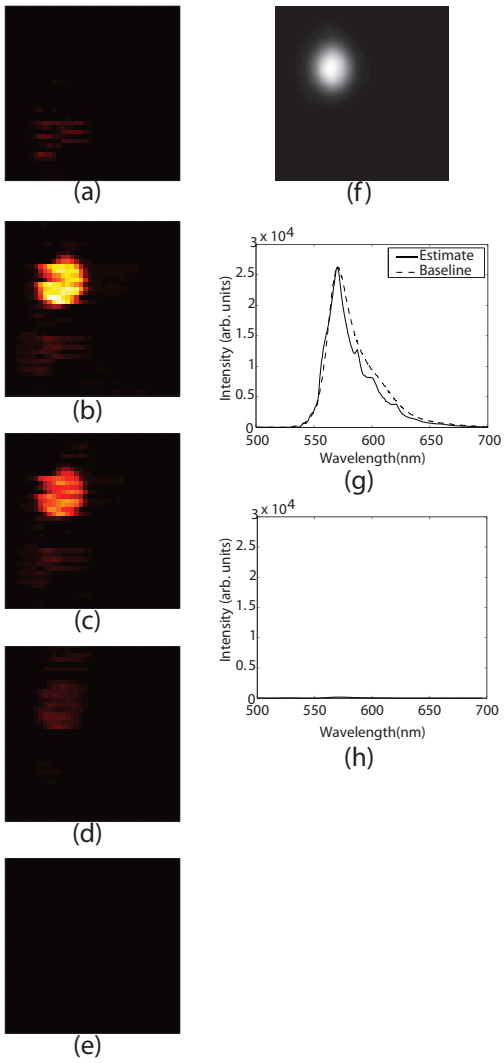

Figure 2.16: Object data cube reconstruction of 0.2 μm fluorescent microspheres excited by 532 nm laser light. Transverse images at spectral channels (a) $k = 268$, (b) $k = 222$, (c) $k = 205$, (d) $k = 128$, and (e) $k = 10$ are shown. (f) Downsampled baseline image from the SPOT camera. (g) Spectral plot for the spatial location row 29, column 57 on the bead overlayed with an OO baseline spectrum. (h) Spectral plot of a background pixel located at spatial position row 29, column 80.

of 163.2 μm). Therefore, the spatial extent of the fluosphere is $8\times$ larger than the theoretical estimate. This suggests that the sample FOV recorded with both the SPOT detector and the CAS was not located at a "best focus" plane. Instead the fluosphere was imaged in a defocused plane. Note that the "best focus" position was empirically found. Comparatively, the theoretical spatial extent of the fluosphere at the CAS, considering the microscope objective and coupling optic, measured 7 μm. The fluosphere spatial extent in the reconstructed 2D image shown in Fig. 2.16(b) measures 486 μm. Since the feature size (54 μm) of the aperture-code is the spatial resolution limit, the fluosphere size is about $8\times$ larger than the predicted value. While sample plane defocus was primarily responsible for the resolution degradation, CAS misalignment along the optical axis and other misalignments were also contributing factors.

NNLS inversion was used to estimate the spectrum of the fluosphere and the background signal. The amplitude spectral plot from a single spatial location in the reconstructed object data was overlayed with a baseline OO spectrum, as shown in Fig. 2.16(g). High correlation was found between the spectral estimate and baseline spectrum. A background amplitude spectral plot is also shown in Fig. 2.16(h).

Lastly, the FluoCell microscope slide #2 from *Invitrogen* containing bovine pulmonary artery endothelial cells was tested. The bovine pulmonary artery endothelial

cells were stained with red-fluorescent Texas Red-X phalloidin for labeling F-actin, mouse monoclonal anti-α-tubulin in conjunction with green-fluorescent BODIPY FL goat anti-mouse IgG for labeling microtubules, and blue-fluorescent DAPI for labeling nuclei. The cell was an interesting spectral source since the sample contained two minimally overlapping fluorescence emissions within the spectral band of the CAS. The cells ranged in size between 6 μm and 20 μm. The CAS is insensitive to the nuclei labeled with DAPI since the emission falls outside of the CAS spectral bandwidth. The excitation and emission *Invitrogen* spectra for the red-fluorescent Texas Red-X phalloidin and the green-fluorescent BODIPY FL goat anti-mouse IgG are plotted in Fig. 2.17. Fluorescence emission from the bovine cell was collected with a 50×, 0.5 NA microscope objective. The post-processed spectral slices from the data cube of the bovine cell are shown in Fig. 2.18(a-e). Recall that higher spectral channels correspond to blue-shifted wavelengths. The transverse image at spectral channel $k = 284$, in Fig. 2.18(b), reveals a brighter image since the dominant feature of the cell is green (see Fig. 2.18(g)). Also, Figure 2.18(d) isolates the contribution in the cell due to the red-fluorescent labeled F-actin. While cell sizes are large compared to the spatial limitations of both the SPOT detector and the CAS, the smaller features of the cell were difficult to distinguish in the reconstructed 2D images at various spectral channels in the object data cube.

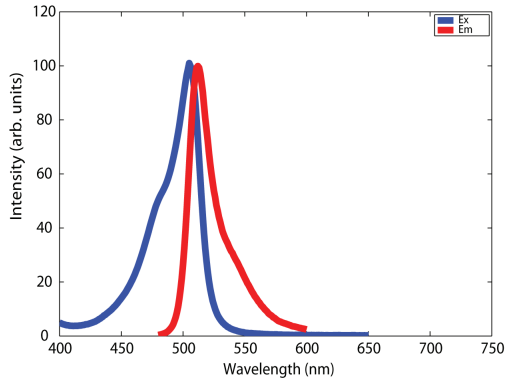

(a)

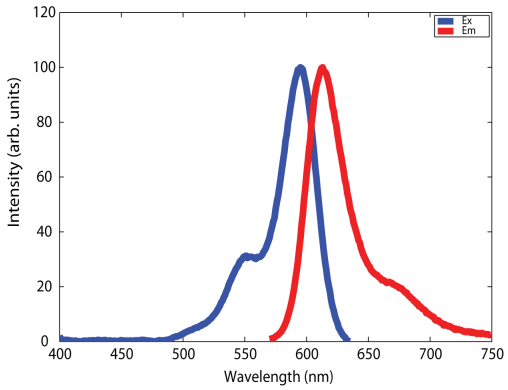

(b)

Figure 2.17: Excitation and emission spectra from (a) the green-fluorescent BODIPY FL goat anti-mouse IgG label and (b) the red-fluorescent Texas Red-X phalloidin label contained in the bovine pulmonary artery endothelial cell, *Invitrogen* FluoCell Slide #2.

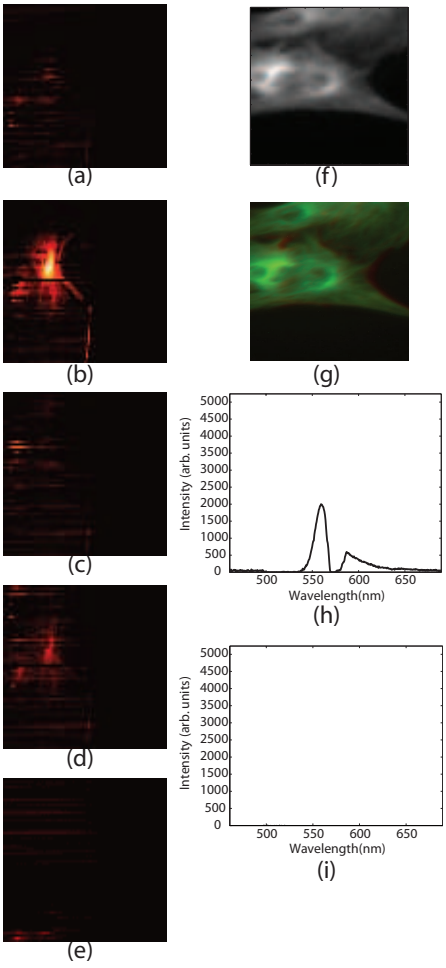

Figure 2.18: Object data cube reconstruction of the *Invitrogen* FluoCell Slide #2 containing bovine pulmonary artery endothelial cells 5 - 20 μm in size. Object data cube reconstruction of spatial slices at spectral channels (a) $k = 313$, (b) $k = 284$, (c) $k = 250$, (d) $k = 200$, and (e) $k = 10$ are shown. (f) Downsampled baseline image from the SPOT camera. (g) RGB rendered image with the SPOT camera. (h) Spectral plot at spatial location row = 10 and column = 8 on the cell and (i) at spatial location row = 13 and column = 80 located in the background of the object data cube.

NNLS spectral estimation provides amplitude spectral plots at three different spatial locations in the object data cube. Figure 2.18(h) displays overlayed spectra from two spatial locations on the cell. Figure 2.18(i) shows the background spectral estimate. The axes for the plots are scaled by the maximum value of the dataset. While the overlayed spectra in Fig. 2.18(h) are of low intensity, the general structure of the spectra resembles the baseline spectra shown in Fig 2.17(a-b). Spatial structure in the cell data cube reconstruction was compared to the baseline SPOT detector image in Fig. 2.18(f-g). Image quality for each spectral slice shown in Fig. 2.18(a-e) is sacrificed due to the pushbroom scan size (54 μm) and spatial resolution limitations of CAS. Finer scans would enable improved spatial resolution along the scan direction.

2.6 Summary

This chapter described a robust CAS interface to an upright laboratory-grade microscope. Simulations motivated measurements for both narrowband and wideband sources with SmacM. SmacM experiments show successful narrow-band target reconstructions and fluorescent microspheres and cellular reconstruction.

Still, system alignment, system blur, and empirical "best focus" adjustments could be improved to increase image spatial registration and NNLS spectral estimation. One option for improved biological sample analysis is to employ a smaller feature size

in the aperture-code or finer pushbroom scanning (< 54 μm). Moreover, a scan time limit was not tested to establish a minimum data acquisition time.

Pushbroom imaging with CAS provides high throughput, high spatial resolution, and high spectral resolution. While high throughput is achieved with the CAS hyperspectral imager, the inherent limitation is scan time. Therefore, dynamic imaging is infeasible with the system described in this chapter.

Chapter 3

Snapshot spectral imaging

Considering SmacM limitations associated with system alignment and scan time, dynamic imaging is infeasible. Motivated by pushbroom system limitations, this chapter describes a coded aperture snapshot spectral imager (CASSI) applied to fluorescence microscopy. CASSI records a two-dimensional (2D) spectrally filtered projection of a three-dimensional (3D) spectral data cube. First, a convex quadratic function with total variation (TV) constraints is minimized for data cube estimation from a 2D snapshot. Second, the TV-minimization algorithm is adapted for direct fluorescent bead identification from CASSI measurements by combining a priori knowledge of the spectra associated with each bead type. In this chapter, the proposed methods create 2D bead maps. Simulated fluorescence CASSI measurements are used to evaluate the behavior of the algorithms. Also, real CASSI measurements of a ten bead type fluorescence scene are recorded and 2D bead maps are created. Baseline images from a filtered-array imaging system verify CASSI's 2D bead maps.

3.1 Introduction

Fluorescence microscopy is a high contrast imaging tool where a light source is used to excite various parts of a sample labeled with fluorescent markers. With the emergence of new fluorescent markers for microscopy applications, one underlying challenge is to identify spectrally overlapping fluorescence emitters. Another challenge involves separating both weak and strong emitters from an autofluorescent background. Spectral imaging (SI) addresses these challenges by reconstructing a spectrum at every pixel location in an image. Most fluorescence microscopy applications associated with spectral imaging create a 2D spectral identity map for an end-user interested in target localization and characterization from a detector measurement. SI emerged in the field of remote sensing [45, 46] and reconnaissance applications [47, 48] and it has recently impacted biomedical imaging in pathology [49], gene mapping [50], and confocal fluorescence imaging of bacteria cells [51].

Traditionally, in SI a three-dimensional (3D) data cube (2D spatial, 1D spectral) is generated via scanning or filter-based approaches. Common scanning methods include tomographic, pushbroom and whiskbroom imaging systems [52–54]. A major drawback of these systems is long acquisition times. In recent advances, spatial and spectral resolution from filter-based systems such as acousto-optic tunable filters (AOTF) and liquid crystal tunable filters (LCTF) have improved, with cost

continuing to be a major drawback [55,56]. Current spectral imaging systems for fluorescence microscopy are scanning confocal systems that combine multiple excitation sources, filters, and a spectrograph for data cube estimation. Recent developments of snapshot spectral imagers address the challenges for both scanning and filter-based approaches [39, 57, 58].

Various coded aperture snapshot spectral imagers (CASSI) have been developed. Initially, a static binary-valued Hadamard mask was used for high-throughput analysis of weak and incoherent sources for spectrum recovery [12]. More recently, a static binary-valued, pseudo-random mask in CASSI was used for video rate spectral imaging of burning candles. The mask then serves as both a high-throughput light collector and as a 3D spatial-spectral data cube encoder. This chapter discusses the use of CASSI for the spectral analysis of microspheres used in fluorescence microscopy [20,36,37]. CASSI overcomes the drawbacks associated with both scanning and filter-based systems since a data cube is acquired in a snapshot image at a low system cost. CASSI differs from other snapshot spectral imagers [39, 57, 58] with an on-axis architecture, the use of direct encoding to balance tradeoffs in spatial and spectral resolution, and the use of constrained optimization for image estimation. A snapshot architecture makes CASSI well-suited for 3D data cube estimation of dynamic fluorescent scenes.

The CASSI spectral engine uses a pixel coding strategy to record compressive measurements (2D) of a fluorescent scene (3D data cube). These measurements draw upon concepts from a compressive sensing (CS) paradigm where underdetermined measurements allow for highly accurate signal estimation [6, 7]. Compressive measurements captured from CASSI systems use CS inversion with total variation (TV) minimization to reconstruct a 3D data cube from a single 2D image. In previous experiments [36, 37, 59] and for the system detailed in this chapter, a two-step iterative shrinkage/thresholding (TwIST) algorithm is adapted for 3D data cube estimation. A procedure is developed to create a color coded image of the 3D data cube estimate. Also, this chapter discusses an additional adaptation to a CS TV-minimization algorithm for the identification of fluorescent beads. A priori spectral data are incorporated into the inversion process to further impose sparsity along the spectral domain. The imposed sparsity enables a more accurate reconstruction from fewer measurements. A three-step procedure is then applied to the sparse data cube estimate to create a 2D spectral feature map of fluorescent beads. Approaches in this chapter are designed to address applications in fluorescence microscopy associated with spectral data cube estimation and target identification.

This chapter is organized as follows. In Section 3.2, the dual-disperser (DD)CASSI optical architecture is reviewed and the effect of the aperture-code on a source spec-

tral density is described. Section 3.3 summarizes the TV-minimization algorithm for 3D object data cube estimation and explains the adaptation to further impose sparsity on the data cube using a priori spectral information. The generation of a pseudo-colored object data cube and a 2D bead identification map is described. Also, the performance of both algorithms is demonstrated via simulation in Section 3.3. Further, the CASSI-microscope interface is presented in Section 3.4. Section 3.5 provides CASSI spatial resolution limitations. Also, Section 3.5 shows a CASSI pseudo-colored spectral cube map and a fluorescent bead identification map. Baseline images are recorded with two multi-spectral imaging systems. These images are used to verify CASSI bead identification maps. Section 3.6 presents results from dynamic scene analysis with CASSI. Section 3.7 suggests a compact and low-cost CASSI redesign. Finally, Section 3.8 summarizes the work contained in this chapter.

3.2 System model

The system model for a DD snapshot spectral imager has already been developed [20]. This chapter describes a variant on the DD architecture previously discussed – the use of two direct-view double Amici prisms as dispersing elements as shown in Fig. 3.1. The double Amici prisms are of equal and opposite dispersion ($\pm\xi$). The Amici prisms facilitate an on-axis optical architecture. This section provides a summary

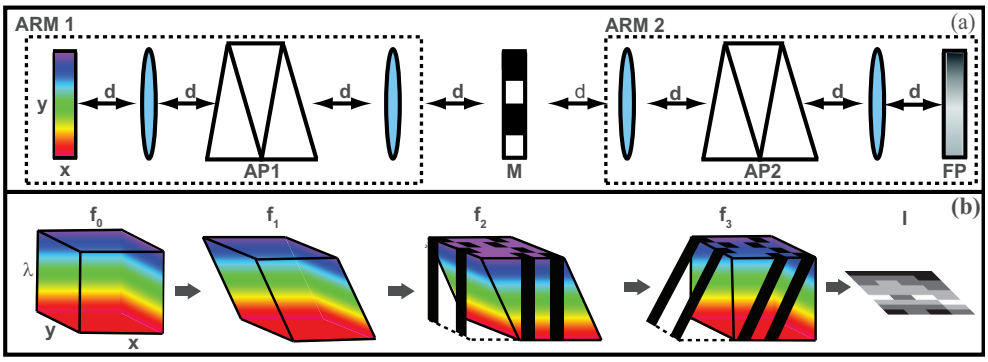

Figure 3.1: (a) Optical architecture for a DD CASSI consisting of two Amici prisms (AP1 & AP2), an aperture code (M) and a focal plane (FP). (b) Power spectral density profile propagated through the system optical architecture. The effect of the aperture code on the power spectral density is illustrated.

for the dual-disperser CASSI system model. An object can be described by a three-dimensional power spectral density, $f_0(x, y, \lambda)$, where x and y denote spatial location and λ represents the wavelength. After the first group of optics in arm 1 (see Fig. 3.1), f_0 is mapped to

$$f_1(x, y, \lambda) = \iint f_0(x', y', \lambda) h_1(x, x', y, y', \lambda) dx' dy'. \tag{3.1}$$

The kernel $h_1(x, x', y, y', \lambda)$ is modeled by a shift invariant impulse response that represents propagation through unity magnification imaging optics and a dispersive element. Diffraction effects in the CASSI architecture and optical aberrations are neglected in the expression for h_1.

$$h_1(x, x', y, y', \lambda) = \delta(x' - [x + \xi_1(\lambda - \lambda_C)])\delta(y' - y). \tag{3.2}$$

Thus far, the system impulse response (h_1) for CASSI is the same as that used in CAS, as previously described in Chapter 2. The main difference is in the location of the aperture-code in the optical architecture. In Eq. (3.2), ξ_1 represents the net dispersion prescribed by the first double Amici prism and λ_C is the system's center wavelength (550 nm). Dispersion by the Amici prism is expressed as $dn/d\lambda$, where n is the index of refraction. Linear dispersion is assumed in this system model for the prescribed spectral range of the instrument. Dispersion in arm 1 is referred to as a *shearing* operation along the x dimension of the optical system. The power spectral density is neither magnified nor dispersed along the y direction. By substituting Eq. (3.2) into Eq. (3.1), f_1 becomes

$$f_1(x,y,\lambda) = \iint f_0(x',y',\lambda)\delta(x' - [x + \xi_1(\lambda - \lambda_C)])\delta(y' - y)dx'dy' \tag{3.3}$$

$$= f_0(x + \xi_1(\lambda - \lambda_C), y, \lambda). \tag{3.4}$$

After the prism, multiple images are formed at wavelength dependent locations. The sheared power spectral density is then modulated by an aperture code. A mask-modulated f_1 is expressed as

$$f_2(x,y,\lambda) = t(x,y)f_0(x + \xi_1(\lambda - \lambda_C), y, \lambda), \tag{3.5}$$

where $t(x, y)$ is the transmittance function of the aperture code. CASSI has a pseudo-random, binary-valued transmittance function defined by

$$t(x, y) = \sum_{ij}^{N} t_{ij} rect\left(\frac{x - i\Delta_T}{\Delta_T}, \frac{y - j\Delta_T}{\Delta_T}\right), \tag{3.6}$$

where t_{ij} is the binary value (0 or 1) associated with either an opaque or transmissive opening on the mask, N refers to the total number of mask elements along each spatial dimension, and Δ_T refers to the mask element pitch. The mask modulation process is referred to as a *punching* operation, where spectral channels are blocked by opaque regions on the mask as a function of spatial location. The optics in arm 2 are meant to undo the dispersion effects from arm 1 (see Fig. 3.1). After the second Amici prism f_2 becomes

$$f_3(x, y, \lambda) = \iint f_2(x'', y'', \lambda) h_2(x, x'', y, y'', \lambda) dx'' dy'' \tag{3.7}$$

$$f_3(x, y, \lambda) = \iint t(x'', y'') f_0(x'' + \xi_1(\lambda - \lambda_C), y'', \lambda) h_2(x, x'', y, y'', \lambda) dx'' dy''. \tag{3.8}$$

Recall that, the Amici prism in arm 2 has equal and opposite dispersion to the Amici prism in arm 1 ($\xi_2 = -\xi_1$). In Eq. (3.8), h_2 is also modeled as the shift-invariant impulse response for the optics in arm 2:

$$h_2(x, x'', y, y'') = \delta(x'' - [x + \xi_2(\lambda - \lambda_C)])\delta(y'' - y). \tag{3.9}$$

Before the detector, f_3 is further simplified to

$$f_3(x, y, \lambda) = f_0(x, y, \lambda)t(x - \xi_1(\lambda - \lambda_C), y). \tag{3.10}$$

A spectrally dependent filter function is described as $H(x, y, \lambda) = t(x-\xi_1(\lambda-\lambda_C), y)$. The application of a 2D aperture-code in a dispersive, intermediate image plane of CASSI creates a 3D spectrally shifted filter function that modulates a 3D power spectral density. Since the detector is insensitive to wavelength, the power spectral density at the detector is integrated along the wavelength dimension.

$$g(x, y) = \int f_0(x, y, \lambda)H(x, y, \lambda)d\lambda. \tag{3.11}$$

The spectral integration process at the detector is referred to as a *smashing* operation. Therefore, an intensity value at every pixel location is recorded at the detector. Since the measurements at the detector are spatially pixelated, detector measurements are modeled as

$$g_{mn} = \iiint t(x - \xi_1(\lambda - \lambda_C), y, \lambda)f_0(x, y, \lambda)p_{mn}(x, y)dxdyd\lambda, \tag{3.12}$$

where p_{mn} represents the detector sampling function at the $(m,n)^{th}$ location as described by

$$p_{mn}(x,y) = rect\left(\frac{x-m\Delta}{\Delta}, \frac{y-n\Delta}{\Delta}\right), \tag{3.13}$$

and Δ represents the detector pixel pitch. Substituting Eq. (3.13) and Eq. (3.6) into Eq. (3.12), results in

$$\begin{aligned} g_{mn} &= \sum_{ij} t_{ij} \iiint rect\left(\frac{x-\xi_1(\lambda-\lambda_C)-i\Delta_T}{\Delta_T}, \frac{y-j\Delta_T}{\Delta_T}\right) rect\left(\frac{x-m\Delta}{\Delta}, \frac{y-n\Delta}{\Delta}\right) \\ &\quad \times f_0(x,y,\lambda)dxdyd\lambda. \end{aligned} \tag{3.14}$$

Next, the mask element pitch (Δ_T) and the detector pixel pitch (Δ) are assumed to be equal ($\Delta_T = \Delta$). Ideally, a relationship between the mask and detector sampling functions is established to simplify the expression in Eq. (3.14). To do this, a substitution is made for k such that $k = \xi_1(\lambda-\lambda_C)/\Delta$. After substituting k into Eq. (3.14), the equation becomes

$$\begin{aligned} g_{mn} &= \sum_{ij} t_{ij} \iiint rect\left[\frac{x-(k-i)\Delta}{\Delta}, \frac{y-j\Delta}{\Delta}\right] rect\left[\frac{x-m\Delta}{\Delta}, \frac{y-n\Delta}{\Delta}\right] \\ &\quad \times f_0(x,y,\lambda)dxdyd\lambda. \end{aligned} \tag{3.15}$$

The sampling functions for the aperture code and the detector overlap when $m = k-i$ and $j = n$. In order to create a discrete representation of f_0, $x' = x-m\Delta$, $y' = y-n\Delta$

and $\lambda' = \lambda - k\Delta$ are substituted into Eq. (3.15) to yield

$$g_{mn} = \sum_{ij} t_{ij}\delta_{i,k-m}\delta_{j,n} \int\int\int f_0(x' + m\Delta, y' + n\Delta, \lambda' + k\Delta) rect\left[\frac{x'}{\Delta}, \frac{y'}{\Delta}\right] dx'dy'd\lambda', \tag{3.16}$$

where Δ again represents the detector pixel pitch. A discrete representation (f) for the 3D object distribution (f_0) is modeled as

$$f_{m,n,k} = \int\int\int f_0(x' + m\Delta, y' + n\Delta, \lambda' + k\Delta) rect\left[\frac{x'}{\Delta}, \frac{y'}{\Delta}\right] \delta(\lambda' + k\Delta) dx'dy'd\lambda'. \tag{3.17}$$

The detector measurements are further simplified using the following equations:

$$g_{mn} = \sum_{ijk} t_{i,j} f_{m,n,k}\delta_{i,k-m}\delta_{j,n} \tag{3.18}$$

$$g_{mn} = \sum_{k} t_{k-m,n} f_{m,n,k}. \tag{3.19}$$

This discrete model for CASSI measurements describes the effect of the aperture-code on an input power spectral density. Compared to the CAS discrete model described in Chapter 2 where a spectrally shifted object is modulated by a shifted aperture-code, CASSI measurements modulate an unshifted object spectral density by a spectrally shifted filter function (t). Since the aperture-code function (t) is defined as a 3D filter function (H) in Eq. (3.11), CASSI measurements may be

algebraically written as

$$g = Hf. \tag{3.20}$$

Note that diffraction effects located at the sample plane of the microscope are relayed to the image plane of CASSI. These diffraction effects are not incorporated into the CASSI system model. Diffracted objects at the sample plane appear defocused at the CASSI image plane. A defocused object results in a larger spectrally encoded object detected by CASSI. An enlarged object does not impact the 3D data cube estimation algorithm or the spectral feature identification algorithm detailed in this paper.

CASSI measures a smaller number of voxels than is required to represent the signal f. A CS inversion scheme is used to solve this underdetermined problem using TV-minimization. Post-processing steps to generate a spectral feature map from a 3D data cube estimate are discussed in the next section.

3.3 Reconstruction procedure and simulation results

3.3.1 3D data cube estimation algorithm

This section describes the TwIST TV-minimization algorithm [59] adaptation for data cube estimation from a single 2D image [37]. The data-cube estimate provides a spatial (x, y) and spectral (λ) representation of an object. Using TwIST [59], a convex objective function is minimized. TwIST is defined by

$$f^* = \arg\min_f \parallel g - Hf \parallel_2^2 + \tau\Phi_{TV}(f), \tag{3.21}$$

where, f^* is the data cube estimate, H is the projection matrix defined by a summation matrix (V) and a calibration cube (C), g is the CASSI measurement and τ is the regularizing parameter. In the nonlinear convex optimization algorithm, TV-minimization is used to find a sparse gradient solution to Eq. (3.21). Φ_{TV} is defined by

$$\Phi_{TV}(f) = \sum_k \sum_{i,j} \sqrt{(f_{i+1,j,k} - f_{i,j,k})^2 + (f_{i,j+1,k} - f_{i,j,k})^2}. \tag{3.22}$$

A pseudo-inverse (H^+) adaptation to the system model, H^+H, (see Appendix A.3) can be used. However, simulations have shown that this adaptation has an extremely high computational cost despite the additive benefit of creating a better conditioned

system matrix. Instead, this section solves Eq. (3.21) to estimate a 3D data cube, f^* by incorporating a $g = Hf$ forward model and $f = C^T V^T g$ transpose model into the TV-minimization algorithm.

Once a data cube estimate (f^*) is found, a procedure is followed to generate a color-encoded representation of the object data cube for display purposes. The colors are based on the reconstructed spectrum per pixel location. Using the spectrum reconstructed at each spatial location in f^*, an adapted RGB code is used to identify each spectrally unique signature in f^*. The adapted RGB code is generated based on the hexadecimal HTML color chart. Note that a baseline spectral database (W) is used to verify spectral plots at spatial locations in the reconstructed object data cube. To generate a color encoded image, a matrix W_f is generated from the spectral database W. The matrix W_f contains columns of spectral vectors $s_n \in \Re^L$, where n describes the number of spectral vectors in the database and L represents the length of spectral data points. W_f consists of L rows and contains $n+1$ columns (i.e. spectral vectors) to account for a background signal and all s_n in the spectral database. Also, an RGB code matrix (G_{RGB}) is generated. The G_{RGB} contains $n+1$ rows and three columns. The adapted RGB matrix provides $n+1$ different hexadecimal HTML colors to RGB values. The left matrix division command was used in MATLAB to generate a matrix inverse (W_{DS}) via a least-squares solution/ pseudo-inverse method.

The left matrix division was applied to the spectral data base matrix (W_f) and the RGB code matrix (G_{RGB}). The matrix inverse, W_{DS}, represents a downsampling matrix. Finally, the spectrum at each $(i,j)^{th}$ spatial location in $f^*(i,j,k)$ is element-wise multiplied by W_{DS} to produce an $f^*(i,j,3)$ data cube. Imaging the resultant data cube provides an $n+1$ psuedo-colored image of the object data cube.

While data cube reconstructions using the above technique were reasonable, 2D TV-minimization does not impose sparsity along the spectral domain. Imposing sparsity on the data cube along the spectral domain was addressed by incorporating prior knowledge into the inversion process as described in subsequent sections.

3.3.2 Direct spectral feature identification algorithm

In fluorescence microscopy, fluorochrome spectral profiles in a sample are known a priori. The a priori knowledge is incorporated into the TV-minimization algorithm to enable more accurate data cube estimation and 2D spectral feature identification. This section aims to describe a three-step procedure that was used to produce a 2D spectral feature map of a fluorescence scene where a unique value at every pixel location only corresponds to one vector in the spectral database, W (see Fig. 3.2).

First, this section describes an adaptation to the 2D TV-minimization algorithm for data cube estimation by incorporating spectral priors into the inversion scheme.

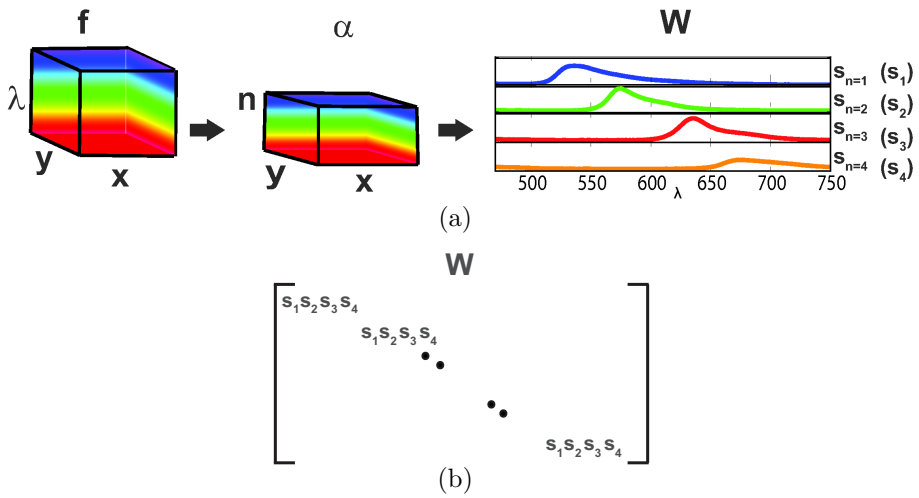

Figure 3.2: (a) Object data cube (f) transformation into a sparse data cube (α) using spectral priors (W). A spectrum recorded at a single pixel location in f corresponds to a single pixel value and bead identity in α. (b) Matrix representation of the spectral data base, W. W can be thought of as a spectrum look-up table.[†]

To do this, an object data cube, $f(i, j, k)$, is transformed into another data cube, $\alpha(m_1, m_2, n)$. The location along the n-axis represents color identification for a spectral vector and the value of $\alpha(m_1, m_2, n)$ represents the brightness. Figure 3.2[†] provides an example for a spectral database, W. W is represented as $W = \{s_n\}_{n=1}^{T}$, where T corresponds to the total number of spectral vectors in W. Each spectral vector, s_n, represents a column vector in $\Re^L$. The goal for inversion is not to reconstruct the f data cube but rather the hope is to reconstruct a more accurate data cube, α^* (see Eq. (3.26)). The data cube estimate, α^*, should tend to be more accurate since it is a sparser data cube. More accurate estimation is facilitated when fewer nonzero values can be used to represent an object data cube. CS theory indicates that the

[†]C. F. Cull, K. Choi, D. Brady, and T. Oliver, "Identification of fluorescent beads using a coded aperture snapshot spectral imager," Appl. Opt. **49**, (2010)

object sparsity in a chosen basis is a crucial factor for reconstruction accuracy [6, 7]. In other words, a sparser representation of the object can provide a more accurate estimate when the total number of measurements is fixed. Note that the transformation of the f data cube into the α data cube generally reduces the sparsity in f on the TV basis. The transformation of f is algebraically expressed as

$$f = W\alpha, \tag{3.23}$$

where W represents a block diagonal matrix of spectral column vectors (see Fig. 3.2(b)) and α represents a sparse data cube. Note that once α is estimated, f is retrieved via matrix multiplication.

Then, the 2D TV-minimization algorithm in Eq. (3.21) was modified by incorporating the transformation of f into forward and transpose models. In this section, CASSI's new forward model is described as

$$g = HW\alpha, \tag{3.24}$$

where the system's transformation matrix (H) is characterized by a summation operator (V) and a calibration cube (C). V is a matrix operation representing the *smashing* operation at the detector and C is a matrix describing a 2D aperture code

shifted as a function of spectral channel (k). Actual implementation of the forward model consisted of replicating each normalized spectral vector within the set $\{s_n\}$ at locations spanning the spatial extent of the detector measurement (g) thereby creating a cube for each spectral vector, $s_n(i, j, k)$. Recall that the length of k corresponds to the length of s_n (L). An inner product was taken between each spectral vector cube and the corresponding n channel in α. α_n is equivalent to $\alpha(m_1, m_2, k)$ where the 2D slice for the n channel estimate is replicated L times so that an inner product between a spectral vector cube and α_n cube can be computed. Results produced by the inner products were then added. Afterwards, the result is element-wise multiplied by C, and a sum was taken along the k dimension to provide a new estimate for the detector image, g. The transpose model for CASSI is given by

$$(HW)^T = W^T C^T V^T. \tag{3.25}$$

Further, the spectral database (W), detector estimate (g), and calibration cube (C) were used as inputs to the transpose model. A g data cube was created by replicating the measurement matrix by the number of spectral channels (k) that CASSI measures. The g data cube was then multiplied by C. Then, the inner product between each spectral signature cube, $s_n(i, j, k)$, and the mask-modulated g cube was computed to provide a channel estimate (n). Lastly, a sum was taken along the k domain

to generate a quasi-estimate for each channel (n) in α. This new estimate is in the same domain as $\alpha^*(m_1, m_2, n)$. The forward and transpose models are implemented at every iteration in the TV-minimization algorithm as described by

$$\alpha^* = \arg\min_{\alpha} \parallel g - HW\alpha \parallel_2^2 + \tau\Phi_{TV}(\alpha), \tag{3.26}$$

where the transformation of f is adapted.

The second step involves generating a 2D spectral feature map by creating a maximum value cube, β, from the algorithm estimate, α^*. Recall that, α^* corresponds to a sparse data cube representation of f via a spectral basis decomposition (W) which is calculated via an inner product between each spectral signature, s_n, with the measured data, g. A single value is obtained from each inner product at each pixel location. This value corresponds to the similarity between each spectral signature with the measured data. While physically the (m_1, m_2) pixel location should only correspond to a single n value, the algorithm estimate (α^*) may yield residual values in neighboring channels. For significantly broad and overlapping spectral vectors in W, the residual values near channel n may be large. Once an α^* estimate is produced, maximum values along the n axis at each (m_1, m_2) location are generated.

A maximum value cube, β, was created using

$$\beta(m_1, m_2, n) = \max_n \alpha^*(m_1, m_2, n). \tag{3.27}$$

In β only one nonzero value is found along the n-axis for every (m_1, m_2) location. Recall that each position along n corresponds to a color identification for a spectral vector and each β value represents the brightness associated with each (m_1, m_2) location. Two different spectral feature maps, γ^* can be created from β.

The last step involves producing two different spectral feature maps, γ_1^* and γ_2^*, for data display purposes. The objective was to create a 2D color-coded map that identifies each bead type for an end-user. Thus, a brightness and color preserving feature map (γ_1^*) and a color-only feature map (γ_2^*) were created. The hue, saturation, and value (HSV) model was used for the brightness preserving feature map (see Fig. 3.10(b)). The maximum brightness value β is the input for value and the position along n corresponds to the input for hue in the HSV model. The saturation input for each (m_1, m_2) position was set to one. An HSV model was generated for each n slice in β. Each HSV map was converted into an RGB equivalent where brightness and color information was preserved. Thus, $\beta(m_1, m_2, n)$ was mapped to $\gamma_1(m_1, m_2, n)$ using an HSV map and an HSV to RGB mapping. Note that three values are associated with each (m_1, m_2) location for the n^{th} channel RGB map. To create a 2D spectral

feature map, γ_1^*, a summation is taken over each RGB map created for each n channel using

$$\gamma_1^*(m_1, m_2) = \sum_n \gamma_1(m_1, m_2, n) \tag{3.28}$$

A second spectral feature map (γ_2^*) based on color was also created. Values in β, along each n channel, were normalized and multiplied by the n value assigned to a single spectral vector. $\beta(m_1, m_2, n)$ was transformed into $\gamma_2(m_1, m_2, n)$, where each nonzero value in γ_2 corresponded solely to color.

$$\gamma_2(m_1, m_2, n) = n \left[\frac{\beta(m_1, m_2, n)}{\max_n \beta(m_1, m_2, n)} \right] \tag{3.29}$$

A pseudo-color map was created by assigning n vectors in a linear gray-scale colormap to unique RGB values ((see Fig. 3.10(c)). The 2D spectral feature map, γ_2^*, was created by performing a summation along the n axis in γ_2 using

$$\gamma_2^*(m_1, m_2) = \sum_n \gamma_2(m_1, m_2, n). \tag{3.30}$$

By doing this, the intensity across a single bead is assigned a constant value and any intensity variation across the bead is not preserved. Lastly, a 2D image was displayed by using the prescribed colormap.

In summary, this section described a three-step approach to create two, 2D spec-

tral feature maps (γ_1^* and γ_2^*) of a fluorescence scene. The first step involved a modification to a 2D TV-minimization algorithm by incorporating spectral priors into the inversion scheme. As a result, $f(i, j, k)$ was transformed into a sparser data cube, $\alpha(m_1, m_2, n)$. Second, a maximum value cube was created from the algorithm estimate. The last step in the procedure involved creating two, 2D spectral feature maps from the maximum value cube. Simulations based on the proposed algorithm are discussed in the next section.

3.3.3 Simulation Results

Two TwIST 2D TV-minimization algorithms for 3D data cube estimation and sparse data cube estimation using spectral priors were tested on simulated data to understand the behavior of the algorithm. A simulated 3D f data cube and α data cube were generated by creating a 64×64 pixel scene of four squares containing spectra from the database in Fig. 3.3(b)[†]. The spectral signatures were downsampled spectra corresponding to calibration standards used in fluorescence microscopy. Simulated detector measurements were produced using the aforementioned forward models. The calibration cube was generated by simulating a shifted 64×64 pixel aperture-code. A spectral shift of 10 nm corresponded to a single pixel shift of the aperture-code.

[†]C. F. Cull, K. Choi, D. Brady, and T. Oliver, "Identification of fluorescent beads using a coded aperture snapshot spectral imager," Appl. Opt. **49**, (2010)

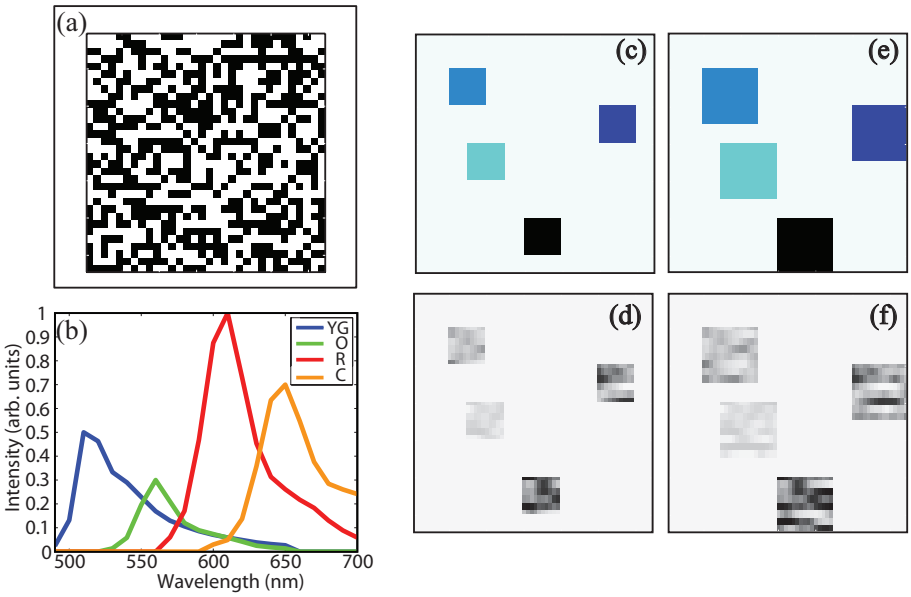

Figure 3.3: (a) Simulated 64 x 64 pixel aperture code. (b) Downsampled fluorescence spectra of a 0.3 intensity-valued yellow green (YG/n=1), 0.5 intensity-valued orange (O/n=2), 1.0 intensity-valued red (R/n=3) and 0.7 intensity-valued crimson (C/n=4) beads. (c) Simulated 10×10 pixel fluorescent squares in a 64×64 pixel image with the corresponding (d) simulated detector image. (e) Input image for 15×15 pixel spectrally different fluorescent squares in a 64×64 pixel image with the corresponding (f) simulated detector image. Note that the colors in (c,e) represent the different intensity values of the simulated fluorescent squares.[†]

A cropped 64×64 pixel replica of the CASSI aperture-code was used in simulation. Also, the simulated system model measured 22 spectral channels spanning the spectral range between 490 nm and 700 nm with 10 nm spectral resolution. The reconstructed f^* estimate and α^* estimate were evaluated using mean squared error (MSE).

In simulation, estimation efficacy for two different square sizes was analyzed. Noise was not added to CASSI measurements for this analysis. A comparison between 10×10 and 15×15 pixel squares was made to quantify how bead size might impact reconstruction accuracy for both algorithms. Regularization parameters (τ) were chosen by trial and error to yield a minimum reconstruction MSE . Number of iterations (p) was chosen such that the relative difference in the objective function was nominal. First, the simulated 3D f data cube was compared to the estimated f^* data cube using MSE. The calculated MSE for the 10×10 pixel squares (see Fig. 3.4(a-b)) is 0.2705 and for the 15×15 pixel squares (see Fig. 3.4(c-d)) is 0.1392. Second, the simulated 3D α data cube was compared to the estimated 3D α^* data cube using MSE. The calculated MSE for the 10×10 pixel squares is 0.1167 and for the 15×15 pixel squares is 0.0415. Note that a smaller MSE was obtained for the estimation of larger squares embedded in a 64×64 pixel scene as depicted in Fig. 3.5. Also, it is important to note that improved reconstruction is possible with α^* data cube

estimation compared to f^* data cube estimation. The analysis of square size provides the motivation to test large beads in the fluorescent microsphere experiment detailed in Section 3.5.

Reconstruction accuracy measured using MSE is a function of object sparsity in the chosen basis (i.e. TV in this study). In simulation, it is possible to analyze estimates by measuring object sparsity in the TV basis. The number of *nonzero gradients*, or level of object sparsity, in the TV basis was calculated for two different square size objects. A nonzero gradient at the $(i,j)^{\text{th}}$ pixel in the k^{th} spectral slice, $\mid \nabla f_{i,j,k} \mid$, is defined as

$$\mid \nabla f_{i,j,k} \mid = \sqrt{(f_{i+1,j,k} - f_{i,j,k})^2 + (f_{i,j+1,k} - f_{i,j,k})^2}. \tag{3.31}$$

Note that larger squares produce more nonzero detector measurements ($g_{m,n} > 0$) and more nonzero gradients. TV object sparsity is measured for both data cube types: the f data cube and the α data cube. The f data cube containing 10×10 pixel squares shown in Fig. 3.4(a) produced 6738 nonzero gradients in the TV basis and 396 nonzero values for the detector measurements. Further, the f data cube containing 15×15 pixel squares (see Fig. 3.4(c)) produced 14280 nonzero gradients in the TV basis and 896 nonzero detector measurements. Second, the α data cube object sparsity was calculated from simulated measurements. The α data cube containing

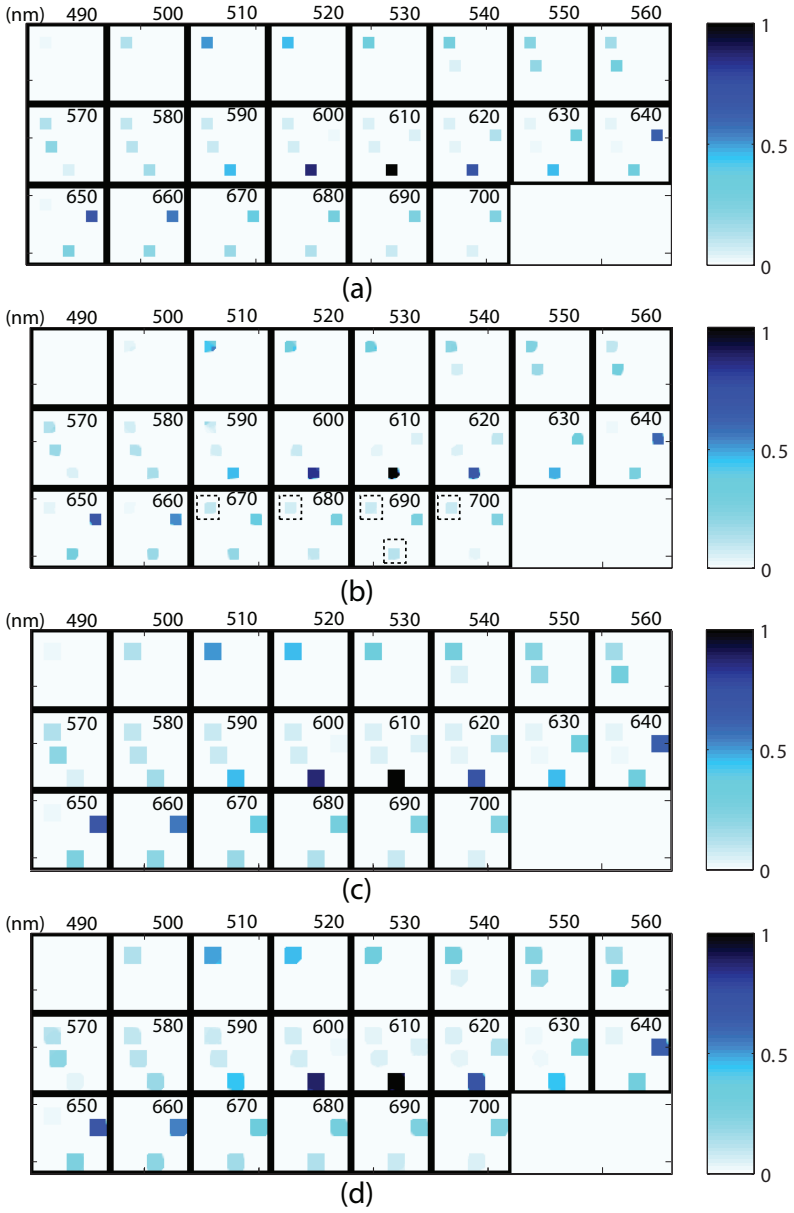

Figure 3.4: Simulated f and f^* data cubes where each sub-image represents a transverse image as a function of spectral slice, k. (a) "true" $f(i,j,k)$ data cube as a function of k for 10×10 pixel squares, (b) estimated $f^*(i,j,k)$ data cube as a function of k for 10×10 pixel squares, (c) "true" $f(i,j,k)$ data cube as a function of k for 15×15 pixel squares, and (d) estimated $f^*(i,j,k)$ data cube as a function of k for 15×15 pixel squares.

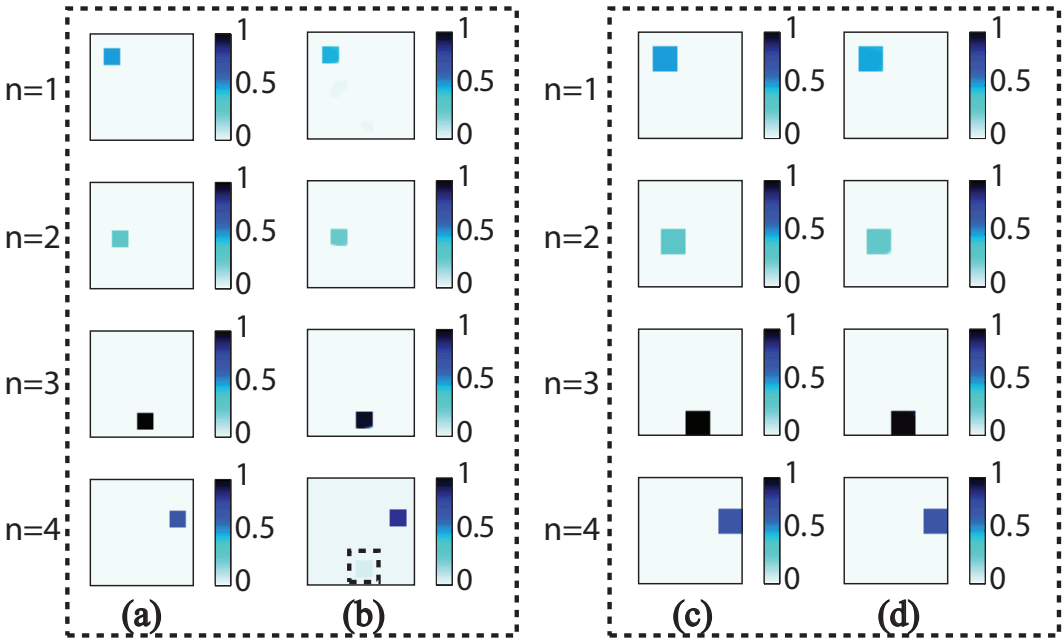

Figure 3.5: Simulated α and reconstructed α^* data cube where each n-channel relates to a single spectral vector in W. (YG, n=1; O; n=2; R, n=3; C,n = 4)(a) "true" $\alpha(m_1, m_2)$ as a function of n for 10×10 pixel squares (b) estimated $\alpha^*(m_1, m_2)$ as a function of n for 10×10 pixel squares. The dotted line in the $n = 4$ slice represents a residual artifact from the $n = 3$ slice. (c)"true" $\alpha(m_1, m_2)$ as a function of n for 15×15 pixel squares (d) estimated $\alpha^*(m_1, m_2)$ as a function of n for 15×15 pixel squares.[†]

10×10 pixel squares, as shown in Fig. 3.3(c), produced 174 nonzero gradients in the TV basis and 396 nonzero values for the detector measurement (g). Also, the α data cube containing 15×15 pixel squares produced 252 nonzero gradients in the TV basis and 896 nonzero detector measurements. A ratio of nonzero detector measurements to object nonzero gradients in the TV basis suggests a measure for reconstruction accuracy. In CS, the number of measurements required for adequate signal estimation is $M \approx O[Klog(N/K)]$, where K represents the sparsity of the signal in some basis and N represents the original size of the signal. Larger squares provide a larger number of measurements and a higher measurement to object gradient ratio, which is an indication for improved CS signal estimation. The f^* data cube compared to the f data cube containing 10×10 pixel squares reveals artifacts at the edges of the smaller pixel squares as noted by the dotted lines in Fig. 3.4(b). Based on the sparsity ratio discussion, f^* data cube estimation requires a larger number of measurements for more accurate reconstruction. Other factors besides the sparsity ratio impact f^* data cube estimation (e.g. mask modulation and system matrix properties). Further, Fig. 3.5(b) shows a reconstruction estimate for 10×10 pixel squares. The dotted line in the α^* ($n = 4$) estimate represents reconstruction error. Contained within the dotted line is a residual square from the $n = 3$ channel estimate. An improvement in reconstruction accuracy for sparse data cube reconstruction occurs when the number

of nonzero detector measurements is increased (see in Fig. 3.5(d)). The ratio of total detector measurements to object sparsity in the TV basis directly impacts TV-minimization reconstructions.

Also, this section compares 3D data cube estimation (f^*) to TV-minimization reconstruction with spectral priors (α^*). First, MSE was calculated between the simulated f data cube (f_T) and the f^* data cube estimate containing 15×15 pixel squares. Next, the TV-minimization estimate (α^*) was transformed into an f^*_α data cube estimate using Eq.(3.23) and the MSE was calculated between f_T and f^*_α. Without noise, the MSE for the f^*_α data cube is 0.1392. This MSE is an order of magnitude better than the MSE obtained with the f^* data cube which is equal to 0.0331.

Further, the impact of noise on TV-minimization reconstruction was analyzed. Poisson noise was added to CASSI measurements. Poisson noise is generated with signal-to-noise ratio (SNR) defined by

$$SNR \stackrel{\text{def}}{=} 10 \log_{10} \left\{ \frac{\sum_m \sum_n g^2_{m,n}}{\sum_m \sum_n (g^p_{m,n} - g_{m,n})^2} \right\}, \tag{3.32}$$

where

$$g^p_{m,n} \sim \frac{1}{\eta} \text{Poisson} \left\{ \eta g_{m,n} \right\}. \tag{3.33}$$

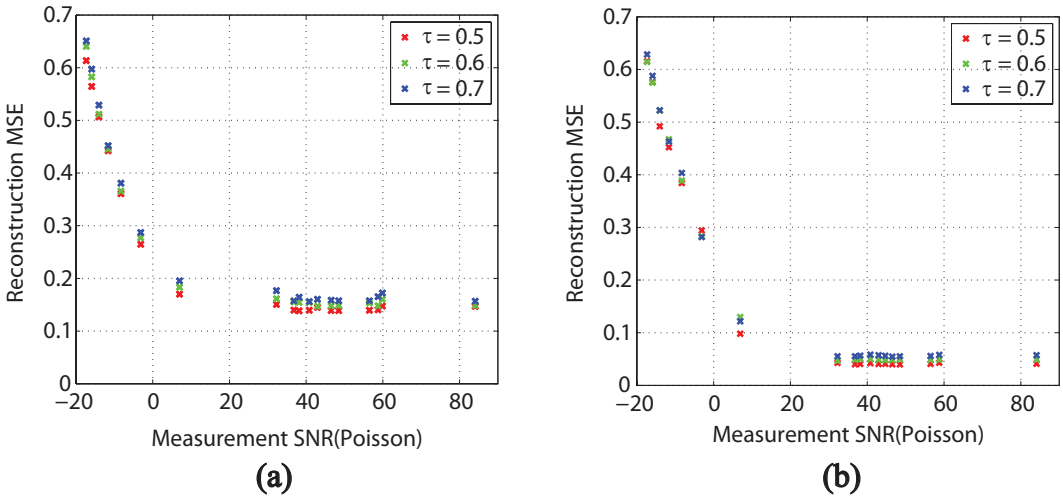

Figure 3.6: Plot of reconstruction MSE from CASSI measurements corrupted by Poisson noise. Reconstruction efficacy is compared between (a) direct f^* data cube estimation and (b) f^*_α data cube estimation (see Section 3.3C for the definition of f^*_α).[†]

The constant value η was chosen based on a desired measurement SNR. Poisson noise was added to CASSI measurements because the experimental system in Section 3.5 is shot-noise limited. The impact of noise on reconstruction efficacy was compared between two different data cube estimation methods (i.e., f^* and f^*_α estimation). In Fig. 3.6[†], 18 different measurement SNR noise levels were analyzed and three different values for τ were considered. Multiple reconstruction MSEs made at each noise level under the same algorithm parameters were found to be consistent. The f^*_α data cube MSE values were still an order of magnitude better then MSE values obtained with f^* reconstructions. Reconstruction MSE converged for both data cube estimation methods around a measurement SNR of 40 dB. Also, the computational

[†]C. F. Cull, K. Choi, D. Brady, and T. Oliver, "Identification of fluorescent beads using a coded aperture snapshot spectral imager," Appl. Opt. **49**, (2010)

cost for estimating f^* was twice as expensive as the estimation of f_α^*. This factor for computational cost varied with image size. These simulation results show that the estimation of α^* produces a more accurate data cube estimate of a simulated f data cube compared to f^* data cube estimation.

In Section 3.3, motivations for the 3D data cube estimation algorithm and the spectral feature identification algorithm were presented. The 3D data reconstruction method provided a procedure for generating a pseudo-color map to present a 3D data cube estimate. Also, an algorithm for direct spectral feature identification was described. Two methods were used to transform the algorithm output into two 2D spectral feature maps. Forward and transpose model implementations were described and used to estimate α^*. Algorithm simulations were used to analyze the performance of two proposed techniques. Simulation results revealed the importance of object size for accurate signal estimation and presented the impact of Poisson noise on reconstruction accuracy. This section did not explore spectral signature limitations (e.g. spectrally narrow or broad). In Section 3.5, reconstructions from real CASSI measurements containing beads with significantly overlapping spectra are presented.

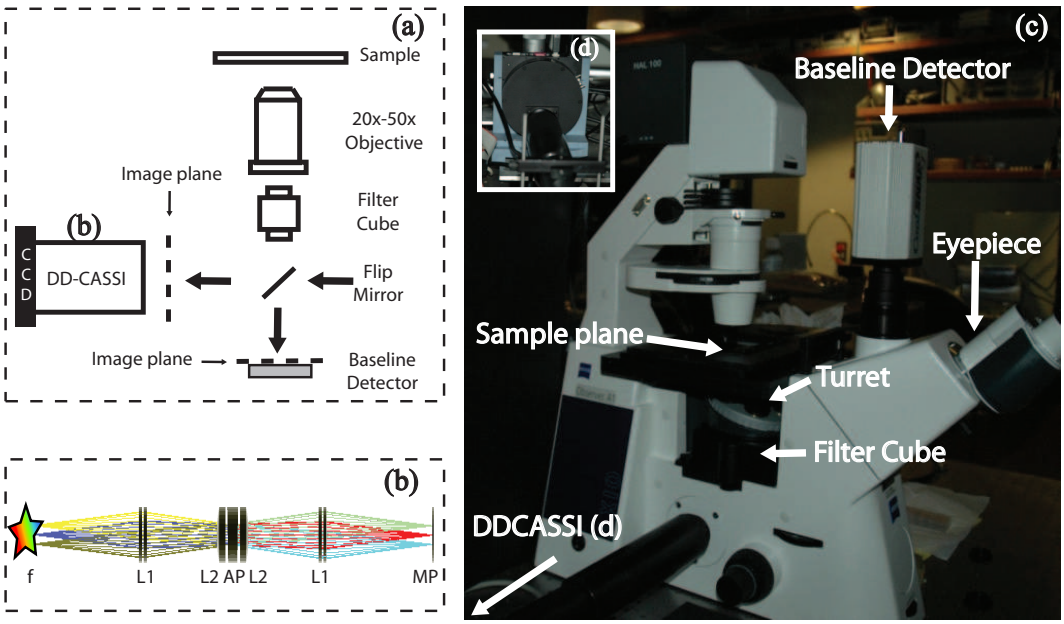

Figure 3.7: (a) Optical architecture for a CASSI interface to an inverted microscope. (b) Realization of Fig. 3.1(a) is in this ray-traced drawing for the first-half of CASSI where (f) is the object (L1) and (L2) are imaging and collimating lenses, (AP) is a direct-view double Amici prism and (MP) is the mask plane where the aperture code resides. (c) Layout of a Zeiss AxioObserver microscope with CASSI coupled to an exit port. (d) Back-end of CASSI.[†]

3.4 System design

A 3.5 ft custom-designed, f/11 CASSI was coupled to the output port of a Zeiss AxioObserver A1 inverted microscope as shown in Fig. 3.7. A Xenon (XBO) arc lamp was used as an excitation source for fluorescence scene analysis. Light from the lamp was directed towards a filter cube located below the objective turret. The filter cube contains an excitation filter, dichroic filter, and an emission filter. The spectral range for the excitation light is between 377 nm and 396 nm and the emission filter spectral bandwidth ranges between 420 nm and 900 nm. Fluorescence signals from

the sample were collected by a microscope objective and redirected towards three intermediate image planes of the microscope. The three intermediate image planes are located at two different exit ports and at the eyepiece. CASSI was coupled to an exit port on the inverted microscope (see Fig. 3.7(c-d)). Two detectors were interfaced with CASSI using a flip mirror. The first detector is a cooled, scientific camera used for imaging samples that require longer exposure times. The detector operates at a resolution of 1200×1600 pixels (16-bit dynamic range) with a pixel pitch of 7.4 μm. A high frame rate camera was used for dynamic scene analysis. It operates at 15 FPS at full resolution (2048×2048) with a pixel pitch of 7.4 μm. The optical architecture and ray-traced model for CASSI is described in Fig. 3.1(a) and Fig. 3.7(b). CASSI uses two direct-view double Amici prisms made from BK7 and SF6 materials. Light from the object is dispersed and imaged onto the aperture-code located at the mask plane (MP) of the optical design. At the mask plane, the dispersion for the spectral range between 450 nm and 750 nm is about 499 μm. A mask element is mapped to two pixels at the detector plane (14.8 μm). With these specifications, CASSI measures about 31 spectral channels within the spectral band of 450 - 750 nm with a spectral resolution of about 10 nm. Recall that the second half of the optical design is a mirror image of the first half (see Fig. 3.7(b)) consisting of a double Amici prism with equal and opposite dispersion. The resolution spot sizes

across the FOV of CASSI vary as a function of spatial position and wavelength. At the edges of the spectral range and at the edges of CASSI's FOV, the average spot size is about 16 μm. Typically, the spatial resolution of coded aperture systems is limited by the mask element size (14.8 μm). Along the edges of the system's FOV and at the two edges of the spectral range, the optical resolution of the system becomes the limiting factor and image quality is degraded. Some of the fluorescent beads analyzed in Section 3.5 were affected by the limitations of CASSI's optical resolution.

3.5 Experimental results

3.5.1 Image quality analysis with (DD)CASSI

Since the f/11 (DD)CASSI was a custom optical system and not manufactured in the laboratory, this section discusses an image quality test to compare *Zemax* simulations with experimental measurements. A method was adapted for testing system spatial resolution [60, 61].

An optical system response to a sharp discontinuity (e.g. step function or slit edges) is one method for measuring resolution. A double slit (12 μm width) at the microscope sample plane was imaged with a 50×, 0.5 NA microscope objective and CASSI. Note that the CASSI aperture-code at the intermediate image plane (see

Fig. 3.1) was removed for the resolution test. The recorded 2D CASSI measurement without the aperture-code is shown in Fig. 3.8(a). The double slit was illuminated with a 10 nm bandpass filtered Halogen light source. The bandpass filters were each centered every 50 nm within a 450 - 700 nm spectral range. Edge spread functions (ESF) were generated from a 1D cross sections (orange line in Fig. 3.8(a)) along the rows of the double slit image (i.e. single column) as shown in Fig. 3.8(b). The ESF shows the imaging system (objective and CASSI optics) response to a sharp discontinuity. Note that peak edges, $L1$ and $R1$ in Fig. 3.8(b), represent microscope sample plane reflections. These reflections contribute to noise or ringing in the line spread function (LSF) shown in Fig. 3.8(c). Averaging of several detector frames would provide a smoother ESF.

After partitioning the ESF into four different regions ($L1$, $L2$, $R1$, $R2$), a derivative was taken in each region to create the LSFs shown in Fig. 3.8(c). The LSF is an integrated point spread function (PSF) profile. If the imaging system PSF is assumed circularly symmetric, the LSF is a 1D approximation to the system PSF. Therefore, *Zemax* spot sizes can be compared to FWHM gaussian fit LSFs measured at four different spatial locations and at six different wavelengths. Table 3.1 compares *Zemax* simulated spot sizes measured in units of detector pixels (7.4 μm) to experimentally measured spot sizes also measured in units of detector pixels. Note that in Table 3.1,

Table 3.1: Zemax and experimental spot sizes

	Wavelength(nm)	*Zemax*(pixels)	Experimental FWHM (pixels)	Δ
1	450	2.43	9.42	6.99
2	500	1.35	3.52	2.17
3	550	0.50	4.47	3.97
4	600	1.89	4.47	2.58
5	650	2.43	7.77	5.34
6	700	1.89	12.0	10.11

Δ represents the difference between both spot size metrics (e.g. *Zemax* and the measured LSFs) in detector pixel units. Several sources of error in the measured data can be attributed to the spot size mismatch. These sources include: detector noise contributions seen in the ESF, optical system misalignments in the custom optical design, and imperfect ESF results. Further, CASSI measurements from a monochromatic full-field source scanned between 450 nm and 750 nm in 5 nm increments suggested that input sources at the edges of the spectral band (e.g. 450 nm, 700 nm, and 750 nm) resulted in spatially blurred mask features. Table 3.1 verifies experimental observations since the largest difference (Δ) between the simulated spot sizes and experimental spot sizes occur at the edges of CASSI's spectral range.

The modulation transfer function (MTF) was generated by taking the Fourier transform of the LSF. Recall that from Chapter 2 the MTF was defined as the ability to resolve an object size of a particular spatial frequency with high contrast. Fourier domain sampling for the MTF plots is defined in [61]. The Fourier-transformed

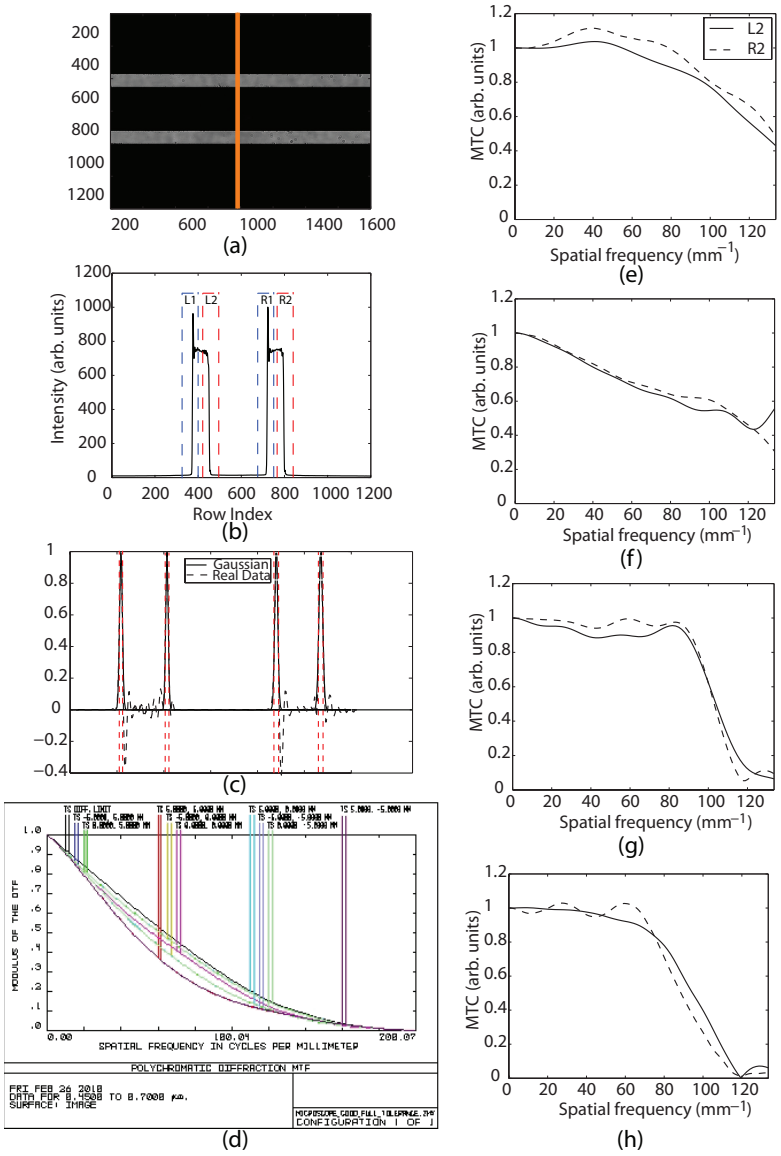

Figure 3.8: (a) Bandpass filtered halogen (500 - 510 nm) illuminated double slit (12 μm) (DD) CASSI image without the aperture-code in the intermediate image plane. (b) Edge spread function (ESF) recorded along (the orange line) a single column and all rows in (a). (c) Line spread function (LSF) generated for regions $L1$, $L2$, $R1$, and $R2$ in (b) with a gaussian curve fit applied to each LSF. (d) *Zemax* modulation transfer (MTF) plot of the custom designed (DD) CASSI system. Experimentally estimated MTFs at (e) 450 nm, (f) 500 nm, (g) 650 nm, and (h) 700 nm.

LSFs located in regions $L2$ and $R2$ in Fig. 3.8(b) at various wavelengths are shown in Fig. 3.8(e-h). The *Zemax* MTF plot can be compared to the MTF plots in Fig. 3.8(e-h). Note that MTC represents the modulation transfer coefficient or contrast value. The MTF plot at 500 nm is most similar to the *Zemax* result. The contrast difference between the *Zemax* MTF plot and the measured MTF plot is .2 at 120 mm^{-1}.

This section provided a method for measuring CASSI's optical performance. The measured performance was compared to *Zemax* simulations. The results explain CASSI's poor spatial resolution at the edges of the spectral band.

3.5.2 Calibration procedure and algorithm implementation

The CASSI model described in Section 3.2 was based on a variety of assumptions. A 1:1 correspondence between the mask element pitch and the detector pixel pitch was assumed. In practice, not all wavelengths spanned by an input power spectral density correspond to single pixel shifts at the detector. Also, a unity magnification impulse response assumed for both arms (h_1 and h_2) in the system model does not account for a spatially varying blur, a change in magnification, or aberrations in the system. A calibration cube for CASSI was taken before a fluorescence scene was analyzed. Ideally, a calibration cube would consist of translating a monochromatically illuminated fiber across the system's FOV at wavelengths spanning the spectral range

of the instrument. However, this calibration process is photon-limited and time consuming. A calibration cube was acquired via full-field monochromatic illumination of CASSI. Full-field illumination was generated using a fiber-coupled optical setup (see Appendix A.4) designed to match the microscope objective image space NA used for fluorescence measurements. Each spectral slice in the calibration cube represents a spectral impulse response recorded every 5 nm for the spectral range between 450 nm and 750 nm. Unlike the monochromatic source analysis explored in Section 3.2, multi-spectral objects measured by CASSI can be described as a superposition of shifted mask patterns that span the object's spectrum. The calibration cube considers the influence of a spectrally shifted aperture-code on a multi-spectral object.

For fluorescent target analysis, the TwIST TV-minimization algorithm was used with the modifications discussed in Section 3.3. Inputs to the algorithm included a CASSI measurement, a calibration cube, a regularization constant, and a spectral database. A region in the image was cropped in order to apply local processing. This is possible because the detector measurements are well registered. Although full FOV processing was possible, local processing provided a lower computational cost. For low contrast signals, a cropped region in an α^* estimate was renormalized to locally increase the contrast of the weak signal. This procedure is similar to applying a local digital gain to an image. By renormalizing the cropped region, all brightness

information from the sparse data cube estimate was removed. These inputs and techniques were used for more accurate data cube estimation and for 2D spectral feature mapping of a ten bead type fluorescence scene.

There are multiple noise contributions that affect CASSI images recorded with a cooled, scientific camera. Two most common noise contributions are photon noise and detector noise. With a well depth of 2^{16}, a readout noise of $(7.9\ e^-)^2$, and a dark current of $(3\ e^-)^2$ the detection system is shot-noise limited. The effect of dark current noise was minimized with additional cooling of the detector to $-20\,^{\circ}\mathrm{C}$. For each data set, a background signal with mean 124 electrons was subtracted to minimize readout noise and dark current noise contributions. Readout noise and dark current noise have nominal effects. Also, longer exposure times were used to maximize SNR. While concerns for the impact of readout noise and dark current are emphasized in fluorescence microscopy of biological samples, in this study, the sample fluorescence emission is photon abundant. Simulations in Section 3.3 describe the impact of Poisson noise on reconstruction efficacy for a shot-noise limited measurement. If a photon-limited case was tested, readout noise would become significant. In this case, TV-minimization reconstructions would be more affected by the aforementioned noise contributions.

3.5.3 Fluorescence microscopy with CASSI

Microscope slides were prepared with Invitrogen Molecular Probes fluosphere solutions. Ten spectrally different fluorescent microsphere solutions were selected. Each fluosphere solution contained 15 μm polystyrene microspheres/beads suspended in 10 mL of 0.15 M NaCl with 0.05% Tween 20 and 0.02% thimerosal. First, the ten different bead solutions were mixed in a separate container. Then, a mixed solution of fluorescent beads was mounted onto a slide using a FluorSave mounting medium from Calbiochem. Each microscope slice containing fluorescent microspheres was analyzed at the "best focus" FOV in the image plane of the microscope objective. The "best focus" FOV is defined as the plane empirically found when a majority of the beads come to focus. Goitrogen's absorption and emission maximum wavelengths are described in Table 3.2. Unlike current multi-spectral systems used in microscopy, CASSI fluorescence bead experiments employ a single, UV excitation source to excite all ten bead types mentioned in Table 3.2. One excitation source removes the need for multiple emission filters or movable parts typically needed in confocal spectral microscopy setups. Since a single excitation scheme was employed, baseline UV excited emission spectra for each microsphere type was recorded using an Ocean Optics (OO) slit spectrometer (see Table 3.2). The recorded OO spectral emissions (see Fig. 3.10(e)) were used as baseline spectra for comparison with 3D data cube

estimates at pixel locations on the microspheres. Also, the OO spectral emissions were inserted into the spectral database (W) for sparse data cube estimation and bead identification. Note that CASSI can be adapted for multi-source narrow-band excitation. A single wide-band UV source merely simplified the implementation for the ten bead type sample under test.

Table 3.2: Fluorescent Microspheres

	Color	ID.	I Abs/Em (nm)	OO Ex/Em (nm)	[OO - I](Em)
1	Blue-green	BG	430/465	390/485	+20
2	Green	G	450/480	390/518	+38
3	Yellow-green	YG	505/515	390/537	+22
4	Yellow	Y	515/534	390/606	+72
5	Orange	O	540/560	390/576	+16
6	Red-orange	RO	565/580	390/640	+60
7	Red	R	580/605	390/620	+15
8	Carmine	CA	580/620	390/635	+15
9	Crimson	C	625/645	390/674	+29
10	Scarlet	S	645/680	390/698	+18

In the experimental setup, CASSI was interfaced to an inverted microscope for fluorescence scene analysis of calibration standards. Two TV-minimization algorithms were applied to CASSI measurements: a 3D data cube estimation algorithm and an algorithm incorporating spectral priors into the TV-minimization scheme. The sample fluorescence emission was relayed to a microscope intermediate image plane using a Zeiss LD Epiplan 50×, 0.5 NA air objective. Recall that a "best focus" FOV was chosen with the microscope objective. In Fig. 3.10(c-d), some beads ap-

pear larger than the rest of the beads contained within a selected FOV. The $Y4$ bead size in Fig. 3.10(a) was caused by an anomaly in the manufacturing process of the Invitrogen fluospheres. However, it is evident from Fig. 3.10(d) that the size of bead $O1$ (see Fig. 3.10(a)) can be attributed to defocus. While a "best focus" FOV was attempted, some beads contained within the selected FOV are located at different depths. This caused beads to appear larger than their true size.

Once a "best focus" FOV was obtained, an intensity-valued spectrally encoded 2D measurement was recorded with CASSI. Figure 3.10(a) shows a CASSI baseline measurement where spectrally coded beads reveal CASSI's optical resolution as a function of wavelength. CASSI measurements (g) were then inverted using the two algorithms discussed in Section 3.3.

First, TV-minimization was used to reconstruct the f^* data cube from the 2D spectrally encoded CASSI measurement. Figure 3.9(k) shows a ten pseudo-color image of a ten bead type fluorescent scene that was generated using the hexadecimal HTML color to RGB value method detailed in Section 3.3.1. Note that the 2D image contained beads additionally outlined with white circles. The 2D image in Fig. 3.9(k) enables bead discrimination, however, intensity variation across the spatial extent of a single bead causes errors in spectral estimation at various pixels. As a result, complete discrimination of red (R), carmine (CA), and red-orange beads is challenging

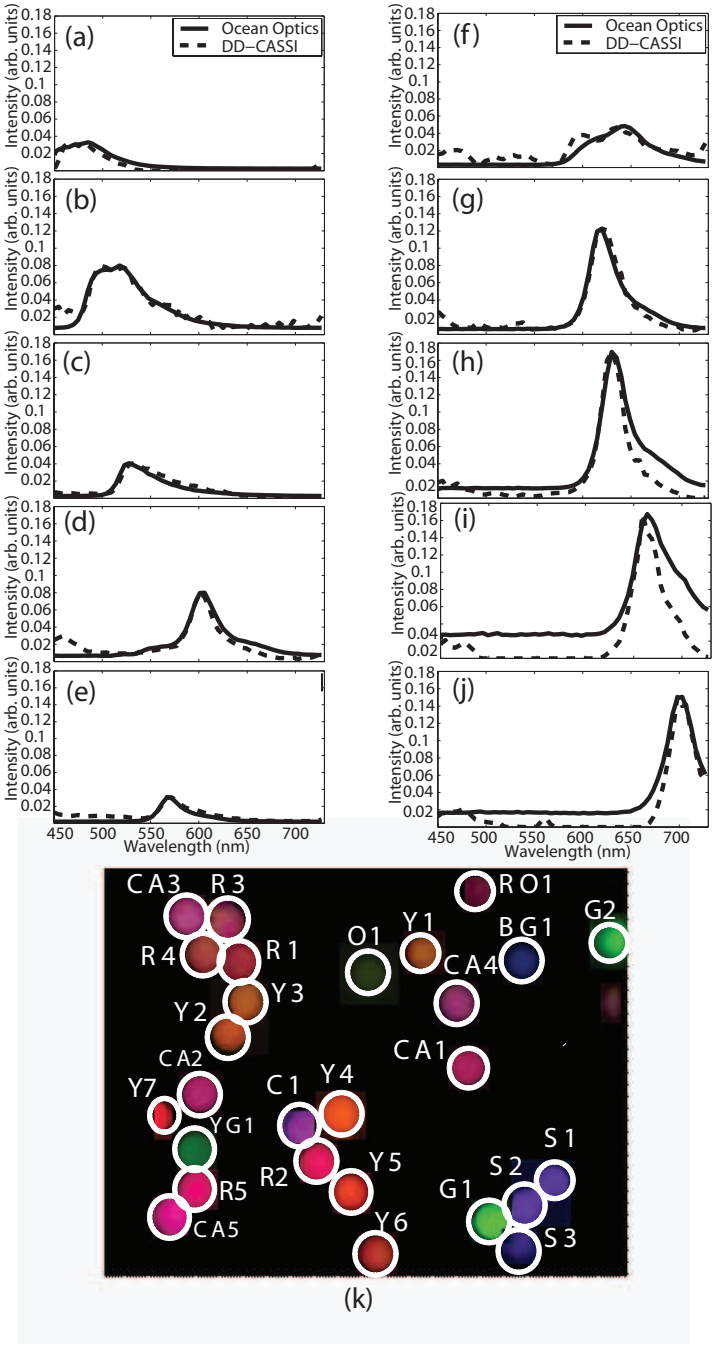

Figure 3.9: f* data cube reconstruction using TV-minimization. Amplitude spectral plots at a single spatial location on the (a) $BG1$ bead, (b) $G1$ bead, (c)$YG1$ bead, (d) $Y1$ bead, (e) $O1$ bead, (f) $RO1$ bead, (g) $R1$ bead, (h) $CA1$ bead, (i) $C1$ bead, and (j) $S1$ bead labeled accordingly in (k). Baseline OO spectra for each bead type are overlayed with CASSI-based reconstructed spectra. (k) Pseudo-colored ten bead CASSI reconstructed image. White circles are additionally added to the image to outline the bead locations.[†]

in Fig. 3.9(k). Further, amplitude spectral plots from a single spatial location on each bead type are shown in Fig. 3.9(a-j). Recall that baseline amplitude spectral plots were obtained with an OO slit spectrometer. Reconstructed spectral plots were compared to rescaled OO baseline spectral plots. Figures. 3.9(a-j) show that reconstructed spectral plots resemble the baseline spectra. However, it is important to note that at different spatial locations on each bead (e.g. at the edges), the shape of the spectral estimate changes. This was the main shortcoming with the 3D data cube estimation method.

Second, the direct spectral feature identification algorithm was applied to CASSI measurements. The reconstructed α^* data cube was transformed into a 2D spectral feature map of the scene. Figure 3.10(b) shows a 2D spectral feature map of a ten bead type fluorescence scene generated from an HSV to RGB mapping, γ_1^*. Beads in this 2D spectral feature map were additionally outlined with white circles. Closer inspection of the reconstructed beads in the 2D bead identification map reveal artifacts in the bead shape. The artifacts or non-uniformity is caused by local processing of the beads for α^* data cube processing. Also, Fig. 3.10(c) represents a color-based 2D spectral feature map, γ_2^*. White circles were added to the 2D bead identification map. Bead reconstruction artifacts from the α^* data cube are clearly seen in the color-based 2D map. Again, the TV-minimization reconstruction parameter τ was

chosen by trial and error. The number of iterations was chosen such that the relative difference in the objective function was nominal. Various values of τ ($\tau = .5 - 2$) were used to evaluate each bead region. Crimson and scarlet were are weakly excited by UV excitation. Signal intensity from these beads appear dim in the baseline CASSI measurements since well-excited beads provide a higher contrast when compared to the background detector signal. Still, the color-based 2D spectral feature map enabled identification of weakly excited beads despite a loss in intensity within the bead region from renormalization of the bead FOV in post-detection.

CASSI measurements and post-detection algorithms provided 2D spectral feature maps where beads are identified based on intensity values and color. In the next discussion, a filtered-array imaging system is described. A baseline image from the filtered-array imaging system is used to verify spectral feature maps generated from CASSI measurements.

3.5.4 Verification testbed

A baseline image was recorded with a Nikon A1 confocal microscope to verify CASSI 2D bead identification maps. The baseline image was separately recorded and was not associated with the CASSI architecture. Results obtained from the baseline system were not compared with CASSI reconstructions as it is not fair to do so

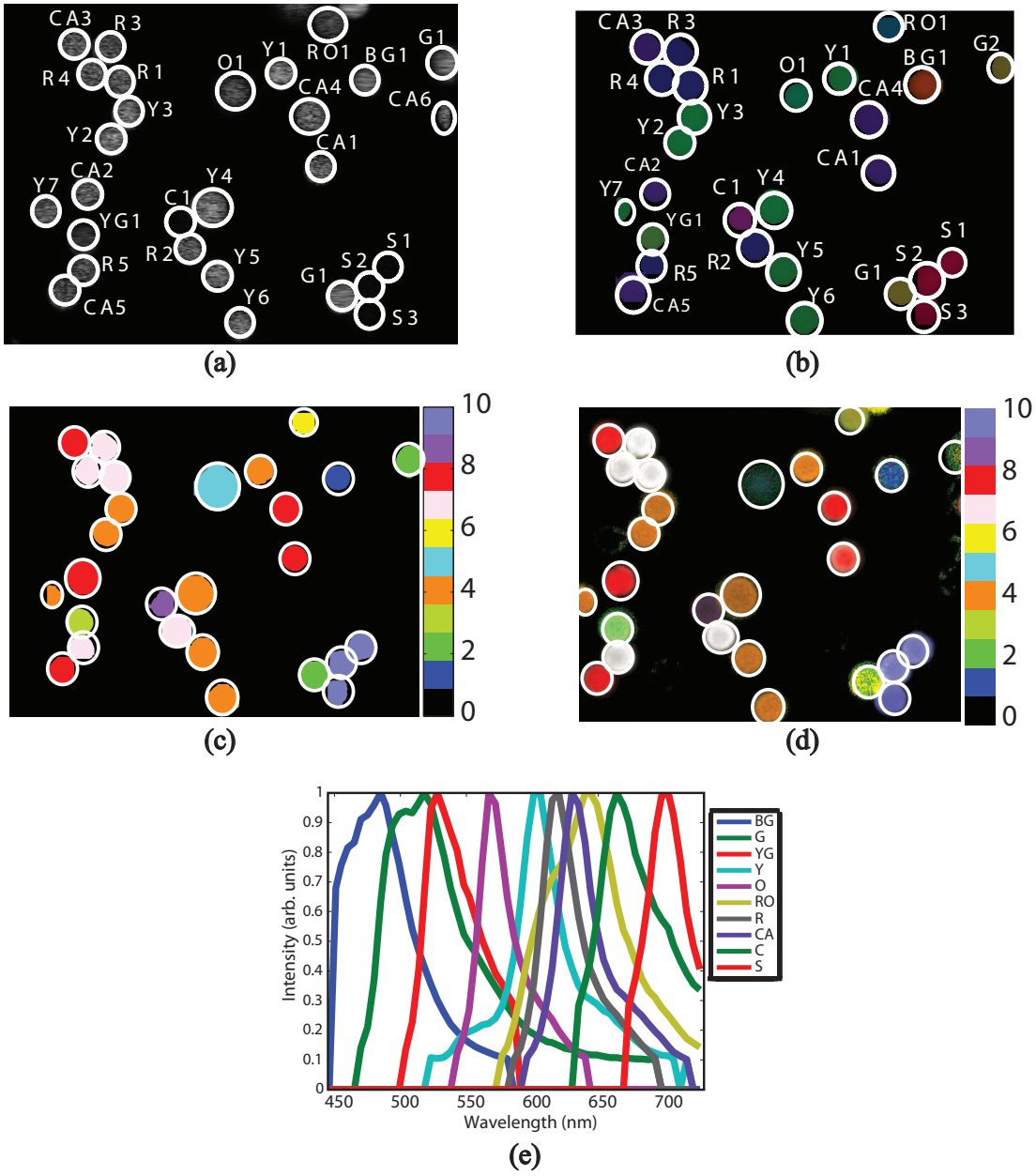

Figure 3.10: (a) Baseline CASSI 2D intensity-valued measurement of a ten bead type fluorescent scene acquired with a 50×, 0.4 NA microscope objective. White circles are added to the images to outline the locations of the beads. (b) CASSI reconstructed 2D spectral feature map, γ_1^*. (c) CASSI 2D spectral feature map, γ_2^*. (d) Nikon A1 series baseline image with ten bead type discrimination where the beads are additionally outlined in white. (e) Spectral vectors used in the database, W, for CASSI reconstructions.[†]

given different system architectures, variable incident energy at the detector, and different excitation schemes. The baseline image is shown merely to illustrate ten bead type discrimination with 2D color coded images produced by a filtered-array system.

A baseline image was captured with a Nikon A1 confocal microscope in wide-field fluorescence mode. A wide-field fluorescence mode was undertaken since CASSI measurements were recorded in wide-field and the goal did not involve imaging diffraction limited spots where out-of-focus light could hinder image analysis. The baseline image was recorded using a CFI Plan-Apochromat 10x, 0.45 NA microscope objective. A multi-wavelength illumination scheme was used for ten bead type excitation. A 402 nm diode laser at 4.8 mW was used to excite both the blue-green and green beads. Yellow-green and yellow beads were illuminated with a 488 nm argon line at 8.6 mW. Orange, red-orange, and red beads were illuminated with a 561 nm laser line at 5.1 mW. The carmine, crimson, and scarlet beads were excited with 640 nm light at 4.1 mW. The Nikon A1 series is also a grating-based system where dispersed light is focused onto a 32-channel PMT array detector so that each channel detects a 10 nm bandwidth. Since a lamdba stack could not be generated at the time of image acquisition, spectra were estimated for various regions of interest and ten spectral emission windows were created in order to isolate each spectrally unique bead type.

The baseline image was recorded with a resolution of 512×512 pixels with approximately 24.8 μm square pitch and yielding a 12-bit dynamic range. For the baseline image, colors were manually assigned to each spectrally unique bead type. The bead type colors within Fig. 3.10(d) were assigned to match the color assignment of the CASSI-based bead identification map in Fig. 3.10(c). The Nikon A1 series baseline image provided a means for verifying the ten bead type spectral map generated from CASSI measurements.

In Section 3.5, a CASSI-microscope interface was described for fluorescence microscopy. In particular, a ten bead type fluorescence scene was analyzed with two TV-minimization schemes and a three-step procedure provided a direct method for bead type identification. The Nikon A1 series provided an image that verified CASSI reconstructed spectral maps.

3.6 Dynamic imaging with CASSI

Dynamic scene analysis was also realized with CASSI. A solution containing ten bead types were pipetted onto a microscope slide and a coverslip was placed on top of the solution. A high frame rate camera, previously described in Section 3.4, was interfaced to CASSI using a flip mirror at the back-end of CASSI. The AVT Pike F-421 camera contains the KAI-4022 Kodak sensor measuring 2048×2048 pixels with

14-bit dynamic range and a 7.4 μm pixel pitch. CASSI images were recorded at 7.5 FPS with a 600×800 pixel image resolution. A baseline detector was placed at a second exit port to the AxioObserver microscope. Baseline images were recorded with an *Imaging Source* DFK 41BF02 firewire color camera containing a ICX205AK Sony sensor measuring 1280×960 pixels with 8-bit dynamic range and a 4.65 μm pixel pitch. Approximately 385 frames of data were recorded with CASSI and the baseline camera at 7.5 FPS and compared. Both algorithms discussed in Section 3.3 were used to reconstruct two different data cubes: one to generate color-coded frames for video production based on spectral reconstruction and the other for direct bead identification using a priori spectral data. As in Section 3.5, local processing of the frames facilitated quicker processing of the collected data.

3.7 Compact CASSI-II design

CASSI was successfully applied to fluorescence microscopy, but one drawback was CASSI's one meter optical system track length. To improve upon this, a new design was created in *Zemax*.

The goal of the redesign was to construct an off-the-shelf, low-cost, and compact system that could interface to any laboratory grade microscope. The redesign, CASSI-II, utilized two low f/number relay lenses from *Edmund Optics*, a field lens,

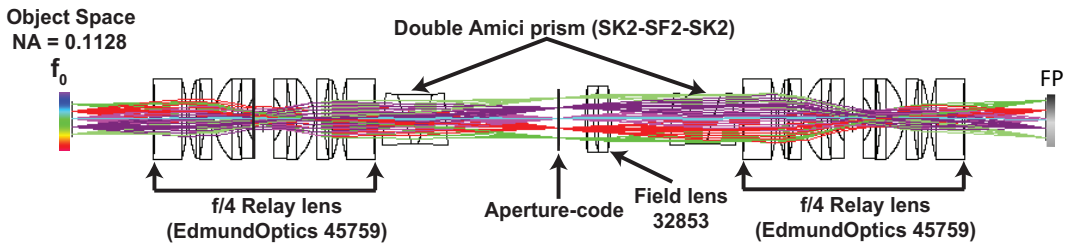

Figure 3.11: *Zemax* 3D optical architecture of CASSI-II where f_0 represents the source spectral density and *FP* represents the monochromatic detector plane..

and custom Amici prisms for the DD optical architecture. For *Zemax* simulations, the relay lens prescription data was obtained from *Edmund Optics*. Also, the Amici prisms were remnants from a previous custom optic order that consisted of two types of flint glass SK2 and SF2 [36]. After several iterations of *Zemax* optimizations with various relay lenses, an improved design was achieved.

The improved design for a low f/number and compact (<3.5 ft) CASSI-II system is shown in Fig. 3.11. For the design, the system object space NA was set to the resultant image space NA from a high NA microscope objective and a coupling optic. Two different microscope objectives were incorporated into the system design: a *Zeiss* Plan-Apochromat 40×, 1.4 NA oil objective and a Plan-Apochromat 20×, 0.8 NA air objective. A *Nikon* CCTV 0.35× coupling optic was also incorporated into the image space NA metric. The aforementioned objectives and coupling optic combination provided an image space NA of approximately 0.114. The microscope

objective image space NA (NA_I) is calculated using

$$\mathrm{NA}_I = \frac{\mathrm{NA}}{M * C} \ , \tag{3.34}$$

where M represents the microscope objective magnification and C represents the coupling optic magnification. The object space NA of CASSI-II was set to match the resultant microscope and coupling optic image space NA. Further, two (*Edmund Optics* NT45-759) f/4, 30 mm relay lenses were used in the optical architecture. Also, the field lens in Fig. 3.11 is a double achromat lens (*Edmund Optics* 32853) with a 45 mm effective focal length. The field lens minimized chromatic aberration. Also, the lens helped to redirect the cone of light coming from the edge of the field, thereby reducing vignetting at the second Amici prism surface.

The system optimization procedure involved measuring the dispersion at the intermediate image plane (mask plane), minimizing spot size at the mask and image plane, determining optimal system field positions, and determining the spectral sensitivity of the instrument. The dispersion (Δd) at the intermediate image plane (see Fig. 3.11) for the spectral range ($\Delta\lambda$) between 470 nm and 770 nm measured 348.8 μm. The number of spectral channels detected by the optical system was determined by dividing the dispersion spatial extent at the mask plane by the RMS spot size at the mask plane (e.g. Typically, the feature size is the RMS limiting factor for

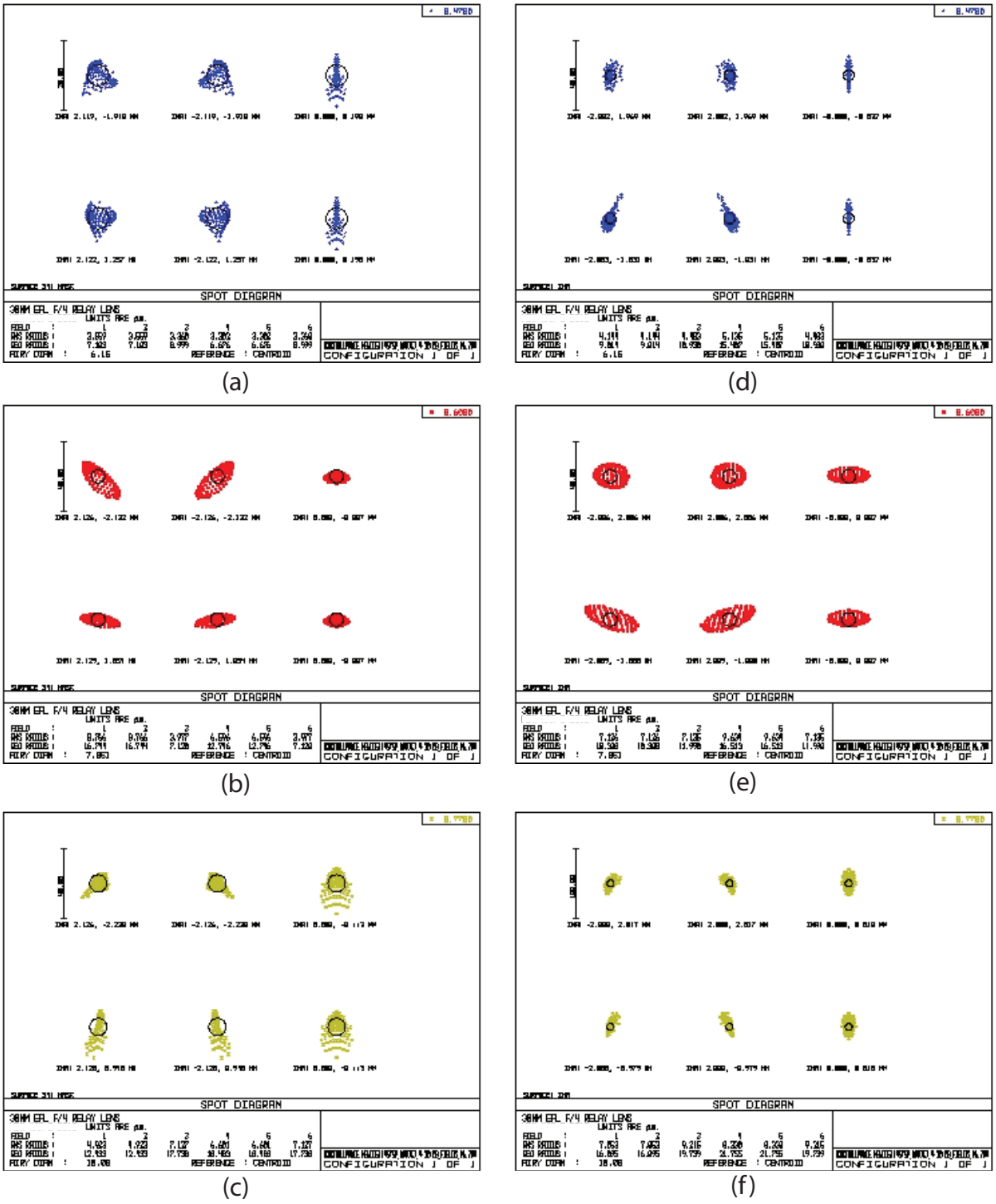

Figure 3.12: *Zemax* CASSI-II spot diagrams at the mask plane for wavelengths (a) 470 nm, (b) 600 nm, (c) and 770 nm. Image plane CASSI-II spot diagrams at wavelengths (d) 470 nm, (e) 600 nm, and (f) 770 nm.

spot size). Figure 3.12(a-c) shows spots sizes at the mask plane as a function of field position and wavelength. Given the spot size at the mask plane, the minimum mask feature size (Δf) for CASSI-II to prevent aliasing measured 14.8 μm. Considering this feature size, CASSI-II measures approximately 24 spectral channels with 14 nm spectral resolution. Spectral resolution ($\Delta\Lambda$) with DD snapshot spectral imagers is calculated using

$$\Delta\Lambda = \frac{\Delta f \Delta\lambda}{\Delta d}. \tag{3.35}$$

A smaller mask feature size or spot size at the mask plane would improve the number of spectral channels measured by the snapshot spectral imaging system. The spectrally varying spot sizes at the CASSI-II image plane are shown at various field positions in Fig. 3.12(d-f). This figure also shows field positions spanning about a 4 mm spatial extent. Coma aberrations are apparent in the spot diagrams at the image plane. These spot sizes and aberrations help characterize CASSI-II image quality. Overall, CASSI-II enabled a more compact solution for fluorescence microscopy at a lower cost due to the use of off-the-shelf optics.

This section has discussed a *Zemax* simulated redesign of CASSI that provided several advantages. The CASSI-II optical system was spectrally sensitive over a spectral range of 470 - 770 nm with 14 nm spectral resolution. Also, CASSI-II measured a 5.3 f/number, an improvement over the previous f/11 generation. Also,

the simulated instrument is three times smaller than the previous generation system with a total track measuring 6.78 in. More optimization or a custom design would improve spatial resolution at both the mask and image planes, thereby improving CASSI-II spectral sensitivity and image quality. While simulations of a second generation system were presented in this section, the system was not built. The next step would be realizing the system redesign.

3.8 Summary

In this chapter, a CASSI optical architecture and interface to an upright microscope for fluorescence microscopy was described. Two numerical estimation methods were used to reconstruct a 3D data cube from 2D detector measurements. Both methods utilized a nonlinear iterative decoding process called TwIST that exploited compressive sensing ideas for 3D data cube estimation. In particular, sparsity in the TV basis was exploited for accurate estimation. While the first method solely exploited sparsity in the TV basis, the second introduced an adaptation to the TV-minimization algorithm with the addition of spectral priors to the inversion scheme. The adaptation naturally produced a sparse data cube estimate of a fluorescent scene instead of reconstructing a f^* data cube estimate where spectra are estimated at every spatial location. With a sparse data cube estimate, a three-step procedure was

implemented to produce two spectral identification maps. These spectral identification maps can assist users in localizing fluorescent beads in a 2D scene. Lastly, a multi-spectral imaging system (a Nikon A1 confocal microscope) was used to verify the CASSI based bead identification maps. The Nikon A1 microscope provided a ten bead type spectral identification map which enabled the verification of CASSI spectral maps. While the first TV-minimization method produced a spectrum at every pixel location, the second method provided a direct means for identifying fluorescent beads from CASSI measurements. Finally, this chapter discussed dynamic imaging of fluorescent microspheres with CASSI and provided a *Zemax* design for a second generation compact and robust snapshot spectral imager.

(DD) CASSI is suitable for fluorescence microscopy applications. Fluorescent beads analyzed in this paper were photon-abundant. Longer exposure times enabled a maximum system SNR. Effects with detector readout noise, background noise, and dark current noise, more common in low-light fluorescence microscopy, would impact TV-minimization reconstruction. These effects were not explored in this chapter since the system operated in the shot-noise limit. Also, while CS inversion schemes incur a higher computational cost, these costs can be reduced. Since (DD) CASSI spectrally encoded measurements are well-registered at the detector plane, local processing can be applied to the measured data. The post-detection process for bead identification

was parallelizable, therefore computational times were reduced. Lastly, this chapter showed that sparse synthetic data cube estimation instead of 3D spectral data cube estimation could potentially reduce an intrinsic computational cost.

Chapter 4

Millimeter-wave compressive holography

While previous chapters focused on spectral imaging, this chapter describes an active millimeter-wave (MMW) holographic imaging system that uses compressive measurements for 3D tomographic object estimation. The system records a 2D digitized Gabor hologram by translating a single pixel incoherent receiver. Two approaches for compressive measurement are undertaken: nonlinear inversion of a 2D Gabor hologram for 3D object estimation and nonlinear inversion of a randomly subsampled Gabor hologram for 3D object estimation. The object estimation algorithm minimizes a convex quadratic problem using total variation (TV) regularization for 3D object estimation. This chapter discusses the comparison between object reconstructions using linear backpropagation and TV-minimization. Also, simulated and experimental reconstructions from both compressive measurement strategies are presented. In contrast with backpropagation, which estimates the 3D electromagnetic field, TV-minimization estimates the 3D object that produces the field. Despite undersampling, range resolution is consistent with the extent of the 3D bandwidth.

4.1 Introduction

Various methods exist for concealed weapons detection [62]. These methods aim to penetrate common obstructions such as clothing or plastics. X-ray [63] and millimeter-wave (MMW) [64] imaging systems are technologies capable of penetrating these barriers for imaging suicide bomb vests or weapons composed of metals, non-metals, or plastics. While X-ray imaging capabilities are highly effective, questions about health risks impair the feasibility of such systems for real-time imaging. Millimeter waves for low power (on the order of milliwatts) imaging systems do not present a health hazard and therefore enable real-time imaging of targets with high contrast and high resolution.

Several studies have explored both active and passive MMW imagers for concealed weapons detection [65, 66] where the system limitation is the detector array cost. Some systems include portal, or hand-held devices [67] operating in close range to the target. Other systems are holographic [68,69]. These MMW focal and interferometric systems map object information onto a two-dimensional (2D) or a linear array that is typically scanned for image formation. These scanning systems [70–72] are plagued by their associated data acquisition times. For these systems there is a tradeoff between scan time and measurement SNR. Therefore, rapid scanning of concealed weapons is challenging for current MMW systems.

For stand-off explosive detection; rapid scanning of the target is a necessity. To overcome the bottleneck associated with current MMW scanning systems, a compressive sensing (CS) framework is considered. Recent studies in CS reveal that an N-point image can be restored from M measurements where $M << N$ [66, 73–75]. Mittleman et al. [74] used a focal system to randomly sample spatial frequencies in the Fourier plane for 2D object estimation at 100 GHz. Work in 633 nm compressive holography [21] further motivates the investigation of CS for MMW imaging. Digital holography, which measures a limited set of spatial frequencies in the Fourier domain, is a compressive encoder, since it compresses three-dimensional (3D) spatial information into a single interferometric planar field. Since the entire extent of an object's 3D spatial frequency band volume can not be captured in a single exposure, multi-angle illumination or object rotation is typically used to improve 3D object estimation. However, the results in [21] suggest that 3D tomographic estimation can be achieved from a 2D hologram recording.

This chapter extends compressive holography to millimeter wavelengths. Subject matter in this chapter differs from compressive holography at visible wavelengths since sparse holographic sampling is implemented to minimize the data acquisition scan cost associated with imaging at millimeter wavelengths. Also, the MMW holography system operates in a completely different wavelength region with corresponding

differences in optics and detectors, so it requires a completely new system design compared to work at visible wavelengths. In this chapter, a subset of spatial frequencies are holographically recorded for 3D object estimation. Also, a randomly subsampled 2D hologram is used to analyze the impact of fewer measurements on 3D object estimation. The holographic technique is similar to [69] since the system architecture is not band-limited by a lens aperture and phase information is preserved. The method in this chapter differs in the nonlinear inversion scheme used for 3D object estimation. The method optimizes a convex quadratic problem using total variation (TV) regularization. The results in this chapter demonstrate that undiffracted fields, overlaid in the frequency domain of a Gabor hologram, can be separated by exploiting TV object sparsity.

Although other contributions in the literature embody a mathematical framework similar to compressive holography [16, 17, 76], there exists a fundamental difference in philosophy. Compressive holography exploits encoding and undersampling for 3D object estimation, whereas techniques in diffraction tomography are designed to overcome sampling limitations imposed by the data collection process. Also, recent work by Denis et al. [77] presents a similar twin-image suppression method; however, a sparsity-enforcing prior in a Bayesian framework combined with l1-regularization is used for object estimation. This chapter represents the confluence of MMW digitized

holographic measurement and TV-minimization for 3D object estimation with minimal error. The algorithm framework in [21] is further adapted for sparse holographic sampling and data inversion.

This chapter is organized as follows. Section 4.2 describes the theoretical background for diffraction tomography and holographic measurement. Hologram recording geometry and resolution metrics are also discussed in this section. Section 4.3 summarizes the TV-minimization algorithm used for 3D object estimation from a 2D digitized composite hologram. Also, simulations of 2D holographic measurements and subsampled 2D holographic measurements help to analyze the impact of various sampling schemes on 3D object estimation using TV-minimization. Section 4.4 describes the experimental platform. Section 4.5 presents TV-minimization and back-propagation reconstructions. Finally, Section 4.6 provides a summary of the chapter and concluding remarks.

4.2 Theory

The ultimate goal is to make the smallest number of measurements about a 3D (x', y', z') object $f_o(\mathbf{r}')$, where $\mathbf{r}'$ is a 3D spatial vector, such that it is possible to reconstruct $f_o(\mathbf{r}')$ with minimal error. Rather than attempting to form an image of $f_o(\mathbf{r}')$ point by point, the approach in this chapter is based on making measurements

in the far-field where spatial frequencies (u_x and u_y) are measured. To do this, a hologram is recorded. A hologram $g(\mathbf{r_h})$ is a record of the interference between two wavefields, a reference field $E_r(\mathbf{r})$ and an object scattered field $E_o(\mathbf{r})$. To record a hologram, a square-law detector in the hologram plane $\mathbf{r_h} = (x, y, z_h)$ measures a time-averaged intensity of the interference,

$$\begin{aligned} g(\mathbf{r_h}) &= \mid E_r(\mathbf{r_h}) + E_o(\mathbf{r_h}) \mid^2 \\ &= \mid E_r(\mathbf{r_h}) \mid^2 + \mid E_o(\mathbf{r_h}) \mid^2 + 2 \mid E_r(\mathbf{r_h}) E_o(\mathbf{r_h}) \mid \cos\left[\theta_r(\mathbf{r_h}) - \theta_o(\mathbf{r_h})\right] \end{aligned} \tag{4.1}$$

where $\theta_r(r_h)$ represents the phase associated with the propagated reference wavefield and $\theta_o\left(\mathbf{r_h}\right)$ represents the phase associated with the propagated object wavefield. The object field is generated by illuminating a 3D object $f_o(\mathbf{r}')$ by an on-axis plane wave $\exp(-2\pi i \mathbf{u_o} \cdot \mathbf{r})$ where $\mathbf{u_o} = (u_{x_o}, u_{y_o}, u_{z_o})$. The 3D object $f_o(\mathbf{r}')$ represents an object scattering amplitude, where after reference plane wave illumination a fraction of the energy is either transmitted or reflected at a point in three-dimensional space. Note that it is assumed that the object does not induce any phase change in an incident wavefield through polarization or bi-refringence.

If the object is transmissive and located z_h distance away from the hologram

plane, under the Born approximation the scattered field is

$$E_o(\mathbf{r_h}) = \frac{-\pi}{\lambda^2} \int E_r(\mathbf{r}')f_o(\mathbf{r}')h(\mathbf{r}_h - \mathbf{r}')d\mathbf{r}', \tag{4.2}$$

where $h(\mathbf{r_h} - \mathbf{r}')$ is the shift-invariant impulse response and $E_r(r')$ is the reference plane wave. For scalar waves in homogeneous space, the impulse response is

$$h(\mathbf{r_h} - \mathbf{r}') = \frac{\exp(2\pi i \mid \mathbf{r_h} - \mathbf{r}' \mid /\lambda)}{\mid \mathbf{r_h} - \mathbf{r}' \mid}. \tag{4.3}$$

We can reformulate the convolution integral in Eq. (4.2) using the Fourier convolution theorem. The Fourier transform of the scattered field along the transverse axes in the recording plane is

$$\widehat{E_0}(u_x, u_y, z_h) = \frac{1}{i\pi\lambda}\widehat{f_o}\left(u_x - u_{x_o}, u_y - u_{y_o}, \sqrt{\frac{1}{\lambda^2} - u_x^2 - u_x^2} - u_{z_0}\right) G_{2D}(u_x, u_y, z) \tag{4.4}$$

where

$$G_{2D}(u_x, u_y, z) = \frac{\exp\left(2\pi i z\sqrt{\frac{1}{\lambda^2} - u_x^2 - u_y^2}\right)}{\sqrt{\frac{1}{\lambda^2} - u_x^2 - u_y^2}}, \tag{4.5}$$

$\widehat{f_o}$ is the 3D Fourier-transform of the object density, and the exponential term represents a propagation transfer function. Under the small angle approximation, $u_{z_o} =$

$1/\lambda$ and $u_x, u_y \leq 1/\lambda$. The frequency domain scattered field is then approximated by

$$\widehat{E_o}(u_x, u_y, z) = \frac{1}{i\pi\lambda}\widehat{f_o}\left(u_x - u_{x_o}, u_y - u_{y_o}, -\frac{\lambda}{2}\left(u_x^2 + u_y^2\right)\right)\exp\left(2\pi i z\sqrt{\frac{1}{\lambda^2} - u_x^2 - u_y^2}\right). \tag{4.6}$$

As discussed in Section 4.3, digital processing of the Gabor hologram aims to isolate the scattered field, $E_o(\mathbf{r_h})$, signal term from background and conjugate terms. Assuming the recorded hologram measures $E_o(\mathbf{r_h})$ directly and $E_r(\mathbf{r_h}) = 1$, Eq. (4.6) demonstrates that a 2D hologram captures a 3D parabolic slice of the object's band volume. Figure 4.1[†] describes tomographic sampling of a 3D band volume in a Gabor geometry. Typically, the illumination (or the object) must be rotated to fully sample the 3D band volume. To increase longitudinal resolution, the system may alternatively be scanned in frequency. Instead of scanning in the frequency domain on the surface of a sphere, this approach allows one to scan a spherical shell with radii corresponding to a wavelength range. In [21], CS theory was used to estimate the 3D distribution of $f(\mathbf{r}')$ from a single holographic image without scanning in frequency or rotating the object. Instead sparsity was exploited. This chapter extends 3D tomographic estimation from 2D holographic measurements to millimeter wavelengths.

[†](*Peer review*)C. F. Cull, D. A. Wikner, J. N. Mait, M. Mattheiss, and D. J. Brady, "Millimeter-wave compressive holography," Appl. Opt. (2010)

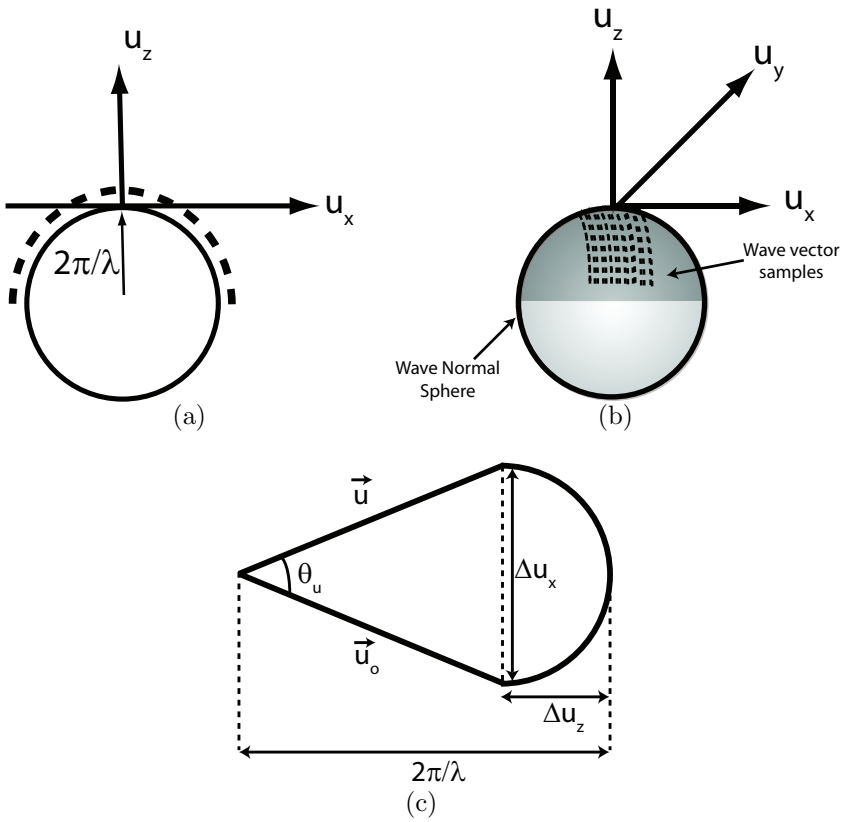

Figure 4.1: Fourier-transform domain sampling of the object band volume in a transmission geometry. (a) 2D slice of a 3D sphere where the dotted-line represents the measurement from single plane wave illumination. (b) Rectilinear pattern represents wave vectors sampled by the hologram due to a finite detector plane sampling. (c) Wave normal sphere cross-section for spatial and axial resolution analysis.[†]

4.2.1 Hologram recording geometry

The geometry used to record the hologram impacts the post-detection signal processing and the ability to reconstruct the image. In an off-axis geometry [78], the signal and its conjugate are separated from each other in frequency space and from the on-axis undiffracted energy (see Fig. 4.2(a)[†]).

Note that the maximum spatial frequency u_{max} that the detector can record is limited by the sampling pitch (dx) of the detector,

$$u_{max} = \frac{1}{2dx}. \tag{4.7}$$

The detector pixel pitch is set by the WR-08 waveguide size (2.32 mm $\times$ 1.08 mm), so the maximum spatial frequency recorded in the vertical direction is 0.463 mm^{-1} and in the horizontal direction is 0.216 mm^{-1}.

Figure 4.2(a) shows that the information content of the object and the pixel pitch of the detector impose minimum and maximum limits on the angle θ_{cz} of the off-axis reference. For simplicity, the reference beam is assumed to have no y-component. To separate the object from its squared magnitude without ambiguity due to detector aliasing or from confusion with undiffracted terms, the angle of the off-axis beam

[†](*Peer review*)C. F. Cull, D. A. Wikner, J. N. Mait, M. Mattheiss, and D. J. Brady, "Millimeter-wave compressive holography," Appl. Opt. (2010)

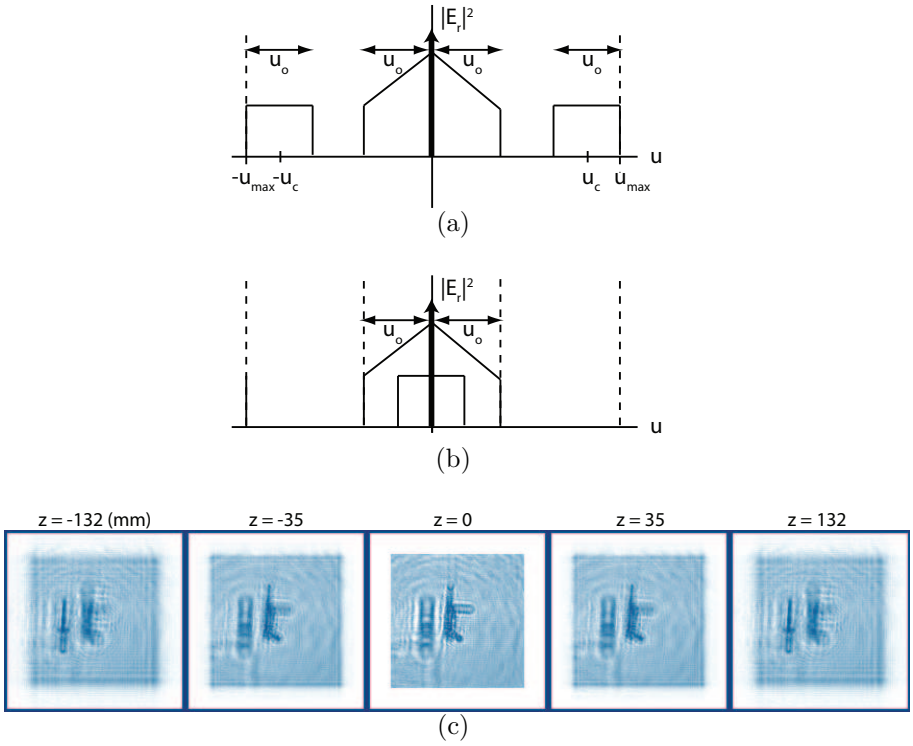

Figure 4.2: (a) Spectrum for an off-axis hologram recording depicting an inherent increase in bandwidth for adequate object separation from undiffracted terms. (b) Spectrum for a Gabor hologram recording depicting the overlay of undiffracted, object, and conjugate terms. (c) Transverse slices from linear inverse propagation results at various z-planes.[†]

must satisfy

$$\theta_{cmin} \leq \theta_{cz} \leq \theta_{cmax}, \tag{4.8}$$

where

$$\theta_{cmax} = \sin^{-1}\left[\left(\frac{\lambda}{2}\right)\left(\frac{1}{dx} - u_B\right)\right], \tag{4.9}$$

$$\theta_{cmin} = \sin^{-1}\left(3\frac{\lambda u_B}{2}\right), \tag{4.10}$$

and u_B is the spatial frequency bandwidth of the object.

Use of an off-axis reference beam simplifies the reconstruction since digital signal processing allows one to yield an estimate of the object field

$$\tilde{g}_{\text{offaxis}} = E_r(\mathbf{r_h})^* E_o(r_h). \tag{4.11}$$

In an on-axis geometry it is more difficult to separate the object field from the undiffracted, zero-order fields and from its conjugate. The overlap of these three fields degrades resolution and contrast in the object reconstruction. One can apply DC suppression techniques to enhance object reconstructions [15, 79, 80] and measurements of the energy in the reference beam alone can be made and subtracted from the hologram,

$$\tilde{g}_{\text{onaxis}} = \mid E_o(\mathbf{r_h}) \mid^2 + E_r^*(\mathbf{r_h})E_o(\mathbf{r_h}) + E_r(\mathbf{r_h})E_o^*(\mathbf{r_h}). \tag{4.12}$$

In this chapter, a hologram is recorded in an on-axis geometry since the need for an increased bandwidth in the off-axis case outweighs the complexity for on-axis object isolation.

4.2.2 Hologram plane sampling and resolution metrics

In the system implementation, the field $g(\mathbf{r_h})$ is sampled and digitized into a 2D matrix by translating a point detector in x and y at the hologram plane z_h. An analytical discussion of the discrete model is detailed in [21] and addressed in Section 4.3.

Holographic measurements captured digitally, by a scanning detector, are related to measurements made in the spatial frequency domain. The total number of detector measurements N is

$$N = n_x n_y, \tag{4.13}$$

where n_x and n_y represent the number of measurements along each spatial dimension in x and y. Given the detector sampling pitch (dx), the number of measurements (n_x) in the hologram plane along the horizontal dimension is given by

$$n_x = \frac{W_x}{dx}, \tag{4.14}$$

where

$$W_x = \frac{\lambda z}{\Delta x_o}, \tag{4.15}$$

z is the distance between the object and the detector, Δx_o is the one-dimensional spatial resolution with which we wish to image the object, and W_x refers to the spatial extent of a diffracted object (Δx_o). The inverse scaling relationship arises from the conjugate relationship between the object and the hologram [81].

Detector sampling over a finite field size affects sampling resolution in the frequency-domain. The sampling resolution, Δ_u, in the frequency domain along both the horizontal and vertical dimensions (u_x and u_y), assuming $n_x = n_y$, is determined by the sampling field size at the detector plane, $\Delta_u = 1/(2n_x dx)$. The maximum spatial frequency sampled by the detector is equal to u_{max} in Eq. (4.7).

Resolution metrics, lateral (Δ_x) and axial (Δ_z), for the Gabor geometry are determined by the illumination wavelength and the system numerical aperture (NA). Based on the Gabor recording geometry, the NA is defined by

$$\begin{aligned} n \sin \theta_u &= \frac{W_x}{2z} \\ &= \frac{\lambda}{2\Delta x_o}, \end{aligned} \tag{4.16}$$

where n is the refractive index of air and θ_u is the half-angle subtended by the object to half the spatial extent of the hologram plane ($W_x/2$). Recall that the spatial resolution is related to the inverse scaling relationship in the frequency domain. The half-angle, θ_u, is also defined as the angular bandwidth sampling on the wave normal

sphere due to system NA. Thus, the NA can also be described in the spatial frequency domain. The wave vector geometry for hologram recording is shown in Fig. 4.1(b-c). Considering the geometry in Fig. 4.1(c) we write

$$\sin(\theta_u) = \frac{\Delta u_x}{\mid \mathbf{u} \mid}, \tag{4.17}$$

where under the small angle approximation

$$\mid \mathbf{u} \mid \theta_u = \Delta u_x. \tag{4.18}$$

Assuming that $NA \approx \theta_u$ and $\mid \mathbf{u} \mid \approx 1/\lambda$, the spatial resolution is equal to

$$\Delta_x = \frac{\lambda}{NA}. \tag{4.19}$$

Similarly, from the wave vector geometry, the spatial frequency resolution along z (Δu_z) is determined by

$$\begin{aligned} \Delta u_z &= \Delta u_{z,max} - \Delta u_{z,min} \\ &= \mid \mathbf{u} \mid (1 - \cos(\theta_u)) \\ &= \mid \mathbf{u} \mid \theta_u^2. \end{aligned} \tag{4.20}$$

Under the small angle approximation, the axial resolution is

$$\Delta_z = \frac{\lambda}{NA^2}. \tag{4.21}$$

After substituting the expression for NA from Eq. (4.16) into Eq. (4.19) and Eq. (4.21), we see that lateral resolution is also defined as $\Delta_x \approx 2\Delta x_o$ and range resolution is defined as $\Delta_z \approx 4\Delta x_o^2/\lambda$. Defining the lateral and axial resolution using NA describes resolution in terms of system geometry (a function of object distance), whereas the second metric is modeled as a function of feature size, Δx_0. The maximum of the two measures for lateral and axial resolution provides a baseline metric for resolution. These metrics are used to evaluate resolution from TV-minimization object reconstructions in Section 4.5.

This section provided motivation for implementing a Gabor geometry instead of an off-axis approach. The impact of detector sampling at the hologram plane was addressed and a relation between object sampling and frequency domain sampling was discussed. Finally, theoretical resolution metrics were derived.

4.3 Reconstruction methods and Simulations

In this section, two reconstruction methods are discussed: 3D object estimation from a Gabor hologram and 3D object estimation from randomly subsampled Gabor holo-

graphic measurements. Subsampling is implemented to further analyze the impact of compressive measurement on 3D object estimation.

The continuous model for Gabor holography, modeled under the first Born approximation, is shown in Eq. (4.2). The detector plane is located at the $z_h = 0$ plane in the $\mathbf{r}(x, y, z_h)$ coordinate system. The object data, f, is located in the $\mathbf{r}$'(x', y', z') coordinate system. The recorded hologram in Eq. (4.1) can be reformulated when assuming that $E_r(\mathbf{r_h}) = 1$ and if operations on $f_o(\mathbf{r}')$ in the convolution integral in Eq. (4.2) are expressed using an operator, H. After squared-reference field subtraction, we can represent the recorded hologram in algebraic notation using

$$g = \mid Hf \mid^2 + Hf + H^*f + n, \tag{4.22}$$

where g is an $N \times 1$ vectorized detector measurement, H is a 2D discrete system matrix, f is an $M \times 1$ vectorized object representation ($f_o(\mathbf{r}')$), and n is the noise associated with the measurement. If the object-squared field contribution is ignored in Eq. (4.22), a linear relationship between the detector measurement and object field distribution, $g = Hf$, can be established.

Once the digital hologram is recorded, the goal is to estimate the object distribu-

tion, f. The digitized holographic measurement in [21] is represented as

$$g_{n_1,n_2} = \sum_{l} \mathbb{F}_{\mathbf{2D}}^{-\mathbb{1}} \left\{ \widehat{f}_{m_1,m_2,l} \exp\left(il\Delta_z \sqrt{\frac{1}{\lambda^2} - m_1^2\Delta_u^2 - m_2^2\Delta_u^2} \right) \right\}_{n_1,n_2}, \tag{4.23}$$

where $\mathbb{F}_{\mathbf{2D}}^{-\mathbb{1}}$ represents the 2D inverse fast Fourier transform (FFT) operation, $\widehat{f}$ represents the FFT of the object distribution, and the exponential term encompasses the transfer propagation function. Indices n_1 and n_2 are discrete indices for each spatial dimension (x and y), l is the discrete index for z, m_1 and m_2 are the Fourier-transformed indices, Δ_z is the resolution cell along the axial plane, and Δ_u is the sampling resolution in the Fourier-domain due to discretization by the detector plane. Using Eq. (4.23), we can model H in Eq. (4.22) as

$$H = \mathbb{F}_{2D}^{-1}\mathbb{Q}\mathbb{F}_{2D}. \tag{4.24}$$

The adjoint system model of Eq. (4.23) is

$$f = H^{\dagger}g \tag{4.25}$$

where $H^{\dagger}$ is the adjoint operator defined as

$$H^{\dagger} = \mathbb{F}_{2D}\mathbb{Q}^{\dagger}\mathbb{F}_{2D}^{-1}. \tag{4.26}$$

Note that † represents the Hermitian transpose operation. The forward system matrix, H, models scattering/object field propagation via two FFTs and a quadratic phase term [81]. The FFT and inverse FFT operators are diagonal matrices and the exponential term in Eq. (4.23) is expressed as a propagation quadratic phase matrix, $\mathbb{Q} = Q_{l,m_1\times m_2}$, where

$$Q_{l=1,m_1,m_2} = \exp\left(\imath l \Delta_z \sqrt{\frac{1}{\lambda^2} - m_1^2\Delta_u^2 - m_2^2\Delta_u^2}\right). \tag{4.27}$$

The adjoint model in Eq. (4.25) is used for linear backpropagation object estimation (see Appendix A.5 for forward and adjoint model matrix implementation details and sensing matrix (H) CS coherence properties).

Inverse propagation, otherwise known as backpropagation, is a linear method for 3D object field reconstruction. Figure 4.2(c)† shows digitally backpropagated object fields at different z-planes. This result demonstrates the challenges associated with linear inverse propagation, as the undiffracted and out-of-focus field contributions make object range detection challenging. Linear backpropagation provides an estimate for the 3D field and not the 3D object density. Minimizing the contribution of the undiffracted field or twin-image problem has been explored [77, 82]. Conventional methods to increase range resolution require either multiple wavelengths or

†(*Peer review*)C. F. Cull, D. A. Wikner, J. N. Mait, M. Mattheiss, and D. J. Brady, "Millimeter-wave compressive holography," Appl. Opt. (2010)

multiple projections [83, 84]. By exploiting results from compressive sensing, this project demonstrates that it is possible to isolate objects along an axial plane where range resolution is consistent with the object's spatial extent using only a single 2D recording.

Recently, the TwIST 2D TV-minimization algorithm was adapted for 3D tomographic estimation from a single digitized 2D hologram [21,85]. Forward and adjoint operators in Eq. (4.24) and Eq. (4.25) are incorporated into the TwIST algorithm. Analytical rigor associated with the algorithm has previously been formulated [21]. The algorithm minimizes a convex quadratic problem with the addition of a sparsity constraint. The sparsity constraint is enforced on the gradient (see Eq. (4.30)) of the object estimate, f. Applying the constraint enables improved 3D tomographic estimation from a 2D measurement [86] since the twin-image problem associated with the inverse propagation method is reduced. Even though the effect of the nonlinear term $\mid H\left[f\right] \mid^2$ is neglected in the system model shown in Eq. (4.22), a new term, e, is added to model measurement error. The final measurement model becomes

$$g = 2\Re\left\{H\left[f\right]\right\} + n + e. \tag{4.28}$$

In this chapter, a convex quadratic function is minimized using TV regularization

denoted by

$$f^* = \arg\min_f \parallel g - Hf \parallel_2^2 + \tau\Phi_{TV}(f), \tag{4.29}$$

where f^* is the 3D object estimate and τ is the regularization constant. The Φ_{TV} function is defined as

$$\Phi_{TV} = \sum_l \sum_{i,j} \sqrt{(f_{i+1,j,l} - f_{i,j,l})^2 + (f_{i,j+1,l} - f_{i,j,l})^2}, \tag{4.30}$$

where l represents the discrete index in z and i and j correspond to discrete indices for a 2D (x, y) spatial extent. The ϕ_{TV} function preserves edges while imposing smoothness on a solution. The regularization constant, τ, determines the convergence and image quality of the estimate. The TV-regularization algorithm in Eq. (4.29) is considered as a special case in a Bayesian framework since TV regularization is similar to determining a maximum a posteriori estimate with a TV-prior distribution. TV-minimization reconstructions enable twin-image reduction and squared-field reduction, which are otherwise dominant in linear inverse propagation. Figure 4.3[†] shows TV-minimization object reconstructions. Undiffracted energy contributions are localized at the $z = 0$ plane, while twin-image contributions are weakly scattered to the object field planes and primarily located at the conjugate object planes

[†](*Peer review*)C. F. Cull, D. A. Wikner, J. N. Mait, M. Mattheiss, and D. J. Brady, "Millimeter-wave compressive holography," Appl. Opt. (2010)

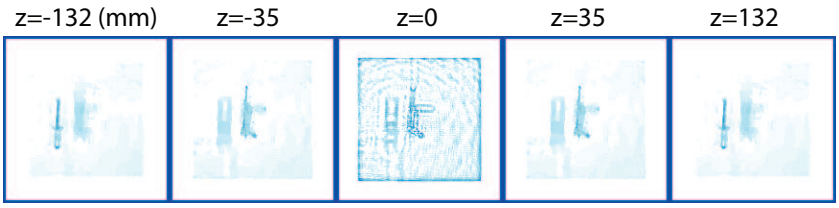

Figure 4.3: Transverse slices from TV-minimization reconstructions at different z-planes. A dominant squared-field term is confined to the z=0 plane.[†]

(i.e. $z \leq 0$ in Fig. 4.3). Compared to inverse propagation results in Fig. 4.2(b), Fig. 4.3 demonstrates twin-image suppression and squared-field suppression since TV-imposed sparsity enables estimation of the object density and not the field distribution.

In this paper, the impact of subsampled holographic measurements on object reconstruction is also analyzed. A binary-valued, pseudo-random transmittance function, $t(x, y)$, is applied to reduce the number of measurements at the hologram plane. The transmittance function is defined as

$$t(x, y) = \sum_{p,q} t_{p,q} rect \left[\frac{x - p\Delta_T}{\Delta_T}, \frac{y - q\Delta_T}{\Delta_T} \right]. \tag{4.31}$$

The pseudo-random measurement matrix contains transmissive (1) and opaque (0) openings. The sampling pitch, Δ_T, of the matrix is equal to the receiver sampling pitch. Similarly, indices for the discrete representation of the measurement matrix and detector matrix are equivalent ($p = n_1$ and $q = n_2$). The sparse detector mea-

surement, $\breve{g}$, is defined as

$$\breve{g}_{n_1,n_2} = t_{n_1,n_2} g_{n_1,n_2}. \tag{4.32}$$

If the discrete transmittance function, t_{n_1,n_2}, for the aperture is represented as a diagonal matrix, W, then the new forward and adjoint models are represented as

$$g = W F_{2D}^{-1} Q F_{2D} f \tag{4.33}$$

and

$$f = F_{2D}^{\dagger} Q^{\dagger} \left[F_{2D}^{-1}\right]^{\dagger} W^{\dagger} g. \tag{4.34}$$

The TV-minimization algorithm is adapted for hologram measurement subsampling using the aforementioned forward and adjoint models. Sparse detector measurements are motivated by an existing need to reduce scan times in MMW imaging applications. Simulations incorporating the above system model are explored in the next section to study the impact of a subsampled 2D hologram image on 3D tomographic reconstruction. The goal is to show that a reduction in the number of measurements can be achieved without a huge compromise in 3D object reconstruction.

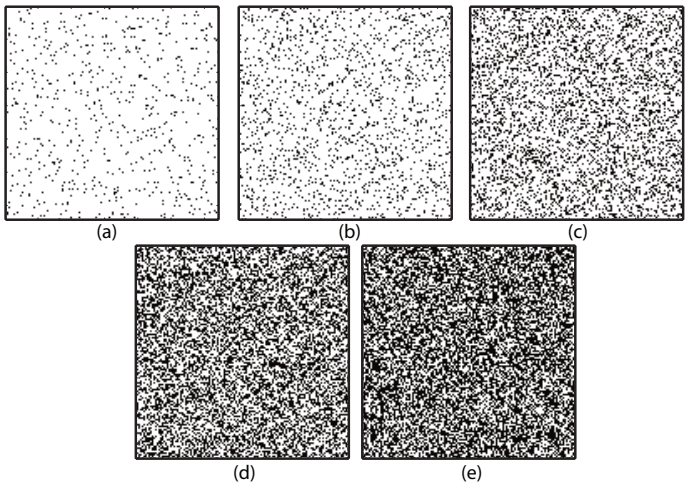

Figure 4.4: Sampling windows for sparse measurement where (a) 3.9%, (b) 9.77%, (c) 23.83%, (d) 44.56%, and (e) 54.68% measurements are removed.[†]

4.3.1 Simulation Results

In simulation, two approaches are undertaken to analyze the impact on 3D object estimation using TV-minimization. The first approach involves the recording of 2D digitized holographic measurement. The second approach studies the impact of subsampled/sparse 2D holographic measurement on 3D object estimation. In this section, the simulated detector measurements are constructed using Eq. (4.22). The sparse measurement model is based on Eq. (4.33) and incorporated into Eq. (4.22). Recall that for sparse measurement, a pseudo-random transmittance function is applied to holographic measurements. Examples of the sampling matrices under test are shown in Fig. 4.4[†]. TV-minimization results were analyzed when detector measurements

[†](*Peer review*)C. F. Cull, D. A. Wikner, J. N. Mait, M. Mattheiss, and D. J. Brady, "Millimeter-wave compressive holography," Appl. Opt. (2010)

were uncorrupted and corrupted by additive white gaussian noise (AWGN). Noise was added to simulated detector measurements using the MATLAB 'awgn' command, where the measurement signal-to-noise ratio (SNR) was specified. Also, the impact of 0 to 54.68% 2D measurement reduction on 3D object estimation was analyzed. For 3D object estimation, two inversion methods are compared: a linear backpropagation method and nonlinear TV-minimization. To quantify reconstruction efficacy the peak signal-to-noise ratio (PSNR) metric was used . PSNR is defined as

$$PSNR(dB) \stackrel{\text{def}}{=} 20\log_{10}\left\{\frac{\text{MAX}_A}{\frac{1}{n_x n_y d}\sum_{i=1}^{n_x}\sum_{j=1}^{n_y}\sum_{l=1}^{d}[A_{i,j,l}-B_{i,j,l}]^2}\right\}, \tag{4.35}$$

where A represents the synthetic object, B represents the object estimate, n_x and n_y represent the number of detector pixels along each spatial dimension, d represents the number of axial planes, and PSNR units are in decibels (dB). As expected, PSNR decreases as the percentage of samples removed increases. Also, the addition of AWGN decreases PSNR.

Simulation system parameters mimic that of the experimental platform. Each simulated hologram measures 128×128 pixels with a pixel pitch of 2.32 mm. The synthetic objects were modulated by a 94 GHz reference illumination field. Two synthetic 3D objects, synthetic slits and a synthetic gun and dagger object, were tested. The objects were located at different depths along the axial plane. The axial

resolution definition in Section 4.2.2 was used as the metric for object separation along the axial plane. The synthetic slit targets follow this convention. For example, the smallest object feature size of the synthetic slit target measured one wavelength (≈ 3 mm) and the object distance from the detector measured 20 mm, which resulted in an object separation distance of approximately 10 mm. The synthetic gun and dagger target attempts to mimic experimental measurements detailed in Section 4.5. Further, TV-minimization reconstruction depths were based on the predetermined object locations. Note that the synthetic targets are 2D and have a uniform amplitude. Real objects explored in Section 4.5, however, are 3D and located in multiple planes. The impact of 3D spatially extended objects along multiple axial planes was not investigated in this chapter.

First, a digital hologram of a uniform 3D slit object was simulated using Eq. (4.22). Row one, row two, and row three of the slit object were located in three separate planes: 20 mm, 30 mm, and 40 mm away from the detector plane. The slits are 21 pixels long. Row one contained three sets of three-pixel-wide slits. Slit pairs were separated by one, two, and three pixels, respectively. Row two contained three sets of five-pixel-wide slits. Slit pairs were separated by two, four and one pixel(s), respectively. Row three consisted of three sets of two-pixel-wide slits. Slit pairs were separated by one, two, and four pixels, respectively. In the post-detection pro-

cess, linear backpropagation and TV-minimization reconstructions are compared and shown in Fig. 4.5[†]. Note that the reconstructions in Fig. 4.5 show simulated detector measurements corrupted by AWGN at a 30 dB measurement SNR. Backpropagation accurately estimates the object wavefield, while TV-minimization accurately estimates the object spatial extent along the axial plane. Improved twin-image suppression was obtained with TV-minimization. Note that the slit object addressed spatial resolution limitations as fewer holographic measurements were used for data inversion. These limitations were object size dependent. A set of five-pixel-wide (11.6 mm) slits separated by four pixels (9.23 mm) were resolved after nonlinear inversion even though 44.46% of the holographic measurements were removed. Linear backpropagation object field estimation was challenging when 54.68% of the holographic measurements were removed. A closer inspection of Fig. 4.5 demonstrates other spatial resolution limitations based on smaller object feature sizes.

Second, a hologram of a 3D synthetic object consisting of a uniform amplitude 2D gun and a 2D dagger was simulated. The synthetic 2D objects were placed at different distances along the axial plane. The synthetic data were modeled after experimental data in Fig. 4.7[†]. The synthetic gun and dagger were located 30 mm

[†](*Peer review*)C. F. Cull, D. A. Wikner, J. N. Mait, M. Mattheiss, and D. J. Brady, "Millimeter-wave compressive holography," Appl. Opt. (2010)

[†](*Peer review*)C. F. Cull, D. A. Wikner, J. N. Mait, M. Mattheiss, and D. J. Brady, "Millimeter-wave compressive holography," Appl. Opt. (2010)

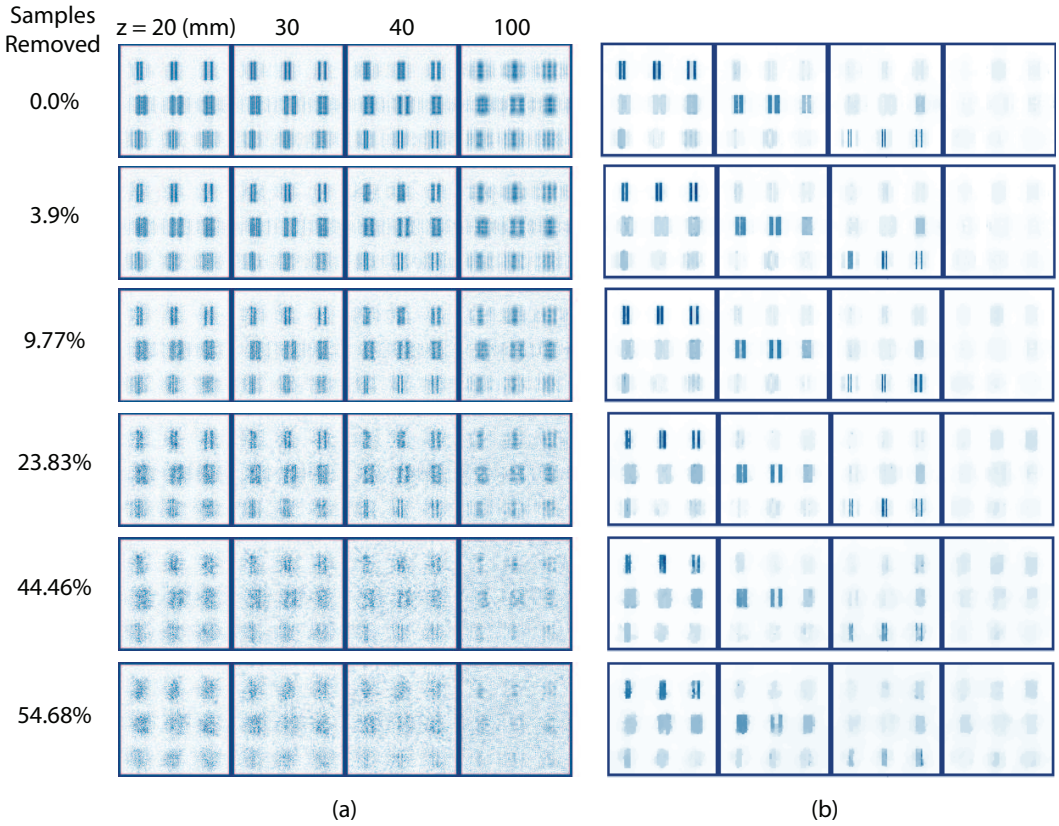

Figure 4.5: Synthetic 3D slit object results with an applied transmittance function and corrupted by AWGN at a 30 dB measurement SNR using (a) backpropagation and (b) TV-minimization for 3D tomographic object estimation. Various values for τ (0.2 – 1.0) are used for sparsely sampled (0.0 – 54.68%) TV reconstructions† (see Table 4.1)

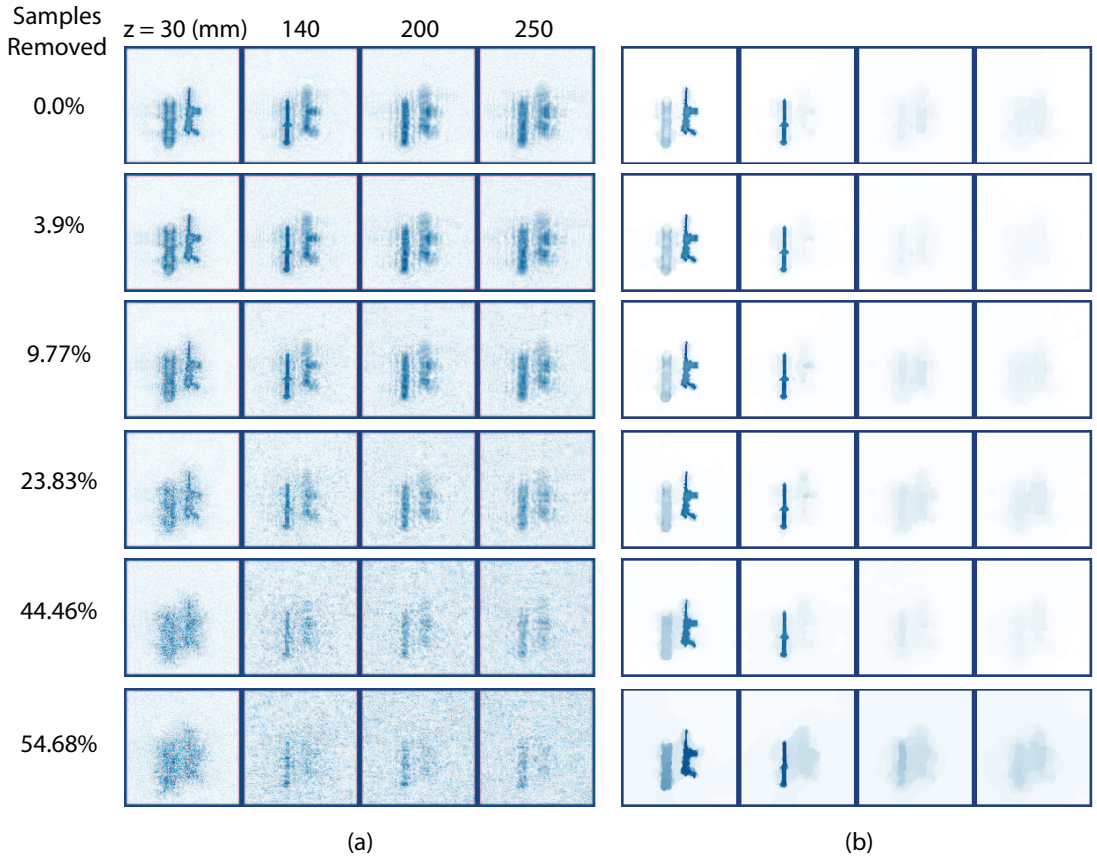

Figure 4.6: Synthetic 3D dagger and gun object results with an applied transmittance function and corrupted by AWGN at a 30 dB measurement SNR using (a) backpropagation and (b) TV-minimization for 3D tomographic object estimation. A τ value of 0.2 is used for TV-minimization reconstructions from sparsely sampled detector measurements corrupted by AWGN (see Table 4.1).[†]

and 140 mm away from the hologram plane. The smallest feature on the gun, located at the barrel, measured two pixels (4.64 mm). The smallest feature on the dagger, located at the edge of the blade, measured four pixels (9.28 mm). Figure 4.6 presents linear and nonlinear inversion estimates of the holographically measured data corrupted by AWGN at a 30 dB measurement SNR. While linear backpropagation fails to estimate the object field both spatially and longitudinally with 54.68% of the measurements missing, TV-minimization succeeds in providing adequate spatial resolution and object localization along the axial plane.

While Fig. 4.5 and Fig. 4.6[†] only consider reconstructions from 3D synthetic targets corrupted by AWGN at a single measurement SNR, Fig. 4.8 quantitatively summarizes the effect over a range of AWGN noise levels for different subsampling strategies. Simulation results in Fig. 4.8 use various values of τ (.2 - 1) for 3D object reconstructions. The number of iterations, however, was fixed. Values for τ were chosen by trial and error to visually produce the best object contrast in the reconstruction estimate. The number of iterations were chosen such that the relative difference in the objective function was nominal. In Fig. 4.8, 13 different measurement SNR noise levels were analyzed. Using the same algorithm parameters, multiple reconstruction estimates at each noise level were consistent. The TV-minimization

[†](*Peer review*)C. F. Cull, D. A. Wikner, J. N. Mait, M. Mattheiss, and D. J. Brady, "Millimeter-wave compressive holography," Appl. Opt. (2010)

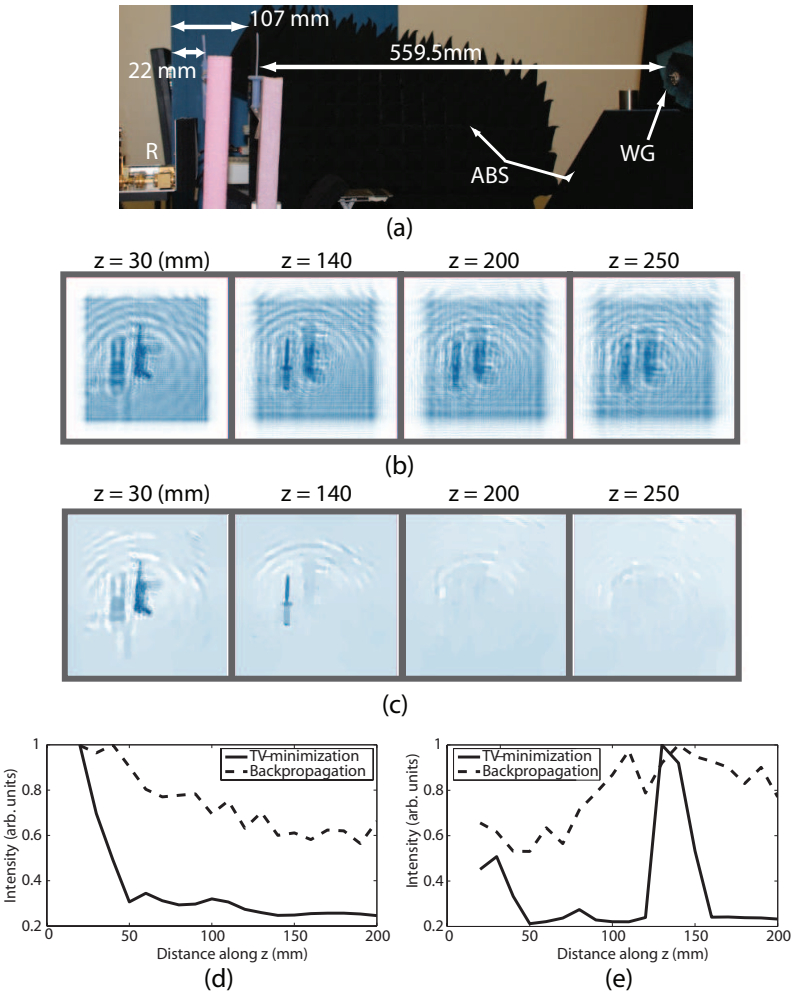

Figure 4.7: Experiment with a polymer model gun and dagger placed at two different distances along the axial plane.(a) Photograph of the experiment. Transverse slices in four different z-planes of the (b) backpropagated and (c) TV-minimization reconstructions. Amplitude pixel (x,y) as a function of z, in 10 mm increments, where TV-minimization and backpropagation for a central point on the (d) barrel of the gun and (e) on the blade edge of the dagger are plotted.[†]

reconstruction of the synthetic 3D slit target for all sampling schemes converged at a 30 dB measurement SNR with a PSNR range between 25 dB and 30 dB. The results in Fig. 4.8(a) show that a 54.7% measurement reduction only incurs a 5 dB loss in PSNR. In comparison, the synthetic 3D gun and dagger object converged around a 40 dB measurement SNR which yielded approximately a 32 dB PSNR. For the synthetic dagger and gun object case, measurement reduction between 0% and 54.68% provided a PSNR range between 29 dB and 32 dB. Since the 3D gun and dagger gradient sparsity is smaller, it was not surprising that TV-minimization results yielded a higher PSNR compared to the 3D slit target. Lastly, backpropagation results for both 3D synthetic objects in Fig. 4.8(c,d) converged at a 20 dB measurement SNR for all measurement schemes and yielded a low reconstruction PSNR (17 - 20 dB).

In simulation, object sparsity can be measured by calculating the number of nonzero gradients for each 3D synthetic object under test. Object sparsity was measured for each synthetic 3D object by calculating the gradient and totaling the nonzero values. The nonzero gradient, $\mid \nabla f_{i,j,l} \mid$, at the $(i,j)^{th}$ pixel location in the l^{th} axial plane was calculated using

$$\mid \nabla f_{i,j,l} \mid = \sqrt{\left(f_{i+1,j,l} - f_{i,j,l}\right)^2 + \left(f_{i,j+1,l} - f_{i,j,l}\right)^2}. \tag{4.36}$$

Note that larger 3D objects produce more nonzero gradients. The nonzero gradients

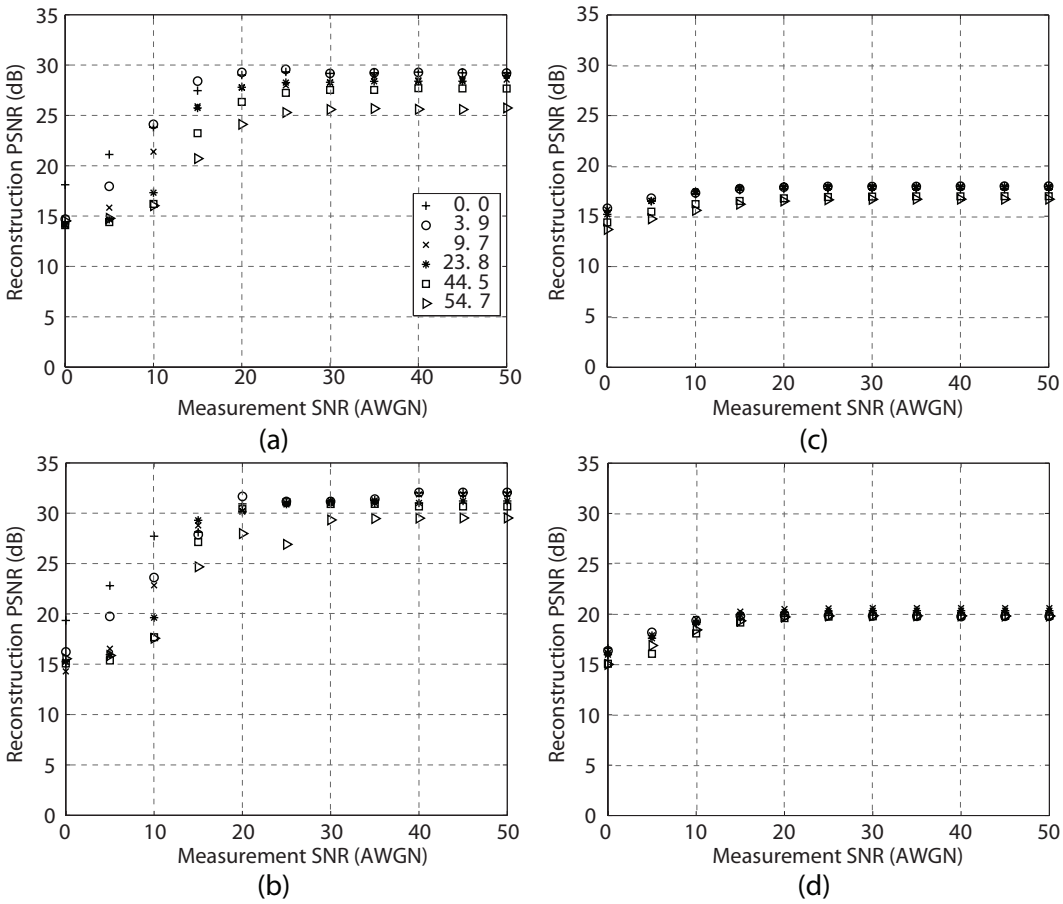

Figure 4.8: Plot of reconstruction PSNR (in dB) versus measurement SNR (in dB) from millimeter-wave holography detector measurements corrupted by AWGN. TV-minimization reconstruction results with 0.0 - 54.7% measurement reduction are shown for the (a) synthetic slit target and (b) synthetic gun and dagger target. Backpropagation reconstruction results with 0.0 - 54.7% measurement reduction are shown for the (c) synthetic slit target and (d) synthetic gun and dagger target.[†]

calculated for the synthetic 3D slit object and the synthetic 3D dagger and gun object were 2580 and 1129. Recall that the simulated 2D hologram measured 128×128 pixels. The ratio between the total number of measurements (N) recorded at the detector plane to the object sparsity/nonzero gradients calculated was analyzed. This ratio is listed in Table 4.1 as the *sparsity ratio*. In CS, the number of measurements required for adequate signal estimation is $N \geq SC \log(M)$ [21, 73], where S represents the number of nonzero gradients/sparsity calculated in the gradient domain, C represents an empirical constant value, and M represents the original size of the vectorized object signal f. The reconstruction of the 3D slit object with a 54.68% measurement reduction was evaluated by analyzing the PSNR and sparsity ratio. A low PSNR was attributed to a low sparsity ratio shown in Table 4.1. For example, a 3D synthetic gun and dagger object with a 54.68% measurement reduction yielded a PSNR of 26.09 and had a sparsity ratio of 6.7. Since the sparsity ratio for the synthetic slit object with the same measurement reduction yielded a low PSNR, one

Table 4.1: Synthetic 3D Slit (ST) and 3D Gun and Dagger (GD) Sparsity

	% Removed	ST Sparsity Ratio	GD Sparsity Ratio
1	0	6.35	14.51
2	3.9	6.10	13.95
3	9.77	5.73	13.09
4	23.83	4.84	11.05
5	44.46	3.53	8.06
6	54.68	2.88	6.58

would need to record a larger number of holographic measurements for an improved reconstruction PSNR. While the synthetic 3D slit object addressed spatial resolution limitations and gradient domain object sparsity concerns in simulation, the synthetic 3D gun and dagger object was used to evaluate experimental reconstructions taken of a semi-transparent gun and dagger placed along an axial plane in Section 4.5.

4.4 Experimental setup

Simulations in the previous section indicate that digital holography combined with a TV post-detection process is effective. To validate the simulations, various experiments were conducted to measure Gabor holograms. The 2D hologram was recorded in a Gabor geometry as shown in Fig. 4.9[†]. RF energy was generated from a tunable InP Gunn diode oscillator and coupled to a WR-10 open waveguide with dimensions 2.54 mm (W) $\times$ 1.27 mm (H). The oscillator was tuned to 94 GHz (see Appendix A.6 for spectral linewidth distribution) and after attenuation was found to radiate with a peak power of 100 mW. In the far-field ($4D^2/\lambda$) of the waveguide aperture, a collimated/reference beam was directed towards an object having spatial extent, L_x in Fig. 4.9. Actual reference beam dimensions (B) were calculated using the illumination wavelength (λ), waveguide aperture size (D), and waveguide to object

[†](*Peer review*)C. F. Cull, D. A. Wikner, J. N. Mait, M. Mattheiss, and D. J. Brady, "Millimeter-wave compressive holography," Appl. Opt. (2010)

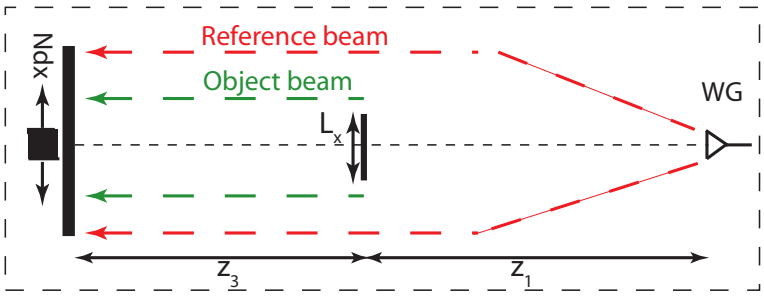

Figure 4.9: Optical schematic for millimeter-wave Gabor holography containing a waveguide (WG), object extent (L_x), detector plane sampling with number of pixels (N) and pixel pitch (dx), waveguide to object distance (z_1), and object to receiver distance (z_3).[†]

distance (z_1 in Fig. 4.9) such that $B = .89\lambda z/D$ [87]. Energy diffracted from the object interfered with a reference field at a receiver plane where N measurements were recorded with sampling pitch dx.

Our detector is an incoherent, single pixel receiver circuit shown in Fig. 4.10. Incident energy (at 94 GHz) at the receiver circuit was collected with a WR-08 open waveguide measuring 2.32 mm (W) $\times$ 1.02 mm (H). In the circuit, energy was mixed with a local oscillator (LO in Fig. 4.10) at 85 GHz and down converted to an intermediate frequency (IF in Fig. 4.10(b)) at 9 GHz. The IF signal was amplified twice with a low noise amplifier (LNA) and a MITEQ (8-12 GHz) amplifier. A band pass filter was applied to the signal before a voltage measurement was read from a Schottky diode detector. The band pass filter passes frequencies between 7-11 GHz thereby making the receiver spectrally sensitive over a bandwidth of 4 GHz.

The output of the diode is a DC voltage and measurements recorded with the

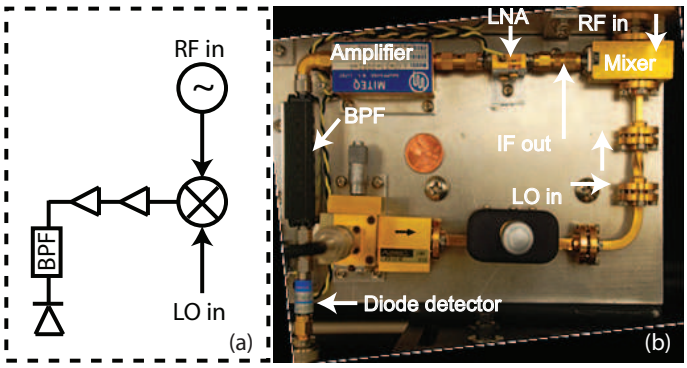

Figure 4.10: Superheterodyne receiver (a) circuit diagram and (b) experimental layout where incident energy (RF in) is mixed with a local oscillator (LO), down converted to an intermediate frequency (IF), amplified by both an LNA and a second amplifier, filtered with a band pass filter (BPF), and detected with a Schottky diode.[†]

receiver circuit confirmed that the system was operating in the linear region. The sensitivity of the receiver measured 48.31 mV/μW (see Appendix A.7 for the sensitivity plot). Also, there exists a DC offset in the receiver response due to the inherent circuit noise, as well as, the data acquisition system. This DC offset or mean noise value was calculated by recording 1000 measurements per pixel over a region of 60×60 pixels. The mean background/noise value is 15 mV. The standard deviation of the noise level about the mean (0.1472 mV) provides an indication for the circuit noise caused by the receiver. Also, while the mean signal value within the recorded composite hologram is object dependent, the mean signal value for the reference beam was greater than 20 times the mean background signal. Thus, the composite holograms were not limited by inherent circuit noise or background noise levels.

For real-time measurement, voltages from the receiver circuit were acquired using a National Instruments (NI) USB high-speed M series data acquisition module (USB-6251). A LabView GUI was used to automate the data collection process from the NI-DAQ module, as well as, to automate dual-axis ($x - y$) translation of the receiver circuit. For receiver translation, we used a step size sampling rate of 1000 samples per second. The sampling process involved scanning a step size of one-fifth of a 2.32 mm pixel pitch (step size of 73 motor steps) in the horizontal direction to more accurately acquire data using a raster-scan method. In the vertical direction, the step size equalled a 2.32 mm pixel pitch (step size of 365 motor steps). Further, 21 samples were averaged per step in both the horizontal and vertical directions. All holograms were recorded as a raster-scanned (x-y) 128 (H)×640 (W) images. The data acquisition time for a raster-scanned 128×640 pixel image took about 28 minutes.

4.5 Experiment results

Several Gabor holograms were recorded using the incoherent receiver circuit described above. The raster-scanned image was binned by five along the horizontal direction to generate a 128×128 pixel image. Each hologram is digitally recorded with 16 bit accuracy as specified by the DAQ module. In the post-detection process, the composite

hologram was reference beam subtracted, DC filtered in the spectrum of the hologram, and zero-padded to create a 168×168 pixel image. Zero-padding the system matrix helps to avoid circular convolution effects from the FFT operation used in the forward and adjoint models in the TV-minimization algorithm. In this section, two methods for 3D object reconstruction were compared: conventional backpropagation and TV-minimization. Recall that Fig. 4.3 in Section 4.3 depicted a squared-field term isolated at the $z = 0$ plane and twin-images located at object planes $z \leq 0$ using the TV-minimization algorithm. For simplicity, both the backpropagated and TV-minimization reconstructions were compared and evaluated at $z > 0$ planes.

Figure 4.11 illustrates three semi-transparent polymer objects analyzed in this section. Specific properties associated with the object polymer material have been addressed elsewhere [88]. These objects were made with an Eden 333 prototyping machine that lays thin layers of photopolymer and UV-cures each layer, building a 3D object slice by slice. A 5 mm thick sheet of the polymer material under test (see Fig. 4.11) was uniformly illuminated with 94 GHz energy. The material was found to attenuate the incident energy by less than 20%. In the experiment, the polymer objects were mounted to Styrofoam blocks (also semi-transparent in the MMW) or suspended with string. Test objects, in Fig. 4.11, include a model wrench with 2 in (W) $\times$ 6 in (H) spatial extent, a model dagger with .25 - .5 in (W) $\times$ 4 in (H)

Figure 4.11: Object scale of a semi-transparent polymer (a) wrench, (b) dagger, and (c) gun.†

spatial extent, and a model gun with .16 - 1 in (W) × 5 in (H) spatial extent. Combinations of these test objects were used in the experimental setup. Further, MMW RF absorber (ABS in Fig. 4.7(a) and Fig. 4.12(a)) was used to minimize stray reflected energy collected at the receiver.

Three separate experiments were conducted. In each experiment, the spatial extent of the 128×128 pixel hologram was 296.96 mm in both the horizontal and vertical dimensions. The holograms were zero-padded to 168 × 168 pixels. Zero-padding the hologram does not have any impact on reconstruction since diffracted object data does not exist in those regions. In the first experiment (see Fig. 4.7(a)), a hologram of a polymer model gun and model dagger was recorded. The objects were placed 22 mm and 107 mm away from the receiver platform as shown in Figure 4.13(a). Recall that the optical schematic for the hologram recording geometry is shown in Fig. 4.9. Using linear inversion, the holographic measurement was backpropagated to four different

z-planes as shown in Fig. 4.7(b). Linear backpropagation estimates the 3D electromagnetic object field at each z-plane, but out-of-focus diffracted energy present in all z-planes hinders object localization. In Fig. 4.7(c), however, TV-minimization results provide a means for localizing objects to their corresponding z-planes. Note that the baseline axial resolution metrics, derived in Section 4.2, suggest an axial resolution of approximately 20 mm for an object feature size of 4 mm. Figure 4.7(d-e) shows the pixel amplitude as a function of distance in z in 10 mm increments. These plots were generated at a finer resolution than the theoretical limit of 20 mm. Figure 4.7(d-e) shows the pixel amplitude at a central pixel (x,y) located at the barrel of the synthetic gun and at the blade edge of the synthetic dagger. The axial plots in Fig. 4.7(d-e) show that TV-minimization reconstructions fall short of the theoretical limit. While backpropagation results provide an estimate of the object field along the axial plane, TV-minimization enables object localization that is consistent with the spatial extent of the object. The experimental axial resolution with the gun and dagger experiment is approximately 30 mm. Errors are attributed to the residual diffracted energy (out-of-focus energy) found in neighboring z-planes for the TV-minimization results. The measurement error can be minimized by acquiring a larger number of measurements (> 128 pixels).

In a second experiment, a semi-transparent polymer wrench, gun, and dagger were

placed at three different distances away from the receiver (see Fig. 4.12(a)). These distances were 48 mm, 155 mm, and 205 mm. The recorded digital hologram of the three objects is shown in Fig. 4.13(b). A higher background signal, compared to the previous experiment, is attributed to an increase in illumination source power. The 3D object is estimated using linear backpropagation and TV-minimization. Object estimates were reconstructed at four separate z-planes as depicted in Fig. 4.12(b-c). Linear backpropagation estimates reveal object field distributions in each z-plane and limited object localization while TV-minimization estimates show a reduction in out-of-focus contributions from twin-images. Amplitude data from a single spatial location in each object is plotted in increments of 5 mm along the axial plane in Fig.4.12(d-f). Object localization using TV-minimization is shown in Fig. 4.12(d-f), while backpropagation field estimates do not provide any axial resolution. Still, the theoretical measure for a 4 mm feature size on the polymer gun object should enable 20 mm axial resolution. Axial plots from TV-minimization reconstruction in Fig. 4.12(d-e) show an axial resolution of approximately 30 mm. Capturing more measurements with the receiver circuit would further improve TV estimation of the 3D object.

Lastly, the impact of sparse holographic measurements was analyzed with real data. Sampling matrices, shown in Fig. 4.4, were applied to experimental mea-

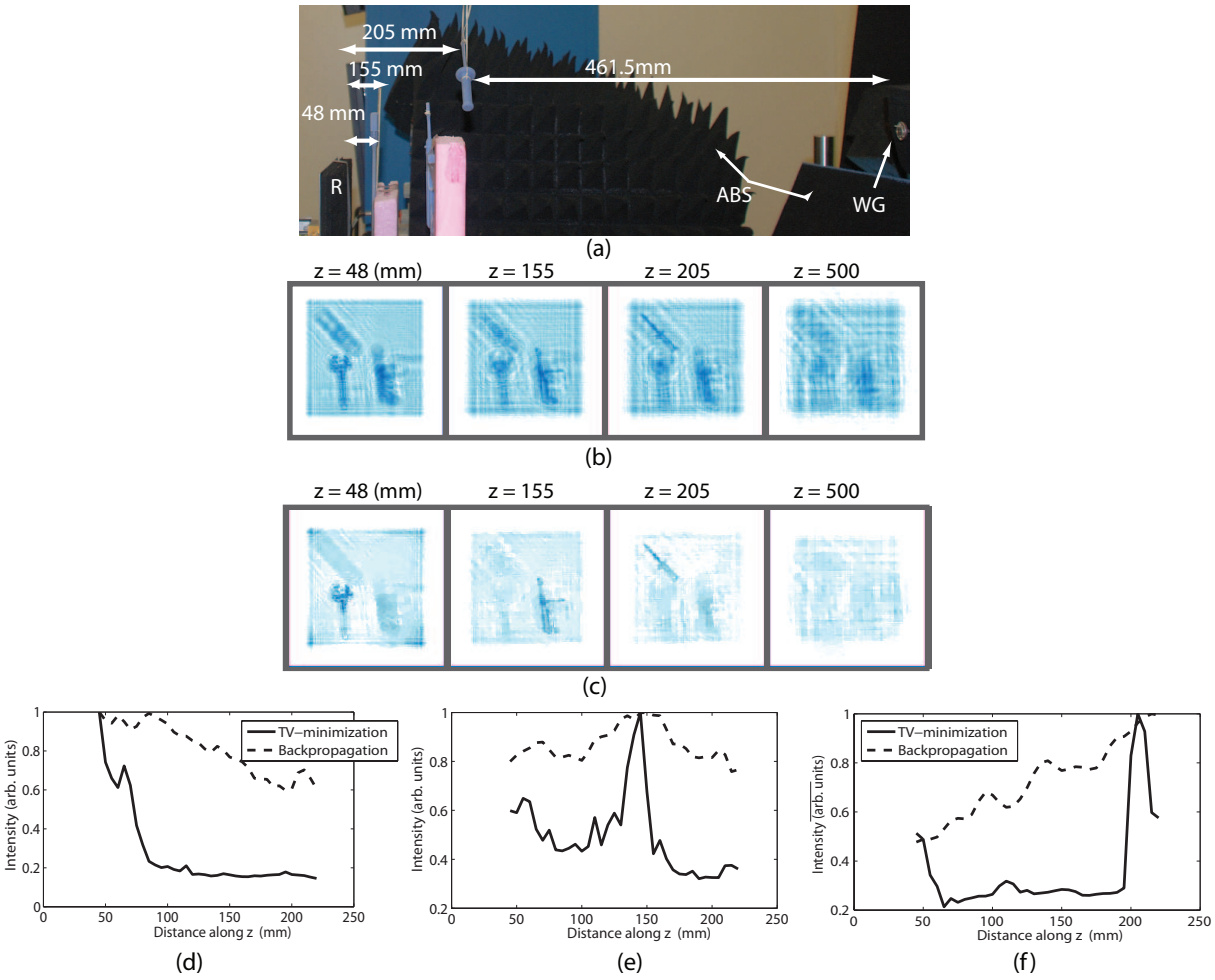

Figure 4.12: Experiment with a polymer model wrench, gun, and dagger placed at three different distances along the axial plane.(a) Photograph of the experiment. Transverse slices in four different z-planes of the (b) backpropagated and (c) TV-minimization reconstructions. Amplitude pixel (x,y) as a function of z, in 5 mm increments, where TV-minimization reconstructions and backpropagation estimates for a center point on the (d) wrench, (e) gun, and (f) dagger are plotted.[†]

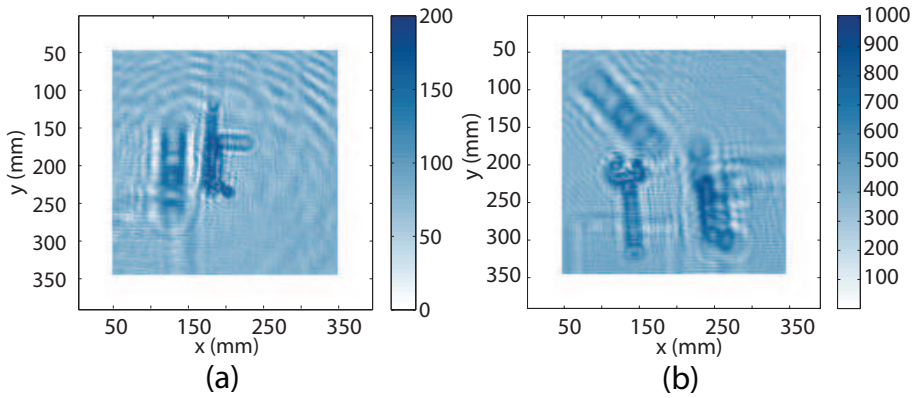

Figure 4.13: Experimental holographic recording of (a) a model dagger and a model gun and (c) a model dagger, a model gun, and a model wrench located in different z-planes.[†]

surements. Since holographic measurements (128×128 pixels) were zero-padded to a spatial extent of 168×168 pixels, each 128×128 transmittance function was zero-padded to the measurement data size. Figure 4.14 shows backpropagation and TV-minimization results for sparse holographic measurement. For backpropagation estimates, absolute zero values in the detector measurement due to the subsampling matrix were substituted with interpolated values calculated from measurements at neighboring pixels. Similar to synthetic gun and dagger simulations in Section 4.2, experimental data showed adequate spatial resolution and object localization along the axial plane when 54.68% of the measurement data was removed. This was feasible when a gradient sparsity constraint was used. Again, pixel amplitude versus distance in z plots were generated in increments of 10 mm along the axial plane. Measurement reduction by 3.9% and 54.68% does not seem to impact object local-

ization using TV-minimization. However, simulation and experimental results reveal a sacrifice in spatial resolution using backpropagation and TV-minimization with a 54.68% measurement reduction.

In summary, this section discussed three experiments where objects were placed along the z-axis at either two or three different planes. While data acquisition times were long (e.g. $<$ 30 minutes), 3D object estimation and improved object localization along the axial plane is made possible with TV-minimization. Linear backpropagation accurately estimates the object field along the axial plane, however, out-of-focus diffracted fields hinder object localization. Sparse measurement impacts object spatial resolution using linear backpropagation since object field reconstruction is challenging. TV-minimization results improve upon a linear backpropagation method where a twin-image term and a squared-field term affect object reconstruction. Sparse measurement reconstructions in simulation and with experimental data demonstrated that reconstructed object quality is maintained with fewer measurements. Also, sparse measurement reconstruction with experimental data further motivated the potential for decreasing data acquisition times using fewer scans.

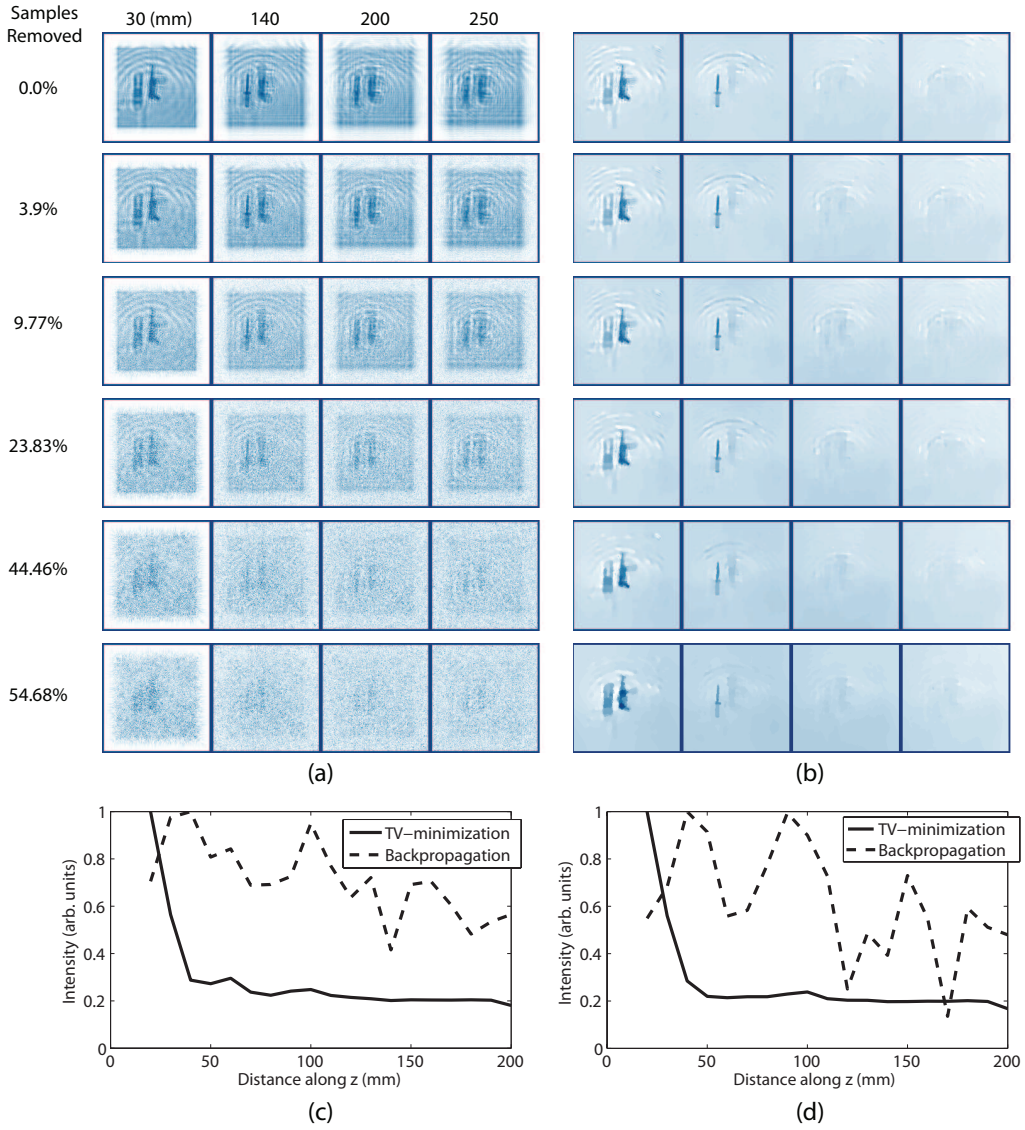

Figure 4.14: Sparse measurement reconstruction of experimental data using (a) linear backpropagation and (b) TV-minimization for 3D object estimation. Amplitude of a central pixel (x,y) on the blade edge of the dagger as a function of z, plotted in 10 nm increments, from (c) 3.9% holographic measurement removal and (d) 54.68% holographic measurement removal.[†]

4.6 Summary and Conclusion

An improved method for 3D tomographic estimation from 2D holographic measurements has been presented. Linear backpropagation estimation of a 3D object is hindered by a squared-field term and a twin-image term in reconstruction. TV-minimization of 2D holographically recorded data shows suppression of these out-of-focus terms. Our nonlinear inversion scheme exploits object sparsity in the gradient domain. Further, simulations and experimental data reconstructions show that randomly sampled 2D holographic measurements enable 3D object estimation even when 54.68% of the measurements have been removed. However, there is a degradation in spatial resolution. PSNR values in simulation decrease when holographic measurements are removed. Also, a sparse measurement scheme for adequate 3D object estimation is object dependent. Successful 3D object estimation from 2D holographic measurements using TV-minimization depends on the object feature size (Δx_o), which translates into the recorded hologram spatial extent.

This chapter has focused on the analysis of semi-transparent objects at millimeter wavelengths. In practice, objects of interest are not semi-transparent. Thus, a reflection geometry may be better-suited in a practical implementation. Data inversion techniques discussed in this chapter are applicable to a reflection geometry. The reflection case is more challenging as speckle impacts holographic measurement.

Also, since gradient-imposed sparsity is object dependent, a thorough object study on resolution for both transmissive and reflection cases still needs to be undertaken.

Chapter 5

Conclusions and discussion

This dissertation has explored three different devices : SmacM, (DD)CASSI, and a MMW holography platform. These devices were related to research efforts that included pushbroom imaging for transmissive target analysis and fluorescence microscopy, snapshot spectral imaging for fluorescence microscopy, and compressive holography for eventual remote concealed weapons detection.

Chapter 2 discussed the system model, system design, and a coded aperture spectrometer interface to an upright microscope for transmissive and fluorescent target analysis. System simulations were used to study the impact of spectrally narrow and broad objects on NNLS spectral estimation. The CAS pushbroom imager provided optimized spatial resolution compared to a previous generation system and 1 nm spectral resolution. Fluorescence microscopy of microspheres and cells were analyzed with SmacM. The main drawback, depending on the target application (i.e static or dynamic sample analysis), was scan time. Scan times with SmacM were dominated by the detector integration time. Studies evaluating scan time limitations could be undertaken to maximize system performance for analyzing fluorescent biological

samples.

Chapter 3 discussed a snapshot spectral imager, CASSI, that overcame the limitations of a scanning system at the expense of spatial and spectral resolution. CASSI's spatial and spectral resolution were limited by the aperture-code feature size. The instrument's spectral resolution measured 10 nm. Two algorithms for 3D object estimation were implemented in simulation and evaluated with real data. Static and dynamic fluorescent samples were tested with CASSI. An optical system re-design was discussed to create a more compact and off-the-shelf system. The progression for this work would involve realizing the CASSI re-design for increased stability and ease of comparison to other multi-spectral testbeds. Also, realizing spectral analysis of dynamic biological samples would be interesting and beneficial to the cell biology community since current systems are costly. Finally, as CCDs advance and detector pixels decrease in size a more efficient aperture-code could be realized in CASSI to improve spatial and spectral resolution.

Chapter 4 presented a MMW holography platform, the system model, and a TV-minimization algorithm used for 3D tomographic object estimation from a single 2D holographic composite and a 2D sparse holographic composite. Various sampling strategies were investigated in an attempt to reduce data acquisition time versus the traditional raster scan method of creating an image composite. Sampling strategies

were evaluated in simulation to study the impact on reconstruction efficacy. Real measurements were also analyzed with each sampling scheme. In the experimental setup, semi-transparent and polymer objects placed at various positions along the axial plane and were successfully reconstructed. The progression of this work involves a change in the sampling geometry to extend millimeter-wave object reconstruction to metallic object analysis. Simulations with a reflection geometry could motivate experiments in this configuration. A reflection geometry would enable the analysis of metallic objects, while introducing a speckle phenomenon. Wideband illumination, structured illumination, or statistical analysis would be required to minimize the speckle contribution. While this project considered an off-axis geometry as well, a space-bandwidth product limit prevented successful object reconstruction and increased the number of measurements required for successful object estimation. This approach could also be revisited. Finally, the study of MMW holography for remote concealed weapons detection motivates the realization of a platform for use in the field. Therefore, measurement strategies discussed in this dissertation would need to be successfully tested and expanded upon for actual system implementation.

Appendix A

Appendix

A.1 Derivation of angular, linear dispersion, and spectral resolution

Derivation of linear dispersion, ξ, begins with the grating equation:

$$\sin(\theta_I) + \sin(\theta_R) = \frac{\kappa\lambda}{\Lambda}, \tag{A.1}$$

where θ_I represents the incident angle onto the grating, θ_R represents the refracted angle from the grating, κ represents the grating diffraction order, and Λ represents the reciprocal grating period. If it is assumed that $\theta_I = 0$, the angular dispersion $(\delta\theta/\delta\lambda)$ is found by taking the partial derivative with respect to θ_R and λ as shown below.

$$\frac{\delta\theta_R}{\delta\lambda} = \left(\frac{\delta}{\delta\theta_R}\right)^{-1}\frac{\delta}{\delta\lambda} \tag{A.2}$$

$$\frac{\delta}{\delta\theta_R} = \cos(\theta_R)$$

$$\frac{\delta}{\delta\lambda} = \frac{\kappa}{\Lambda}.$$

Angular dispersion is defined as

$$\frac{\delta\theta_R}{\delta\lambda} = \frac{\kappa}{\Lambda\cos(\theta_R)}. \tag{A.3}$$

Linear dispersion, ξ, is calculated by multiplying angular dispersion by the optical system back focal length (F) as denoted by

$$\begin{aligned}\frac{\delta x}{\delta\lambda} &= \frac{\delta\theta_R}{\delta\lambda}F \\ &= \frac{\kappa F}{\Lambda\cos(\theta_R)}.\end{aligned} \tag{A.4}$$

Also, spectral resolution is easily derived by multiplying the reciprocal linear dispersion in Eq. A.4 by the root-mean-squared (RMS) spatial resolution limit of the spectrometer. In the case of the CAS, the mask feature size typically dominates in the RMS spatial resolution calculation. The empirical system calculation for linear dispersion involves dividing the dispersion spatial extent along the x-axis of the detector plane by the spectral range ($\Delta\lambda$) of the spectrometer. Experimental spectral resolution is then derived as previously described.

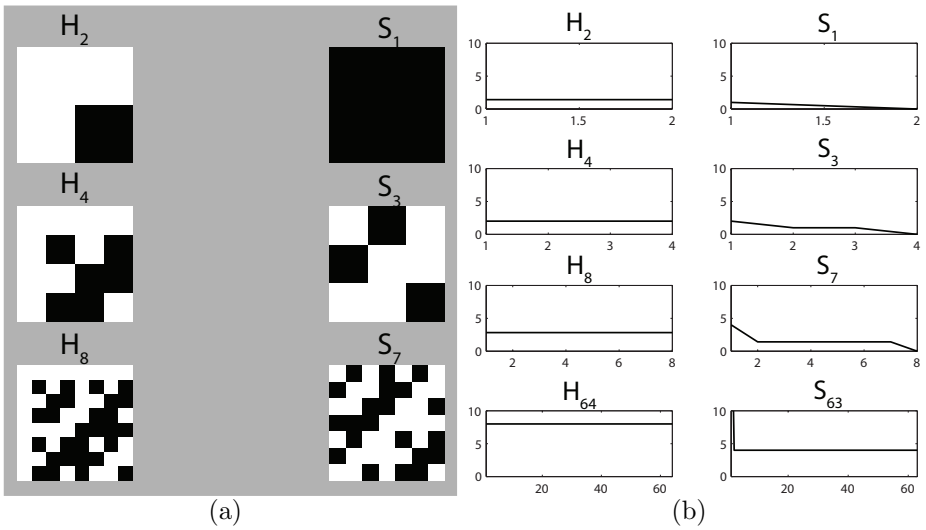

Figure A.1: (a) Hadamard (H_A) and S-matrices (S_A) of different orders. (b) Singular value spectrum.

A.2 Hadamard and S-matrices

The Hadamard matrix is a well-conditioned, invertible matrix. The first order Hadamard matrix is defined as $\mathrm{H}_{A=1} = [1]$. The partitioned matrix

$$\begin{bmatrix} H & H \\ H & -H \end{bmatrix}, \tag{A.5}$$

is used to find Hadamard matrices of higher orders. Each H_A is a normalized Hadamard matrix of order A. To generate an S-matrix from a Hadamard matrix, the first row and first column of the Hadamard matrix are removed and values equal to +1 are changed to 0 and values equal to -1 are changed to 1 [89]. Hadamard and S-matrices are shown in Fig. A.1(a). Further, singular value decomposition (SVD)

is used to characterize system matrix performance for Hadamard or S-matrix-based coded aperture spectrometers. The SVD can be used to determine the rank of a matrix by counting the number of nonzero singular values. Also, the condition number of the matrix is found by plotting the singular vectors returned from the SVD and taking the ratio between the maximum singular value to the minimum singular value. The condition number found provides a measure for system sensitivity to noise in the measured data. Singular value plots are shown in Fig. A.1(b) for different order Hadamard and S matrices. Note that a flat singular value spectrum is indicative of a well-conditioned matrix, or a system matrix less sensitive to noise.

A.3 Pseudo-inverse TV-minimization for 3D data cube estimation

In Chapter 3 of this dissertation, two algorithms were discussed for 3D (x, y, λ) data recovery from 2D detector measurements using a nonlinear iterative TV-minimization algorithm. Another adaptation to the TV-minimization algorithm consists of incorporating the pseudo-inverse into the system matrix. This approach provides a better conditioned system matrix (see Fig. A.3(c)). This method would enable adequate comparison between an RGB image inverted for 3D data cube estimation and a CASSI image inverted using a pseudo-inverse TV-minimization. Both meth-

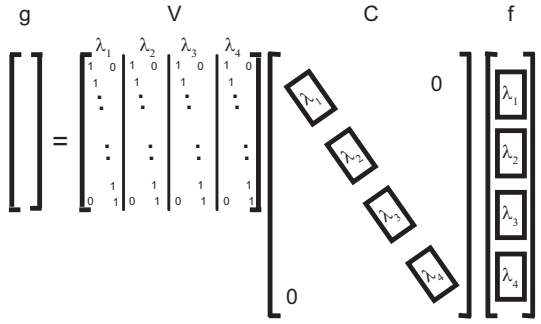

Figure A.2: CASSI system model where the transformation matrix (H) is represented by a summation matrix (V) and a calibration cube matrix (C) from a CASSI system measuring four spectral channels

ods would employ a pseudo-inverse in the data estimation process. This section addresses, in simulation, CASSI data inversion by incorporating the pseudo-inverse into the system matrix for TV-minimization.

Recall from Chapter 3 that the dual-disperser CASSI system model employs a transformation matrix (H) that is modeled as a summation matrix (V) and a calibration cube matrix (C). The matrix structure for the system model is shown in Fig. A.2. The summation matrix (V) is a block diagonal matrix of ones and the calibration cube matrix (C) is a diagonal matrix with shifted mask modulated images that are vectorized and placed along the diagonal of the calibration matrix. For this simulation exercise, a 40×40 detector image is generated and the baseline f data cube measures 40×40×10. The CASSI forward model is generated using

$$g = VCf, \tag{A.6}$$

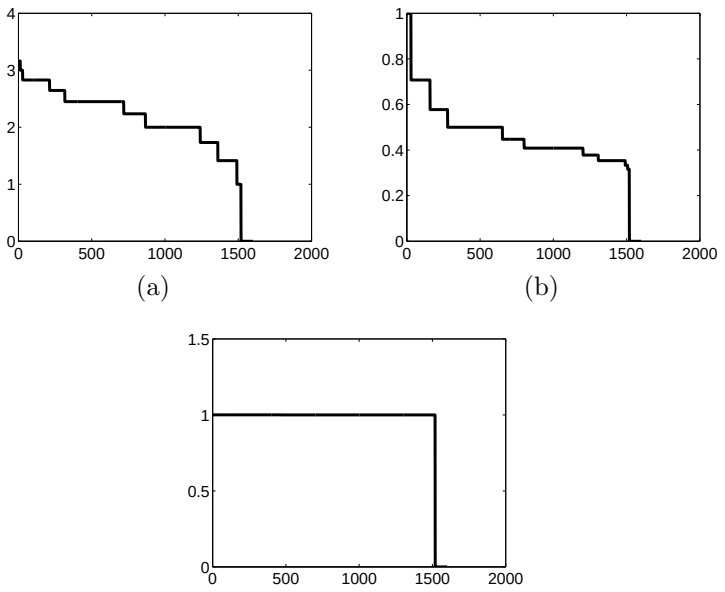

Figure A.3: (a) Singular values plot for the transformation matrix, H.(b) Singular values plot for H^+.(c) Singular values plot for the H^+H matrix

where g is a 1600×1 vectorized detector measurement, V is a 1600×16000 matrix, and C is a calibration matrix of size 16000×16000. To evaluate the behavior of the linear system model, a singular value decomposition (SVD) is taken of the system matrix, H. A plot of the singular values provides a means for generating the condition number of the system matrix. A flat spectrum indicates a condition number equal to one. The singular value plot for H is shown in Fig. A.3(a). The singular value spectrum for H is not as ideally conditioned. An attempt to improve the condition number is made by replacing the H matrix with a pseudo-inverse. The pseudo-inverse for H is expressed as

$$H^+ = (H^\dagger H)^{-1} H^\dagger, \tag{A.7}$$

where $H^{\dagger}$ represents the Hermitian transpose operator. The singular value spectrum for H^{+} is shown in Fig. A.3(b). The H^{+} transformation yields a condition number of approximately three. The pseudo-inverse is implemented by the MATLAB 'pinv' command which uses an SVD approach to Tikhnov regularization to solve for the inverse of an ill-conditioned matrix. To improve the condition number of the system matrix, the pseudo-inverse matrix (H^{+}) was multiplied by the H matrix and an SVD singular value spectrum plot was generated. The singular value plot for $H^{+}H$ is shown in Fig. A.3(c).

$$\mathbb{B} = H^{+}H \tag{A.8}$$

Matrix $\mathbb{B}$ in Eq. A.8 provides a better conditioned system matrix (i.e. condition number of one).

Using the new system matrix ($\mathbb{B}$) the forward and transpose models in Eq. A.6 can be reformulated. The CASSI forward model incorporating the matrix $\mathbb{B}$ is modeled as

$$g = \mathbb{B}^{T} f, \tag{A.9}$$

where $\mathbb{B}^{T}$ represents the transpose of the matrix. Also, the new CASSI transpose model is

$$f = \mathbb{B} g \tag{A.10}$$

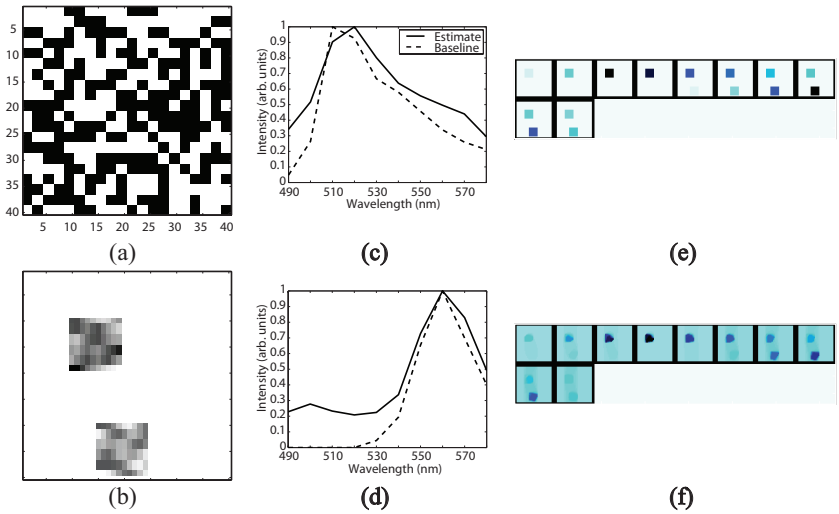

Figure A.4: (a) Simulated 40×40 pixel aperture-code. (b) Simulated 15×15 pixel fluorescent squares in a 40×40 detector image. Baseline and pseudo-inverse adapted TV-minimization spectral estimates at a single spatial locations from each 15×15 pixel square for the (c) yellow-green and (d) orange spectral signature. (e) Baseline f data cube of 15×15 pixel squares. (f) Pseudo-inverse TV-minimization f^* data cube estimate.

Results from the pseudo-inverse adaptation to the TV-minimization algorithm are shown in Fig. A.4. A simulated 3D f data cube was generated by creating a 40×40 pixel scene containing two 15×15 pixel squares spectrally modeled after the baseline spectra shown in Fig. A.4(c-d). The spectral signatures were downsampled to match the resolution of the simulation system. The calibration cube was generated by simulating a shifted 40×40 pixel aperture-code shown in Fig. A.4(a). The simulated system model measured 10 spectral channels spanning the spectral range between 490 nm and 580 nm with 10 nm spectral resolution. The number of spectral channels and the image size were constrained by the computational power used to generate the system matrix. Figure A.4(e-f) shows the baseline f data cube and the f^* data

cube estimate generated from the pseudo-inverse method described in this section. The measured PSNR is 14.773. While the PSNR needs improvement, the amplitude spectral plots of the baseline spectra and the reconstructed spectra in Fig. A.4(c-d) are very similar in shape. The pseudo-inverse implementation is impractical for real data analysis where an f data cube size is typically $100 \times 100 \times 32$ or larger since generating the forward and transpose system matrices incur a large computational cost. For this reason, the implementation was not used with experimental data.

A.4 Full-field CASSI illumination fiber coupled setup

In Chapter 3, Section "Calibration procedure and algorithm implementation", a calibration cube was acquired via full-field monochromatic illumination of CASSI. Full-field illumination was achieved with a fiber interface between the monochromator and CASSI. A high NA fiber was used to fully illuminate the CASSI input aperture with monochromatic light. Due to the high NA of the fiber, a lens combination was coupled to the fiber output. The lens combination output was modeled after the image space NA generated from a microscope objective used in the data acquisition process of fluorescent targets. Note that the object space NA of CASSI was modeled after the image space NA from a 20×, 0.8 NA objective, this image space NA was used to model the lens combination. Direct illumination of CASSI with the high NA fiber

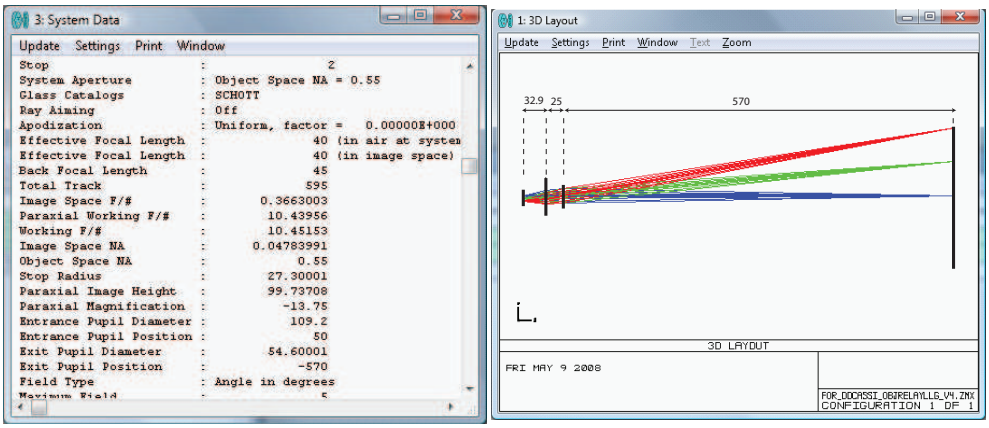

(a) (b)

Figure A.5: (a) *Zemax* system prescription data for the optical setup used for CASSI calibration data acquisition. (b) (distance units in mm) *Zemax* 3D optical layout for object space NA matching and full-field illumination of CASSI.

would cause unwanted stray light reflections to appear in each of the monochromatic frames recorded with CASSI and used in the TV-minimization algorithm.

The experimental optical setup consisted of a high NA fiber and two lenses. The lens combination was used to reimage the light from the high NA fiber from the monochromator to the CASSI input aperture. The CASSI object plane NA is 0.04 and the fiber output NA is 0.55. The lens combination object space NA is 0.55 and the image space NA was optimized to a 0.04 NA to match the CASSI object space NA. Figure A.5(b) shows the lens combination. The lenses in the optical setup were modeled as ideal paraxial surfaces of different effective focal lengths (EFL) found in the lab. An initial design was created on paper and then optimized in *Zemax*. First, the thin lens equation was used to calculate the image distance and the EFL was calculated. For *Zemax* optimization, the object and image distances

were set as variable and the image space NA was optimized. The results are shown in Fig. A.5(a), where the image space NA approximately matches the CASSI object space NA (0.04). Theoretical calculations for a thin lens pair ($f_1 = 50$ mm and $f_2 = 100$), yield an EFL of approximately 33 mm.

$$f_{EFL} = \frac{f_1 f_2}{f_1 + f_2} \tag{A.11}$$

The *Zemax* EFL is 40 mm with the optimized lens system. The distance between the paraxial surfaces was found by manipulating

$$f_{EFL} = \frac{f_1(L_d - f_1)}{L_d - (f_1 + f_2}, \tag{A.12}$$

and solving for the distance between the two paraxial surfaces in the lens system, L_d. The theoretical distance, L_d, is 20 mm and the *Zemax* distance was set to 25 mm. The image distance for the thin lens pair was optimized in *Zemax*. Overall, the lens system provided a method for decreasing the NA captured by the fiber to match the object space NA of CASSI. This helped to minimize vignetting or unwanted reflections in acquiring the calibration cube.

A.5 Millimeter-wave compressive holography forward and adjoint model matrices

Recall from Chapter 4 that the forward model for Gabor holography is

$$g = F_{2D}^{-1} Q F_{2D} f. \tag{A.13}$$

The forward model matrix implementation for two object depths and single wavelength illumination is

$$g = \begin{bmatrix} F_{2D}^{-1} \end{bmatrix} \begin{bmatrix} Q_{z_1} & Q_{z_2} \end{bmatrix} \begin{bmatrix} F_{2D} & \\ & F_{2D} \end{bmatrix} \begin{bmatrix} f_{z_1} \\ f_{z_2} \end{bmatrix}. \tag{A.14}$$

Also, recall that the adjoint model is

$$f = F_{2D}^{\dagger} Q^{\dagger} \left[F_{2D}^{-1} \right]^{\dagger} g, \tag{A.15}$$

where $\dagger$ represents the Hermitian transpose. Since the Fourier matrix is a unitary matrix, the adjoint and inverse of the Fourier matrix are equivalent. The adjoint system model matrix implementation for two object depths and single wavelength

illumination is represented as

$$\begin{bmatrix} f_{z_1} \\ f_{z_2} \end{bmatrix} = \begin{bmatrix} F_{2D} & \\ & F_{2D} \end{bmatrix} \begin{bmatrix} Q_{z_1} \\ Q_{z_2} \end{bmatrix} \begin{bmatrix} F_{2D}^{-1} \end{bmatrix} \begin{bmatrix} g \end{bmatrix}. \tag{A.16}$$

Further, Chapter 4 explored a subsampling holographic measurement that incorporated a sampling window into the forward and adjoint models. The new forward and adjoint models were denoted by

$$g = W F_{2D}^{-1} Q F_{2D} f \tag{A.17}$$

$$f = F_{2D}^{\dagger} Q^{\dagger} \left[F_{2D}^{-1}\right]^{\dagger} W^{\dagger}. \tag{A.18}$$

The matrix implementation of the corresponding forward and adjoint models is given by:

$$\begin{bmatrix} g \end{bmatrix} = \begin{bmatrix} W \end{bmatrix} \begin{bmatrix} F_{2D}^{-1} \end{bmatrix} \begin{bmatrix} Q_{z_1} & Q_{z_2} \end{bmatrix} \begin{bmatrix} F_{2D} & \\ & F_{2D} \end{bmatrix} \begin{bmatrix} f_{z_1} \\ f_{z_2} \end{bmatrix} \tag{A.19}$$

and

$$\begin{bmatrix} f_{z_1} \\ f_{z_2} \end{bmatrix} = \begin{bmatrix} F_{2D} & \\ & F_{2D} \end{bmatrix} \begin{bmatrix} Q_{z_1} \\ Q_{z_2} \end{bmatrix} \begin{bmatrix} F_{2D}^{-1} \end{bmatrix} \begin{bmatrix} W^{\dagger} \end{bmatrix} \begin{bmatrix} g \end{bmatrix} \tag{A.20}$$

The adaptation of the subsampled forward and adjoint models for multi-wavelength illumination considering two object depths and three wavelengths is denoted by

$$\begin{bmatrix} g_{\lambda_1} \\ g_{\lambda_2} \\ g_{\lambda_3} \end{bmatrix} = \begin{bmatrix} W & & \\ & W & \\ & & W \end{bmatrix} \begin{bmatrix} F_{2D}^{-1} & & \\ & F_{2D}^{-1} & \\ & & F_{2D}^{-1} \end{bmatrix} \begin{bmatrix} Q_{z_1\lambda_1} & Q_{z_2\lambda_1} \\ Q_{z_1\lambda_2} & Q_{z_2\lambda_2} \\ Q_{z_1\lambda_3} & Q_{z_2\lambda_3} \end{bmatrix} \begin{bmatrix} F_{2D} & \\ & F_{2D} \end{bmatrix} \begin{bmatrix} f_{z_1} \\ f_{z_2} \end{bmatrix} \tag{A.21}$$

and

$$\begin{bmatrix} f_{z_1} \\ f_{z_2} \end{bmatrix} = \begin{bmatrix} F_{2D} & \\ & F_{2D} \end{bmatrix} \begin{bmatrix} Q_{z_1\lambda_1} & Q_{z_1\lambda_2} & Q_{z_1\lambda_3} \\ Q_{z_2\lambda_1} & Q_{z_2\lambda_2} & Q_{z_2\lambda_3} \end{bmatrix} \begin{bmatrix} F_{2D}^{-1} & & \\ & F_{2D}^{-1} & \\ & & F_{2D}^{-1} \end{bmatrix} \begin{bmatrix} W^{\dagger} & & \\ & W^{\dagger} & \\ & & W^{\dagger} \end{bmatrix} \begin{bmatrix} g_{\lambda_1} \\ g_{\lambda_2} \\ g_{\lambda_3} \end{bmatrix} \tag{A.22}$$

Further, the system matrix or sensing matrix defined in Eq. A.13, $H = \mathbb{F}^{-1}Q\mathbb{F}$, can be analyzed from a compressive sensing viewpoint. In general, the efficacy of a CS sensing matrix, $H = \Phi$, is predicated upon incoherence. The mutual coherence metric, $\mu(\Phi)$, [8, 90] is defined as

$$\mu(\Phi) = \max_{i \neq j, 1 \geq i,j \leq N} \left\{ \frac{\mid \phi_i^T \phi_j \mid}{\|\phi_i\| \|\phi_j\|} \right\}, \tag{A.23}$$

where ϕ_i represents the i^{th} column in the sensing matrix Φ. The mutual coherence can also be calculated from the maximum non-diagonal entry of the Gram matrix,

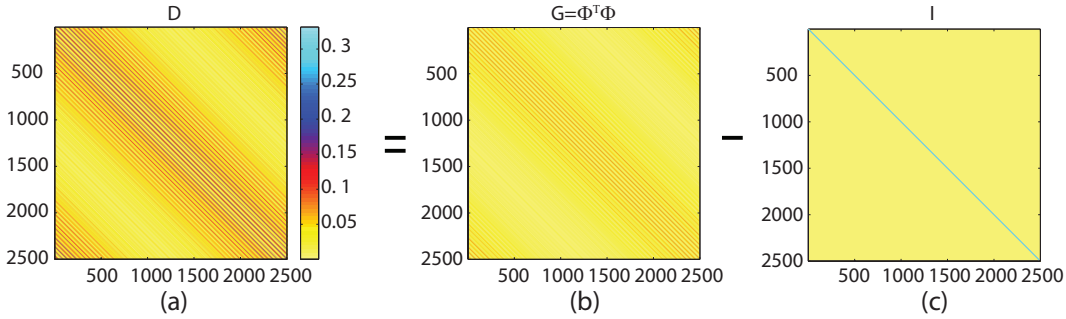

G = $\Phi^T\Phi$, when the columns of Φ are normalized. In general, if the Φ matrix is orthonormal (i.e. vectors of the matrix are of unit length and dot product between columns is zero), the mutual coherence is equal to zero. CS theory indicates that a low mutual coherence is suggestive of a better sensing matrix. In this exercise, the DFT matrix, Green's function (i.e. quadratic phase matrix, Q in Eq. A.13 and in Chapter 4), and the inverse or transpose DFT matrix were generated. The Gram matrix (G) is represented as

$$G = \Phi^T\Phi \tag{A.24}$$

$$= (\mathbb{F}_{2D}^{-1}Q\mathbb{F}_{2D})^{\dagger}(\mathbb{F}_{2D}^{-1}Q\mathbb{F}_{2D}),$$

and is shown in Fig. A.5(b). To compute the mutual coherence (μ), a new matrix D is generated by subtracting the Gram matrix (G) from an identity (I) matrix of the

same size so that the maximum of the non-diagonal entry can be found.

$$D = G - I \tag{A.25}$$

$$\mu = \max(D) \tag{A.26}$$

The steps in Eq. A.24 and Eq. A.26 are pictorially shown in Fig. A.5. The mutual coherence calculated for the millimeter-wave holography system matrix H was 0.3.

A.6 Millimeter-wave holography InP Gunn source characteristics

For the millimeter-wave holography project, a tunable (88 - 99 GHz) InP Gunn oscillator served as a reference beam and object illumination source. The center frequency of the Gunn oscillator operated at 94 GHz and the spectral linewidth plot from the manufacturer is shown in Fig. A.6(a). Since the oscillator could be frequency tuned, a micrometer reading and output power as a function of frequency plot is shown in Fig. A.6. For all holography experiments, a spectrum analyzer was used to monitor the spectral linewidth, detected frequency, and peak power. A sample measurement from the spectrum analyzer is shown in Fig. A.6(c).Time had to be allocated to frequency stabilize the source since it initially entered a multi-frequency mode.

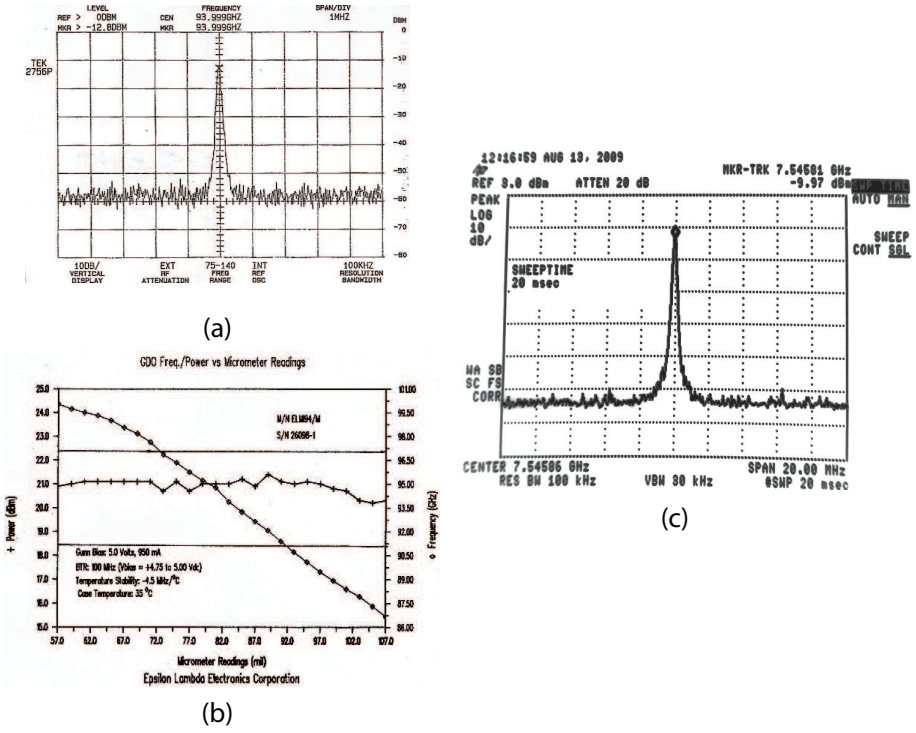

Figure A.6: (a) *Epsilon Lambda* spectral linewidth plot of a tunable W-band InP Gunn diode at a 94 GHz central frequency. (b) Data sheet for the InP Gunn diode oscillator with a maximum output power at 20 dBm (100 mW). Power output as a function of micrometer reading. (c) Spectrum analyzer reading from the superheterodyne receiver circuit at a single frequency (94 GHz before heterodyne detection) of 7.55 GHz. Power reading measures .10 mW at the detector and greater than 25 mW at the output to the waveguide after 6 dB attenuation.

A.7 Millimeter-wave holography: superheterodyne receiver sensitivity calculation

To calculate the sensitivity of the receiver circuit, a different single frequency 95 GHz Gunn oscillator, attenuator, and the superheterodyne receiver circuit were connected with minimal waveguide to reduce errors associated with the sensitivity measurement for the receiver circuit. The Gunn source illuminated the receiver circuit at full power and was attenuated by a range of values (40 - 45 dB). For this measurement, the 0 dB point and the 3 dB (half-power) point can be used to measure the sensitivity of the receiver. More data points increase the accuracy of the detector sensitivity calculation. At each data point, the illumination input power and the receiver voltage were measured. A summary of the data points are shown in Fig. A.7. The receiver sensitivity is measured as the slope of the line fit to the data points (48.31 $mV/\mu W$).

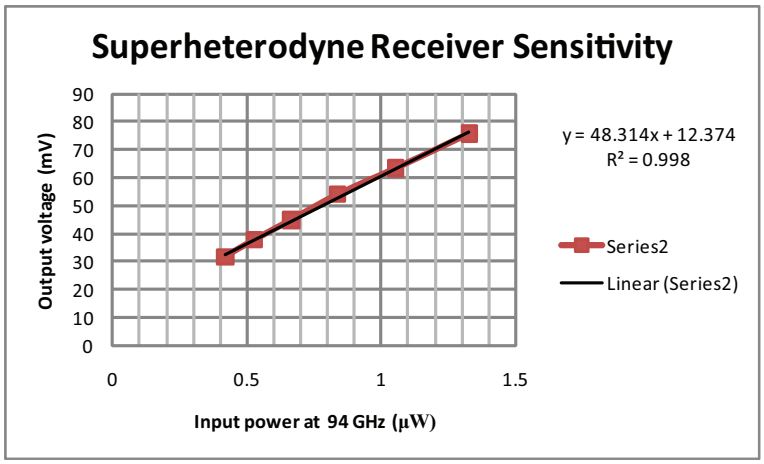

Figure A.7: Receiver output voltage versus input power at 94 GHz.

Bibliography

[1] B. Guenther, *Modern Optics*. Wiley -VCH, 1990.

[2] D. J. Brady, *Optical Imaging and Spectroscopy*. John Wiley & Sons, OSA, 2009.

[3] M. V. Smirnov, "Holographic approach to embedding hidden watermarks in a photographic image," *J. Opt. Technol.*, vol. 72, no. 6, pp. 464–468, 2005.

[4] G. Bub, M. Tecza, M. Helmes, P. Lee, and P. Kohl, "Temporal pixel multiplexing for simulateous high-speed, high resolution imaging," *Nature Methods*, vol. 7, pp. 207–211, 2010.

[5] C. E. Shanon, "Communication in the presence of noise," *Proceedings of the IEEE*, vol. 72, pp. 1192 – 1201, Sept. 1984.

[6] E. Candes, J. Romberg, and T. Tao, "Robust uncertainty principles: exact signal reconstruction from highly incomplete frequency information," *Information Theory, IEEE Transactions on*, vol. 52, pp. 489 – 509, feb. 2006.

[7] R. Baraniuk, "Compressive sensing [lecture notes]," *Signal Processing Magazine, IEEE*, vol. 24, pp. 118 –121, july 2007.

[8] E. Candes and J. Romberg, "Sparisty and incoherence in compressive sampling," *Inverse Problems*, vol. 23, no. 3, pp. 969–985, 2007.

[9] D. Donoho, M. Vetterli, R. DeVore, and I. Daubechies, "Data compression and harmonic analysis," *Information Theory, IEEE Transactions on*, 1998.

[10] E. Candes and M. Wakin, "An introduction to compressive sampling," *Signal Processing Magazine, IEEE*, 2008.

[11] E. Candes, "Compressive sampling," *Proceedings of the International Congress of Mathematicians*, 2006.

[12] M. E. Gehm, S. T. McCain, N. P. Pitsianis, D. J. Brady, P. Potuluri, and M. E. Sullivan, "Static two-dimensional aperture coding for multimodal, multiplex spectroscopy," *Appl. Opt.*, vol. 45, no. 13, pp. 2965–2974, 2006.

[13] M. Duarte, M. Davenport, D. Takhar, J. Laska, T. Sun, K. Kelly, and R. Baraniuk, "Single-pixel imaging via compressive sampling," *Signal Processing Magazine, IEEE*, 2008.

[14] A. F. Goetz, G. Vane, J. E. Solomon, and B. N. Rock, "Imaging Spectrometry for Earth Remote Sensing," *Science*, vol. 228, no. 4704, pp. 1147–1153, 1985.

[15] U. Schnars and W. Juptner, *Digital Holography, Digital Hologram Recording, Numerical Reconstruction and Related techniques*. New York: Springer-Verlag, 2005.

[16] A. Abubaker and P. Van Den Berg, "Total variation as a multiplicative constraint for solving inverse problems," *Image Processing, IEEE Transactions on*, vol. 10, no. 9, pp. 1384 –1392, 2001.

[17] P. Guo and A. Devaney, "Comparison of reconstruction algorithms for optical diffraction tomography," *J. Opt. Soc. Am. A*, vol. 22, no. 11, pp. 2338–2347, 2005.

[18] C. G. Sontheimer, "Square-law detector." Patent, August 1945. 2387472.

[19] M. E. Gehm and D. J. Brady, "High-throughput hyperspectral microscopy," vol. 6090, p. 609007, SPIE, 2006.

[20] M. E. Gehm, R. John, D. J. Brady, R. M. Willett, and T. J. Schulz, "Single-shot compressive spectral imaging with a dual-disperser architecture," *Opt. Express*, vol. 15, no. 21, pp. 14013–14027, 2007.

[21] D. J. Brady, K. Choi, D. L. Marks, R. Horisaki, and S. Lim, "Compressive holography," *Opt. Express*, vol. 17, no. 15, pp. 13040–13049, 2009.

[22] D. Landgrebe, "The evolution of landsat data analysis," *Photogrammetric Engineering and Remote Sensing*, vol. LXIII, no. 7, pp. 859–867, 1997.

[23] F. Sigernes, D. A. Lorentzen, K. Heia, and T. Svenøe, "Multipurpose spectral imager," *Appl. Opt.*, vol. 39, no. 18, pp. 3143–3153, 2000.

[24] V. E. Brando and S. Phinn, "Guest editorial: Coastal aquatic remote sensing applications for environmental monitoring and management," *Journal of Applied Remote Sensing*, vol. 1, p. 011599, 2007.

[25] C. M. Stellman, G. G. Hazel, F. Bucholtz, J. V.Michaelowicz, A. Stocker, and W. Schaaf, "Real-time hyperspectral detection and cuing," *Optical Engineering*, vol. 39, no. 7, pp. 1928–1935.

[26] J. B. Campbell, *Introduction to remote sensing*. The Guilford Press, 3rd ed., 2002.

[27] M. E. Martin, M. B. Wabuyele, M. Panjehpour, M. N. Phan, B. F. Overholt, R. C. DeNovo, T. Moyers, S. G. Song, and T. Vo-Dinh, "Dual modality fluorescence and reflectance hyperspectral imaging: principle and applications," vol. 5692, pp. 133–139, SPIE, 2005.

[28] A. Siddiqi, H. Li, F. Faruque, W. Williams, K. Lai, and M. Hughson, "Use of hyperspectral imaging to distinguish normal, precancerous, and cancerous cells," *Cancer Cytopathology*, vol. 114, no. 1, pp. 13–21, 2008.

[29] M. B. Sinclair, J. A. Timlin, D. M. Haaland, and M. Werner-Washburne, "Design, construction, characterization, and application of a hyperspectral microarray scanner," *Appl. Opt.*, vol. 43, no. 10, pp. 2079–2088, 2004.

[30] J. Lerner and R. Zucker, "Calibration and validation of confocal spectral imaging systems," *Cytometry A*, vol. 62A, pp. 8–34, 2004.

[31] P. Kasil and T. Vo-Dinh, "Hyperspectral imaging system using acousto-optic tunable filter for flow cytometry applications," *Cytometry A*, vol. 69A, no. 8, pp. 835–841, 2006.

[32] Q. Li, Y. Xue, G. Xiao, and J. Zhang, "New microscopic pushbroom hyperspectral imaging system for application in diabetic retinopathy research," *Journal of Biomedical Optics*, vol. 12, no. 6, p. 064011, 2007.

[33] R. G. Sellar and G. D. Boreman, "Classification of imaging spectrometers for remote sensing applications," *Optical Engineering*, vol. 44, no. 1, p. 013602, 2005.

[34] ChromoDynamics, "HSi-300 hyperspectral imaging system data sheet," tech. rep., Orlando, FL. `http:/www.chromodynamics.net/`; accessed February 24, 2010.

[35] C. Research and Instrumentation, "Varispec liquid crystal tunable filters brochure," tech. rep., Cambridge, MA. `http://www.cri-inc.com/`; accessed February 24, 2010.

[36] A. A. Wagadarikar, N. P. Pitsianis, X. Sun, and D. J. Brady, "Video rate spectral imaging using a coded aperture snapshot spectral imager," *Opt. Express*, vol. 17, no. 8, pp. 6368–6388, 2009.

[37] C. A. Fernandez, A. Wagadarikar, D. J. Brady, S. C. McCain, and T. Oliver, "Fluorescence microscopy with a coded aperture snapshot spectral imager," vol. 7184, p. 71840Z, SPIE, 2009.

[38] C. F. Cull, K. Choi, D. J. Brady, and T. Oliver, "Identification of fluorescent beads using a coded aperture snapshot spectral imager," *Appl. Opt.*, vol. 49, no. 10, pp. B59–B70, 2010.

[39] L. Gao, R. T. Kester, and T. S. Tkaczyk, "Compact image slicing spectrometer (iss) for hyperspectral fluorescence microscopy," *Opt. Express*, vol. 17, no. 15, pp. 12293–12308, 2009.

[40] M. E. Gehm, M. S. Kim, C. Fernandez, and D. J. Brady, "High-throughput, multiplexed pushbroom hyperspectral microscopy," *Opt. Express*, vol. 16, no. 15, pp. 11032–11043, 2008.

[41] S. McCain, M. Gehm, Y. Wang, N. Pitsianis, and D. Brady, "Coded aperture raman spectroscopy for quantitative measurements of ethanol in a tissue phatom," *Applied Spectroscopy*, vol. 60, no. 6, pp. 663–671, 2006.

[42] E. C. Cull, M. E. Gehm, B. D. Guenther, and D. J. Brady, "Standoff raman spectroscopy system for remote chemical detection," vol. 5994, p. 59940H, SPIE, 2005.

[43] C. Fernandez, B. D. Guenther, M. E. Gehm, D. J. Brady, and M. E. Sullivan, "Longwave infrared (lwir) coded aperture dispersive spectrometer," *Opt. Express*, vol. 15, no. 9, pp. 5742–5753, 2007.

[44] D. J. Schroeder, *Astronomical Optics*. California: Academic Press, 2nd ed., 2000.

[45] J. A. Hackwell, D. W. Warren, R. P. Bongiovi, S. J. Hansel, T. L. Hayhurst, D. J. Mabry, M. G. Sivjee, and J. W. Skinner, "LWIR/MWIR imaging hyperspectral sensor for airborne and ground-based remote sensing," vol. 2819, pp. 102–107, SPIE, 1996.

[46] A. Goetz, G. Vane, J. Solomon, and B. Rock, "Imaging spectrometry for earth remote sensing," *Science*, vol. 228, no. 4704, pp. 1147–1153, 1985.

[47] C. M. Stellman, G. G. Hazel, F. Bucholtz, J. V. Michalowicz, A. Stocker, and W. Schaaf, "Real-time hyperspectral detection and cuing," *Optical Engineering*, vol. 39, no. 7, pp. 1928–1935, 2000.

[48] C. M. Stellman, F. M. Olchowski, and J. V. Michalowicz, "WAR HORSE (wide-area reconnaissance: hyperspectral overhead real-time surveillance experiment)," vol. 4379, pp. 339–346, SPIE, 2001.

[49] M. Maggioni, G. L. Davis, F. J. Warner, F. B. Geshwind, A. C. Coppi, R. A. DeVerse, and R. R. Coifman, "Hyperspectral microscopic analysis of normal, benign and carcinoma microarray tissue sections," vol. 6091, p. 60910I, SPIE, 2006.

[50] M. Huebschman, R. Schultz, and H. Garner, "Characteristics and capabilities of the hyperspectral imaging microscope," *Engineering in Medicine and Biology Magazine, IEEE*, 2002.

[51] W. Vermaas, J. Timlin, H. Jones, M. Sinclair, L. Nieman, S. Hama, D.K.Melgaard, and D. Haaland, "In vivo hyperspectral confocal fluorescence

imaging to determine pigment localization and distribution in cyanobacterial cells," *PNAS*, vol. 105, no. 10, pp. 4050–4055, 2008.

[52] M. Descour and E. Dereniak, "Computed-tomography imaging spectrometer: experimental calibration and reconstruction results," *Appl. Opt.*, vol. 34, no. 22, pp. 4817–4826, 1995.

[53] P. Mouroulis, R. O. Green, and T. G. Chrien, "Design of pushbroom imaging spectrometers for optimum recovery of spectroscopic and spatial information," *Appl. Opt.*, vol. 39, no. 13, pp. 2210–2220, 2000.

[54] L. QingLi, X. YongQi, X. GongHai, and Z. JingFa, "Study on microscope hyperspectral medical imaging method for biomedical quantitative analysis," *Springer Chinese Science Bulletin*, vol. 53, no. 9, pp. 1431–1434, 2008.

[55] S. C. Gebhart, R. C. Thompson, and A. Mahadevan-Jansen, "Liquid-crystal tunable filter spectral imaging for brain tumor demarcation," *Appl. Opt.*, vol. 46, no. 10, pp. 1896–1910, 2007.

[56] T. Vo-Dinh, B. Cullum, and P. Kasili, "Development of a multi-spectral imaging system for medical applications," *J. Phys. D.*, vol. 36, no. 14, pp. 1663–1668, 2003.

[57] A. R. Harvey, D. W. Fletcher-Holmes, A. Gorman, K. Altenbach, J. Arlt, and N. D. Read, "Spectral imaging in a snapshot," vol. 5694, pp. 110–119, SPIE, 2005.

[58] W. Johnson, D. Wilson, M. H. W. Fink, and G. Bearman, "Snapshot hyperspectral imaging in opthalmology," *J. Biomed. Optics*, vol. 12, no. 1, pp. 1–7, 2007.

[59] J. Bioucas-Dias and M. Figueiredo, "A New TwIST: Two-Step Iterative shrinkage/thresholding algorithms for image restoration," *Image Processing, IEEE Transactions on*, vol. 16, pp. 2992–3004, 2007.

[60] S. E. Reichenbach, S. K. Park, and R. Narayanswamy, "Characterizing digital image acquisition devices," *Optical Engineering*, vol. 30, no. 2, pp. 170–177, 1991.

[61] V. Nuzhin, S. Solk, and A. Nuzhin, "Measuring the modulation transfer functions of objectives by means of CCD array photodetectors," *J. Opt. Technol, OSA*, vol. 75, pp. 111–113, 2008.

[62] P. Costianes, "An overview of concealed weapons detection for homeland security," pp. 2–6, dec. 2005.

[63] R. McMillan, N. Currie, J. Ferris, D.D., and M. Wicks, "Concealed weapon detection using microwave and millimeter wave sensors," in *Microwave and Millimeter Wave Technology Proceedings, 1998. ICMMT '98. 1998 International Conference on*, pp. 1–4, 1998.

[64] D. McMakin, D. Sheen, and H. Collins, "Remote concealed weapons and explosive detection on people using millimeter-wave holography," pp. 19 –25, oct 1996.

[65] M. R. Fetterman, J. Grata, G. Jubic, J. W. L. Kiser, and A. Visnansky, "Simulation, acquisition and analysis of passivemillimeter-wave images in remote sensingapplications," *Opt. Express*, vol. 16, no. 25, pp. 20503–20515, 2008.

[66] S. Stanko, F. Kloppel, J. Huck, D. Notel, M. Hagelen, G. Briese, A. Gregor, S. Erukulla, H.-H. Fuchs, H. Essen, and A. Pagels, "Remote concealed weapon detection in millimeter-wave region: active and passive," vol. 6396, p. 639606, SPIE, 2006.

[67] N. R. C. committee on Assessment of Security Technologies for Transportation, *Assessment of Millimeter-Wave and Terahertz Technology for Detection and Identification of Concealed Explosives and Weapons*. Washington, D.C.: The National Academies Press, 2007.

[68] N. Farhat and W. Guard, "Millimeter wave holographic imaging of concealed weapons," *Proceedings of the IEEE*, 1971.

[69] D. Sheen, D. McMakin, and T. Hall, "Three-dimensional millimeter-wave imaging for concealed weapon detection," *Microwave Theory and Techniques, IEEE Transactions on*, vol. 49, pp. 1581 –1592, sep 2001.

[70] R. N. Anderton, R. Appleby, J. E. Beale, P. R. Coward, and S. Price, "Security scanning at 94 GHz," vol. 6211, p. 62110C, SPIE, 2006.

[71] R. Appleby, R. N. Anderton, N. H. Thomson, and J. W. Jack, "The design of a real-time 94-GHz passive millimetre-wave imager for helicopter operations," vol. 5619, pp. 38–46, SPIE, 2004.

[72] M. Kemp, "Millimetre wave and terahertz technology for detection of concealed threats - a review," in *Infrared and Millimeter Waves, 2007 and the 2007 15th International Conference on Terahertz Electronics. IRMMW-THz. Joint 32nd International Conference on*, pp. 647–648, Sept. 2007.

[73] E. Candes, J. Romberg, and T. Tao, "Stable signal recovery from incomplete and inaccurate measurements," *Communications on Pure and Applied Mathematics*, vol. 59, pp. 1207–1223, 2006.

[74] W. L. Chan, M. Moravec, R. Baraniuk, and D. Mittleman, "A single-pixel terahertz imaging system based on compressed sensing," *Appl. Phys. Lett.*, vol. 93, pp. 1211051–1211053, 2008.

[75] W. L. Chan, M. L. Moravec, R. G. Baraniuk, and D. M. Mittleman, "Terahertz imaging with compressed sensing and phase retrieval," *Opt. Lett.*, vol. 33, no. 9, pp. 974–976, 2008.

[76] S. J. LaRoque, E. Y. Sidky, and X. Pan, "Accurate image reconstruction from few-view and limited-angle data in diffraction tomography," *J. Opt. Soc. Am. A*, vol. 25, no. 7, pp. 1772–1782, 2008.

[77] L. Denis, D. Lorenz, E. Thiébaut, C. Fournier, and D. Trede, "Inline hologram reconstruction with sparsity constraints," *Opt. Lett.*, vol. 34, no. 22, pp. 3475–3477, 2009.

[78] E. N. Leith and J. Upatnieks, "Reconstructed wavefronts and communication theory," *J. Opt. Soc. Am.*, vol. 52, no. 10, pp. 1123–1128, 1962.

[79] T. M. Kreis and W. P. O. Jüptner, "Suppression of the dc term in digital holography," *Optical Engineering*, vol. 36, no. 8, pp. 2357–2360, 1997.

[80] H. Choo, J. Woo, D. Kim, S. Shin, and Y. Yu, "DC suppression in in-line digital holographic microscopes on the basis of an intensity-averaging method using variable pixel numbers," *Optics & Laser Technology*, vol. 41, pp. 741–745, 2009.

[81] J. Goodman, *Introduction to Fourier Optics*. New York: McGraw-Hill, 1968.

[82] T. Latychevskaia and H. Fink, "Solution to the Twin Image Problem in Holography," *Phys. Rev. Lett.*, vol. 98, no. 23, pp. 2339011–2339014, 2007.

[83] R. Mersereau and A. Oppenheim, "Digital reconstruction of multidimensional signals from their projections," *Proceedings of the IEEE*, vol. 62, no. 10, pp. 1319 – 1338, 1974.

[84] R. Mueller, M. Kaveh, and R. Inversion, "A new approach to acoustic tomography using diffraction techniques," *Acoust. Imaging*, vol. 8, pp. 615–628, 1980.

[85] J. Bioucas-Dias and M. Figueiredo, "A New TwIST: Two-Step Iterative Shrinkage/Thresholding Algorithms for Image Restoration," *Image Processing, IEEE Transactions on*, 2007.

[86] A. Kak and M. Slaney, *Principles of Computerized Tomographic Imaging*. IEEE Press, 1988.

[87] M. A. Richards, *Fundamentals of Radar Signal Processing*. New York: McGraw-Hill, 2005.

[88] Z. Wu, J. Kinast, M. E. Gehm, and H. Xin, "Rapid and inexpensive fabrication of terahertz electromagnetic bandgap structures," *Opt. Express*, vol. 16, no. 21, pp. 16442–16451, 2008.

[89] M. Harwit and N. Sloane, *Hadamard Transform Optics*. New York, USA: Academic Press, 1979. pp. 50-59.

[90] I. Stojanovic, W. C. Karl, and M. Cetin, "Compressed sensing of mono-static and multi-static SAR," vol. 7337, p. 733705, SPIE, 2009.

Biography

Christy Ann Fernandez was born in Hinesville, Georgia on November 26, 1982 to Edwin and Wanda Fernandez. She attended high school at the Lawrenceville School in Lawrenceville, New Jersey and at the Zaraphath Christian School in Zaraphath, New Jersey. She graduated from high school in 2001. While in high school, Christy took classes at Columbia University in New York City.

Christy began her undergraduate studies at American University in Washington, DC. She graduated early with honors in 2004 with a Bachelor of Science degree in Physics. During her undergraduate career, she volunteered on the Hill and partook in various internships. Christy was the recipient of American University's Jacob Kastner Memorial Fund Scholarship in Physics, an AFCEA Armed Forces scholarship for academic achievement, and a NIH/NHLBI BRTPUM fellowship. She was also a McNair Scholar during her undergraduate studies.

In Spring 2005, Christy began her graduate studies in the Electrical and Computer Engineering department at Duke University under the supervision of Dr. David Brady. She graduated with a Master of Science degree in May 2007 after defending her thesis entitled, "Longwave Infrared (LWIR) Coded Aperture Dispersive Spectrometer." During her graduate career, she was a recipient of a National Defense Science and Engineering Graduate (NDSEG) fellowship.

Christy will receive her Doctor of Philosophy degree in May 2010.

Publications

1. C.F. Cull, J.N. Mait, D. Wikner, M. Mattheiss, and D.J. Brady. "Millimeter-wave compressive holography," *Special Feature RF Imaging: Architectures and Applications* Appl. Opt., 49 (19), 2010.

2. C.F. Cull, K. Choi, D. Brady, and T. Oliver, "Identification of fluorescent beads

using a coded aperture snapshot spectral imager." Appl. Opt., 49 (10), 2010.

3. C. Fernandez-Cull, D. Brady, D. A. Wikner, and J. N. Mait, "Millimeter-Wave Imaging Using k-Space Compression," in *Computational Optical Sensing and Imaging*, OSA Technical Digest (CD) (Optical SOciety of America, 2009), paper CTuA3.

4. C.A. Fernandez, A. Wagadarikar, D. Brady, S.C. McCain, and T. Oliver, "Fluorescence microscopy with a coded aperture snapshot spectral imager," Three-Dimensional and Multidimensional Microscopy: Image Acquisition and Processing XVI, San Jose, CA, USA, SPIE.

5. M.E. Gehm, M.S. Kim, C. Fernandez, and D.J. Brady, "High-throughput, multiplexed pushbroom hyperspectral microscopy," Opt. Express 16, 11032-11043 (2008).

6. C. Fernandez, B.D. Guenther, M.E. Gehm, D.J. Brady, and M.E. Sullivan, "Longwave infrared (LWIR) coded aperture dispersive spectrometer," Opt. Express 15, 5742-5753 (2007).

7. C. Fernandez, S. Nayeri, and L. Medsker., "Independent component analysis applications in physics," Neural Networks, 2005. IJCNN '05. Proceedings. 2005 IEEE International Joint Conference on , vol.4, no., pp.2213-2216 vol. 4, July 31 2005-Aug. 4 2005

Conferences

1. (*Poster*) C. F. Cull, D. Brady, D. A. Wikner, and J. N. Mait, "Sparse Fourier Sampling in Millimeter-Wave Compressive Holography", Digital Holography and Three-Dimensional Imaging (DH) (April 2010)

2. C. F. Cull, D. A. Wikner, M. Mattheiss, J. N. Mait, D. J. Brady, "Sparse sampling and enhanced axial resolution in millimeter-wave holographic imaging," SPIE Defense and Sensing (April 2010)

3. C.F. Cull, D. Brady, D. A. Wikner, J. N. Mait, "Millimeter-Wave Imaging Using k-Space Compression," Computational Optical Sensing and Imaging (COSI) meeting, (2009)

4. C. Fernandez, A. Wagadarikar, S.C. McCain, and D. J. Brady, "Fluorescence microscopy with a coded aperture snapshot imager," SPIE Photonics West 2009 BiOS Biomedical Optics Symposium. Three-Dimensional Multidimensional Microscopy: Image Acquisition and Processing XVT. (Jan 2009)

5. (*Poster*) S.Lim , Bobby D. Guenther, David J. Brady, C. A. Fernandez, and S. T. McCain, "High-Throughput, Multiplex Aperture-Coded Raman Spectrometer for Biomedical Diagnostics," Biomedical Optics St. Petersburg, FL. (March 2008)

6. (*Invited talk D. Brady Presented*) D. Brady and C. Fernandez, "Multi-Spectral Microscopy using Coded Aperture Snapshot Spectral Imaging," International Topical Meeting on Information Photonics (2008)

7. C. Fernandez, B.D. Guenther, M.E. Gehm, D.J. Brady, and M.E. Sullivan, "Longwave Infrared (LWIR) Coded Aperture Dispersive Spectrometer," OSA Annual Meeting (2006)

8. C.A. Fernandez, E.C. Cull, S.T. McCain, M.E.Gehm, and D.J. Brady, "Liquid Light Guides for High Efficiency coupling to Diffuse Source Spectrometers" SPIE Photonics West (Jan 2006)